AFRL-AFOSR-VA-TR-2021-0023

Microwave Enhancement of Composite Solid Propellant Flames

Sippel, Travis
IOWA STATE UNIVERSITY
1350 BEARDSHEAR HALL
AMES, IA,
US

04/03/2021
Final Technical Report

DISTRIBUTION A: Distribution approved for public release.

Air Force Research Laboratory
Air Force Office of Scientific Research
Arlington, Virginia 22203
Air Force Materiel Command

REPORT DOCUMENTATION PAGE

Form Approved
OMB No. 0704-0188

1. REPORT DATE *(DD-MM-YYYY)* 03-04-2021	**2. REPORT TYPE** Final	**3. DATES COVERED** *(From - To)* 15 Feb 2017 - 14 Feb 2020

4. TITLE AND SUBTITLE Microwave Enhancement of Composite Solid Propellant Flames	**5a. CONTRACT NUMBER**
	5b. GRANT NUMBER FA9550-17-1-0167
	5c. PROGRAM ELEMENT NUMBER
6. AUTHOR(S) Travis Sippel	**5d. PROJECT NUMBER**
	5e. TASK NUMBER
	5f. WORK UNIT NUMBER
7. PERFORMING ORGANIZATION NAME(S) AND ADDRESS(ES) IOWA STATE UNIVERSITY 1350 BEARDSHEAR HALL AMES, IA US	**8. PERFORMING ORGANIZATION REPORT NUMBER**
9. SPONSORING/MONITORING AGENCY NAME(S) AND ADDRESS(ES) AF Office of Scientific Research 875 N. Randolph St. Room 3112 Arlington, VA 22203	**10. SPONSOR/MONITOR'S ACRONYM(S)** AFRL/AFOSR RTA1
	11. SPONSOR/MONITOR'S REPORT NUMBER(S) AFRL-AFOSR-VA-TR-2021-0023

12. DISTRIBUTION/AVAILABILITY STATEMENT
A Distribution Unlimited: PB Public Release

13. SUPPLEMENTARY NOTES

14. ABSTRACT

The aim of this project is to investigate strategies with which to efficiently deposit microwave energy to the flame structure of a propellant to enable dynamic control of propellant energy release rate and new functionalities. Specifically, techniques to interface microwave energy with either (1) the gas phase flame or (2) the propellant condensed phase are explored.

Microwave energy deposition to the gas phase was found to be possible by either (1) increasing the electron number density of the gas phase flame in order to establish within the flame a weak microwave induced plasma (WMIP) or (2) to deposit energy to high-temperature metal oxide combustion products, whose dielectric loss increases exponentially with temperature (e.g. aluminum oxide). With respect to WMIP, it was found that doping of an energetic material with reagents producing strongly electro-positive species (i.e. alkali metals in form of metal nitrates of sodium, potassium, or cesium) within the flame, were effective. Experiments conducted on composite solid propellant demonstrated throttling enhancement of burning rate by up to 60% at atmospheric pressure. Simulations of a 1-D planar flames show that electromagnetic shielding of the flame/s inner core can be significant and is exacerbated by high alkali concentrations (i.e. high electron number density). An optimum dopant level, relative to the size of the flame in order to achieve microwave field penetration of the flame core. A new two-photon laser induced fluorescence scheme with an order of magnitude improvement in signal to noise ratio was also demonstrated and used to explore the WMIP initiation process in propellants.

15. SUBJECT TERMS

16. SECURITY CLASSIFICATION OF:			**17. LIMITATION OF ABSTRACT**	**18. NUMBER OF PAGES**	**19a. NAME OF RESPONSIBLE PERSON**
a. REPORT	**b. ABSTRACT**	**c. THIS PAGE**			MITAT BIRKAN
U	U	U	UU	83	**19b. TELEPHONE NUMBER** *(Include area code)* 426-7234

Standard Form 298 (Rev.8/98)
Prescribed by ANSI Std. Z39.18

Microwave Enhancement of Composite Solid Propellant Flames

Final Technical Report for work Executed under AFOSR Grant FA9550-17-1-0167
Performance period: Feb. 15 Feb 2017 – 14 Feb 2020

Submitted by

Prof. Travis Sippel, PI
515-294-3803 (phone)
515-294-3261 (fax)
tsippel@iastate.edu

Prof. James Michael, co-PI
515-294-0723 (phone)
515-294-3261 (fax)
jmichael@iastate.edu

Dr. Stuart Barkley
Dr. Keke Zhu
Joel Lynch

Iowa State University
Department of Mechanical Engineering
2090 Black Engineering Bldg
Ames, IA 50011

TABLE OF CONTENTS

1. Executive Summary

The aim of this project is to investigate strategies with which to efficiently deposit microwave energy to the flame structure of a propellant to enable dynamic control of propellant energy release rate and new functionalities. Specifically, techniques to interface microwave energy with either (1) the gas phase flame or (2) the propellant condensed phase are explored.

Microwave energy deposition to the gas phase was found to be possible by either (1) increasing the electron number density of the gas phase flame in order to establish within the flame a weak microwave induced plasma (WMIP) or (2) to deposit energy to high-temperature metal oxide combustion products, whose dielectric loss increases exponentially with temperature (e.g. aluminum oxide). With respect to WMIP, it was found that doping of an energetic material with reagents producing strongly electro-positive species (i.e. alkali metals in form of metal nitrates of sodium, potassium, or cesium) within the flame, were effective. Experiments conducted on composite solid propellant demonstrated throttling enhancement of burning rate by up to 60% at atmospheric pressure. Simulations of a 1-D planar flames show that electromagnetic shielding of the flame/s inner core can be significant and is exacerbated by high alkali concentrations (i.e. high electron number density). An optimum dopant level, relative to the size of the flame in order to achieve microwave field penetration of the flame core. A new two-photon laser induced fluorescence scheme with an order of magnitude improvement in signal to noise ratio was also demonstrated and used to explore the WMIP initiation process in propellants.

Techniques involving microwave interaction with condensed phase reactants have demonstrated the ability to highly localize microwave energy absorption and to accelerate burning rates by multiple orders of magnitude. The development of nanoscale thermites with thermally switchable microwave absorptivity is demonstrated through wrapping of thermite clusters with graphene oxide (GO). It was found that thermites wrapped in GO are highly microwave reflective and are not microwave-ignitable under high-power microwave irradiation for long durations (up to 60 seconds). Heating of these thermites was found to lead to GO reduction and as a result, drastic changes in the thermites' microwave absorptivity, which enabled microwave-ignition of the thermites in as short as 200 to 300 ms. The development of such materials, with thermally switchable microwave absorption properties may prevent parasitic microwave energy loss within the bulk condensed phase of an energetic material and enable highly localized microwave loss to the energetic material burning surface. Application of microwave fields to wired propellants (i.e. propellants with spatially graded electrical conductivity) has been demonstrated as a technique with which to achieve multiple orders of magnitude dynamic control over propellant burning rate. A burning rate enhancement of 700% has been demonstrated in use of graphite wires in AP composite propellant where the radius of the wire is matched to the microwave skin thickness.

Taken together, these techniques demonstrate the high degree of utility that can be enabled in design of energetic materials with electromagnetic function. However, this research program also demonstrates that the development of efficient, electromagnetically active energetic materials will require a number of considerations new to the field of energetics. Electromagnetically 'smart' energetic materials have several applications, including development of throttled solid rocket motors, enhanced propellant ignition and flame spread, and dynamically controlled light emission pyrotechnics, among others.

2. Background and Project Motivation

2.1. Motivation

Solid propellants are used in a variety of propulsion applications where high thrust-to-weight ratios and resilient, stable systems are required. Due to their high mass fraction, motors derived from solid propellants find applications in launch vehicles and munitions but are used despite a lack of on-command thrust control or throttling. Unlike liquid rocket engines or hybrid rockets engines, which can dynamically control thrust by altering the liquid fuel or oxidizer flow rate, solid rocket motors typically use a pre-defined grain geometry that cannot be altered after production. Moreover, the burning rate of a solid motor, while predictable, often produces an unsteady or noisy thrust output, which can introduce unwanted vibration or structural loading [1]. Finally, ignition and extinction of solid rocket motors are difficult to achieve in practice, and direct throttling of the thrust in most solid motors is severely limited by high pressures and high temperatures in the combustion chamber.

In order to address these limitations, several techniques to control or extinguish thrust have been explored. These include global pressure control (e.g. pintle nozzles or rapid depressurization quench) [2], lab-scale demonstrations of infrared laser irradiation of the burning surface [3], local pressure and velocity perturbations in the combustor through tailored combustor geometry [4], and the use of hydroxylammonium nitrate (HAN)-based formulations having voltage-sensitive burning rates [5]. Some possible limitations of these techniques include lower propellant mass fractions (pintle nozzles), lower specific impulse/flame temperature formulations (HAN and pintle), highly specific formulations (HAN), and difficulty in scaling to motor configurations (laser irradiation). Although previous application of these techniques provided a means of controlling or throttling motor thrust, more robust and capable techniques are desired.

Microwave coupling to energetic materials, as their flames are highly metal-liaden and they frequently contain a high quantity of alkali metal, provides an intriguing environment for (1) study of microwave interactions with alkali metals (e.g. sodium) and metalloids (e.g. aluminum) within flames and (2) for control of light emission, with applications including enhanced brightness battlefield illuminants, dynamically controlled strobe formulations, and ‘smart’ flares with dynamically controlled color or color ratio. Conventional strategies require tailoring the composition to include various colorant additives (e.g., nitrate salts of barium, sodium, or strontium), selection of formulations with unsteady combustion, or other methods to achieve the desired wavelength, color purity, and intensity [6]. This approach can be laborious and offers no real time control. Moreover, light-emission design through formulation can result in hazards, as many colorants and additives commonly used today (e.g., perchlorates, heavy-metals, strontium additives, and barium additives) produce toxic or environmentally hazardous products [7]. New strategies are needed for producing high color purity and high radiance emitters, while also reducing fabrication complexity and the use of hazardous or regulated emitter ingredients.

2.2. Gas-Phase Microwave Plasma Enhancement

Plasma-based combustion enhancement of energetic materials has been previously demonstrated using electrothermal-chemical (ETC) launchers, which result in improved ignition flame spread, pressurization rate, and global propellant burning rate of solid gun propellants [8,9]. ETC plasmas are generated by the electrical explosion of a conductive filament, subsequent ablation of a filament liner, and electrical discharge through the resulting plasma. The electron temperature of the resulting plasma has been estimated to be ~1.4 eV [10]. Burning rate enhancement can occur from advective effects, chemical kinetic effects, and non-advective heat transfer enhancement [8]. Non-advective heat transfer effects, in particular, have been the topic of much study, and it has been proposed [11] that for spectrally transparent propellants, increased enhancement results from radiation absorption within the propellant matrix, leading to decomposition of the propellant condensed phase ahead of the burning front. This hypothesis is supported by experimental observation of varying degrees of burning rate enhancement in propellants of differing opacity [12], and observation of evidence of particle reaction ahead of the steady state condensed phase preheat region within quenched, optically transmissive articles [13]. Burning rate enhancement during post plasma quenching times has also been found to be formulation dependent [14]. Additionally, the effects of formation of a plasma sheath at the burning surface have also been shown to be important [15].

With such techniques, recent studies have shown burning rate enhancements of up to 35% are possible [16]. Further enhancement has been demonstrated in compositions with higher solid loading fractions [11]. However, burning rate enhancement techniques used in ETC launchers are limited to single plasma injections using a capillary plasma (a single shot technique) in a limited volume (10's of centimeters in length) [17]. While well-suited to gun propellant applications, this technique is inappropriate for rocket motors, which require a scalable and sustained plasma discharge.

These techniques draw heavily from historical efforts to enhance and control hydrocarbon flames using sub-breakdown electric fields, a well-reviewed topic within plasma-assisted combustion research [18,19]. In particular, high-frequency electric fields (e.g., MHz and above at atmospheric pressures), have been used to improve igniters and enhance flame speed [18]. In these gas-phase systems, field energy is primarily deposited to free electrons, the only charged species able to gain and transfer momentum in phase with the alternating electric field. The intricate balance of electron heating and relaxation by atomic and molecular collisions is characterized by the Boltzmann equation, ultimately enabling non-equilibrium populations of excited state neutrals [20–22]. Herein, we refer to this approach as weak microwave induced plasma (WMIP), which is similar to conventional MIP but generated by relatively weak (sub-breakdown) electric fields. For alkali-energetic materials, early research confirmed that visible and near-infrared (VIS/NIR) emission is dominated by spontaneous emission from electronically excited alkali atoms [23–27], making the WMIP approach relevant for these systems. While direct electron collisions are thought to be the primary pathway for producing excess alkali emitters, indirect production by collisions with other excited molecules, like electronically-excited metastable nitrogen, may play a role [28].

Beyond gas-phase flames, energetic materials and their multiphase products have demonstrated a variety of pathways for electric-field enhancement. Application of microwave fields to aluminized solid propellants containing low ionization energy dopants (e.g., $NaNO_3$ 16 wt.%) have been shown to increase the atmospheric pressure burning rate by up to 60%. The ability of the WMIP hypothesis to be applied to these materials was bolstered by direct measurements of non-equilibrium sodium temperatures [29]. Still, the burning rate enhancement of a propellant can also result from microwave energy transfer through other mechanisms, including (1) dielectric thermal runaway of metallic oxide combustion products [30], and (2) dielectric heating of the condensed-phase propellant reactants. Microwave energy transfer to condensed phase reactants of energetic materials containing electrically conductive phases (e.g. metal fuels) is expected to be higher due to eddy current heating [31], which, for metal spheres, is a function of the particle size and microwave penetration depth [32]. In order to improve microwave absorption of most non-metallized energetic materials [33–35], additives with high dielectric loss have been included [36,37].

2.3. Alkali Enhancement of Gas Phase Flame Electron Population

Coupling of microwave energy to the background electron population of a gas phase flame is possible using the high strength electric fields of pulsed microwave sources. The resulting plasmas have been shown to improve combustion limits, open additional kinetic pathways, and provide increased fuel flexibility of gas phase flames [38]. Sub-critical, non-breakdown operation of pulsed fields enables selective microwave coupling to high ionization and low density regions of the flame and has been shown to increase local flame temperature, flame speeds, and improve flammability limits of premixed gaseous flames [39].

The field strength required to achieve efficient energy coupling to the flame can be reduced by increasing the background level of ionization within the flame. In such a manner, efficient coupling can be achieved by microwave radiation from sources generating lower field strengths such as a conventional continuous wave (CW) magnetron. In order to achieve efficient energy coupling to a weakly-ionized flame environment, there is a requirement that the applied field frequency be less than the electron-neutral collision frequency (ion-neutral and ion-electron collisions can be assumed to be negligible due to the slow rate). For the applicable propellant flame number densities at atmospheric pressure, the electron-neutral collisions are expected to be on the order of 10^{11} per second [40]. This was confirmed by BOLSIG+ simulations showing an average of 4.5×10^{11} collisions per second over the relevant range of reduced field strengths. Comparing this to the microwave field frequency ($\sim1.8\times10^{10}$ radians/sec), application of radio frequency and microwave fields can result in efficient electron-neutral collisional energy transfer, as scattering processes sufficiently randomize electron trajectories before field reversals counteract the added momentum [41]. In targeting efficient coupling, one approach is to increase the free electron population and thereby promote increased electron production rates with applied fields. This can be achieved through the addition of low-ionization threshold materials which exhibit significant thermal ionization at propellant flame temperatures. This increase in electron concentration has been previously demonstrated in a fuel lean hydrogen-oxygen flame doped with an alkali metal [42].

In this work, we demonstrate the use of alkali metal doping for efficient, moderate field-strength microwave energy deposition to the flame, which results in significant combustion enhancement. We identify mechanisms responsible for burning rate enhancement, including plasma enhancement, microwave energy absorption by condensed phase aluminum oxide features, and direct microwave energy absorption by the propellant condensed phase. Specifically, this effort aims to (1) explore the effects of dopant addition on equilibrium flame electron populations and propellant performance, (2) experimentally explore the effects of alkali doping and microwave plasma seeding on microwave absorption, flame structure, and burning rate enhancement, and

(3) explore the mechanisms through which microwave energy couples with and is deposited to a composite solid propellant flame structure.

2.4. Microwave Enhancement of Energetic Material Light Emission

While both the gaseous and condensed phases provide pathways for energy deposition via high-frequency fields, there are significant obstacles to realizing enhancement with microwaves. Chiefly, the microwave frequency range (~1-10 GHz) resides below typical plasma frequencies for adiabatic combustion of alkali energetic materials (~0.1-1 THz), which limits microwave penetration to the outer regions of energetic material plumes where air entrainment reduces the temperature, alkali density, and electron density. Additionally, to sustain a non-equilibrium population of emitters, the electron-alkali excitation rate must exceed the efficient alkali-molecular quenching processes [43]. Finally, while the high concentrations of alkali species may be expected to yield substantial increases in the alkali atomic emission, this may be offset by self-absorption of emitted radiation which has been well documented in sodium lamps and alkali-energetic materials [23–27,44]. Self-absorption is mitigated by resonant atomic broadening, which shifts emission wavelengths to regions far from line center with less absorption [44]. Thus, the degree of light emission enhancement that can be expected from application of an electromagnetic field to an alkali energetic material flame remains an open question.

Modeling of emission in alkali-magnesium energetic materials has been performed, but only under the strict conditions of Boltzmann (electronic), Saha (ionic), and Planck (optical) equilibrium [23–26]. Still, relaxing these assumptions has become common-place in plasma modeling [45], and provides a framework for inclusion in energetic material emission models. First, Boltzmann non-equilibrium, both in the electron and excited-state alkali species, must be accounted for. Rate coefficient data for alkali excitation and quenching in molecular gases is well known [43], and the rates of electron-alkali excitation and super-elastic collisions can be computed using a Boltzmann solver with the appropriate electron-alkali cross-section data [46]. Second, deviations from Saha equilibrium sufficient to cause electrical breakdown are possible but are not typically desired for free-space combustion enhancement. Finally, Planck non-equilibrium, the imbalance of absorption and emission, while inevitable, requires solution of the radiation-transfer equation.

2.5. Alkali Metal Detection and Thermometry Techniques

Optical measurement techniques based on alkali seeding have been investigated in a variety of combustion and flow environments. Sodium D-line reversal methods and sodium/potassium laser-induced fluorescence (LIF) intensity ratios have been applied to measure high temperature and shock-heated environments [47]. Single-photon laser-induced fluorescence of sodium was used to determine quantitative sodium distributions during coal combustion [48]. In addition, sodium fluorescence of the D-line transition has been used to measure velocity in gaseous jets by relying on the Doppler shift of sodium atoms [49], and with an inverse flow-tagging by the depletion of ground state sodium by laser-induced ionization [50]. Although these techniques have been successfully employed, they often require corrections in high optical density environments due to the resonant excitation and collection of the fluorescence signal.

For single-photon D-line excitation, both the laser excitation and emission take place at identical wavelengths and interference is difficult to avoid. Sources of interference include signal trapping, strong attenuation of the incoming laser beam, and re-fluorescence [51]. Signal trapping refers to the absorption of emitted photons before reaching the detector and leads to a decrease in signal yield. Overcoming laser absorption also becomes challenging in high optical density regions and requires significant corrections. In addition, for resonant excitation and detection schemes, re-fluorescence can lead to an effective elongation of the observed fluorescence lifetime and spatial broadening of the features of interest. A final complication, which is exacerbated in multiphase flows, is the inability to discriminate using optical filters because the fluorescence signal and scattering signal are at the same wavelength. These features of single-photon resonant excitation and detection of atomic species limit the applicability of single-photon LIF approaches in high-concentration gas phase systems, and are particularly challenging in multiphase combustion systems where particle and droplet scattering are prevalent.

To mitigate these issues, multiphoton techniques have been studied extensively for combustion environments using N atom [52], H atom [53], and O atom [54,55] where two-photon absorption allows interrogation with readily-accessible wavelengths. Other multiphoton approaches have been used for detection of and other small molecules using resonance-enhanced multi-photon ionization (REMPI) [56] and microwave scattering from REMPI [57]. More recently, picosecond and femtosecond laser excitation has shown promise for reducing interference from photo-dissociation of other molecules, and allows for much lower laser fluence due to the high peak power of the pulse [58,59]. Recently, two-photon excited fluorescence has been used in optically dense atomizing sprays for improved imaging contrast [60]. These multi-photon techniques allow access to additional transitions as the quantum mechanical selection rules allow changes of angular momentum $= 0$ and $=\pm 2$, instead of the normal single-photon selection rule ($=\pm 1$). In addition, for atoms including sodium, this typically results in spontaneous emission from the excited state to additional intermediate electronic states, allowing for wavelength discrimination between the excitation and emission wavelengths. Sodium two-photon laser-induced fluorescence has been explored by Weiland et al. [51] and Allen et al. [61] for flames seeded with alkali salts. Weiland et al. [51] investigated two different two-photon excitation schemes (3s–4d and 3s–5s) and reported the ionization loss, amplified spontaneous emission (ASE), and quenching to other states. They did not, however, investigate excitation to the 3d state with a two-photon process. This process is potentially advantageous as a spontaneous transition from 3d–3p is expected, in comparison to the 3s–4d excitation which has been reported with a relatively low quantum yield [51].

2.6. Microwave Interactions With the Energetic Material Condensed Phase To Induce Ignition

Microwave heating of most non-metalized energetic materials (e.g. ammonium nitrate, ammonium perchlorate, tetryl, PETN, RDX, HMX, TNT, and others) is inefficient, and microwave ignition of these energetics occurs on timescales of tens of seconds to minutes [35]. The slow dielectric heating rate of many energetics is due to the non-polar molecular structure (low dielectric loss) and/or low electrical conductivity of many energetic molecules [34,35,62]. In order to accelerate electromagnetic heating, several studies have proposed the inclusion of microwave absorptive susceptor materials, such as silicon carbide (SiC), graphite, or carbon nanotubes (CNT) [62,63]. The addition of micron-sized graphite flakes to nanoscale aluminum (n-Al)/nanoscale iron (II) oxide (n-Fe_2O_3) thermites to enhance microwave heating (3.3 GHz, 170 W) was investigated by Crane et al. [37]. The authors found that 10 wt.% addition of graphite flakes increased microwave heating of the thermite by approximately 100 K min^{-1}. However, heating rates were found to be less pronounced at higher graphite concentrations because of increased bulk electrical conductivity, which decreased the depth of microwave penetration in the energetic (skin depth).

Interaction of electric fields with bulk electrical conductors are typically ignored due to a conductor's small skin depth. However, granular metal particle packs, which are typically found in energetic materials, are well known to exhibit significant microwave energy absorption when the particles are smaller than the wavelength of the field, resulting in conduction losses at particle surfaces due to eddy currents or magnetic induction heating [31]. A modelling study by Biswas et al. recently showed microwave heating of metal particles coated with an oxide shell results in electric field dominated heating in the low conductivity oxide shell, while magnetic field dominated heating occurs in the metal core [64]. In an experimental and modeling study [65], micron-sized Al/Fe_3O_4 thermites were ignited using low continuous power microwave fields (2.1 GHz, 100 W), using an antenna electrode to produce electric field strengths of ~2000 kV m^{-1} at the electrode tip, which produced experimental ignition delays of approximately three seconds. Consequently, the authors proposed that microwave absorption was mostly induced by the electric field component, causing formation of a localized hot spots within the oxide shell due to a thermal runaway instability. Furthermore, a recent experimental study on microwave ignition of n-Ti/ polyvinylidene fluoride energetic suggested that ignition is mainly due to electric field absorption of the oxide shell [66].

2.7. Dielectric Properties of Granular Composites And Energetic Materials

The complex permittivity of a material is given in real and imaginary components, where the real permittivity (ε') indicates the energy storage potential of the material and the imaginary component (ε'') indicates the dielectric loss of the medium. For a homogenous material, the dielectric properties are dependent on the material phase and lattices structure [67]. When an electromagnetic field is applied to a homogenous medium, atoms, molecules, free charge and defects rearrange position during temperature- and frequency-dependent material relaxation. Such properties are important to understanding (1) the thermal response of the condensed phase of an energetic during RF/microwave radiation exposure and (2) the effects of presence of a condensed phase (e.g. attenuation and impedance mismatch) on the field distribution within the non-condensed phase. In a propellant combustion application, while gas-phase absorption effects will occur, as a first step, one may first consider a non-participating gas medium. In doing so, to understand the effects of presence of a perfectly dielectric absorbing propellant condensed phase medium on field distribution and thermal response, the Helmholtz and heat equations (1), (2) are considered, where E is the electric field, ω is angular frequency, ρ is density, c is speed of sound, k is the thermal conductivity, T is temperature, and q_v'' is volumetric heat generation. Furthermore, the volumetric heat generation due to permittivity loss within the RF/microwave field can be written as in equation (3). Condensed phase heating is important from a practical standpoint in order to develop microwave enhancement combustion models and to develop microwave power application regimes.

$$- \nabla^{2} \quad = \omega^{2}\varepsilon_{0}(\varepsilon^{'} - \qquad (1)$$

$$— = \quad ^{2} + \quad '' \qquad (2)$$

$$'' = \qquad ^{2}/2) \qquad (3)$$

Regarding microwave absorption in the condensed phase, previous studies on S-band and X-band microwave absorption of metal filled polymer composites have measured the dielectric properties of micron size metal filled particulate composites, and show that the microwave loss tangent (tan(δ)) within metal particulates is strongly sensitive to particle size and composition [68]. Particle type and size has been shown to be important in determining metal particle energy absorption [69]. Metal particles are known to couple well with S- and X-band microwave radiation and can heat through eddy current mechanisms, with smaller metal particle sizes interacting more effectively with microwaves. While the interaction of high explosives (HMX, RDX, TNT) materials with microwaves has been investigated by measuring the dielectric properties via cavity perturbation of various formulations [33], only very limited literature exist on the dielectric properties of different composite propellants ingredients (e.g. AP, HTPB) [35]. Further, no measured bulk properties of composite propellant formulations or models thereof currently exist in open literature. In order to advance microwave-seeded plasma throttling enhancement of composite solid propellant combustion, it is necessary to measure and be able to predict the microwave properties of the composite solid propellant condensed phase. An investigation is needed to explore condensed phase propellant properties in order to enable RF-thermal modeling and designing of resonant propellant strand cavities and motor configurations that efficiently utilize microwave energy to throttle combustion.

2.8. Microwave Interactions With Graphene Oxide and Reduced Graphene Oxide Composites

Efficient electromagnetic heating of interfaces can be accomplished with the use of nanoscale materials. Graphene, in particular, is unique for its high electrical and thermal conductivity and high charge mobility, all of which result from its unique sp^2, tightly packed carbon lattice structure [70]. Consequently, graphene is a good absorber of alternating electric fields, particularly at microwave frequencies, due to Maxwell-Wagner polarization effects [71]. However, when graphene is oxidized, forming graphene oxide (GO), additional oxygen-containing groups present on the graphene lattice inhibit charge localization and electron mobility, resulting in low microwave absorptivity and high reflectivity [72]. The ability to reduce GO to r-GO through chemical and thermal methods [70] presents an opportunity to dynamically control the microwave absorption of materials. As reduction progresses, charge concentration and electron mobility are improved, thus resulting in higher absorption [73]. Moreover, reduction of GO to r-GO results in lattice defects, which upon electric field application, result in defect polarization/relaxation and group electronic dipole relaxation losses. As a consequence, defects should also result in better microwave absorption, field penetration, and impedance matching characteristics of r-GO as compared to defect-free graphene [72–74].

Reduced graphene oxide coatings have been employed in a number of studies to improve absorption within composites containing nanoscale metallic oxides [75–78]. In all of these previous works, the authors demonstrated increased loss tangent or reduced reflection with addition of 10 to 30 wt.% of r-GO. In particular, the addition of r-GO to nanoscale Fe_3O_4-based composites has been shown to reduce microwave reflection loss from -6 dB to -38 dB [75]. Hollow spheres of Fe_3O_4 wrapped within r-GO sheets have shown enhanced complex permittivity and stronger absorption properties in the frequency ranges of 2 to 18 GHz [78]. The enhanced microwave energy absorption properties of r-GO can be used to produce nanoparticles through microwave shock heating (1600 ºC heating in 100 ms) on an r-GO substrate [79]. In material fabrication, many of these studies have utilized the intra-surface forces of graphene nanomaterials in suspension to form coatings around particles. Specifically, graphene materials can be crumpled / wrapped due to surface tension effects when in suspension within an evaporating liquid droplet [80]. These properties of r-GO/GO may be exploited in synthesis and may enable the ability to alter the microwave ignition properties of nanoscale energetic materials.

2.9. Burning Rate Enhancement of Wired Solid Propellants

To address problems of slow propellant burning rates (low thrust), several techniques to enhance propellant burning rate solid rocket motor combustion and thrust have been explored. By adding conductive wires into propellants, burning rate can be further enhanced. Metal wires cast into propellant produce a more favorable thermal conduction pathway for transport of heat generated by the propellant flame to the condensed phase propellant [81–83]. Inert metal wire materials that have been tested in propellants include graphite, copper, silver, steel, tungsten, molybdenum, brass, and platinum [84–86]. Adding conductive inert wires into propellants can decrease the overall propellant performance [87] if volume and mass fractions are high [88] and do not add further energy to the propellant. Conductive structures can produce large metal agglomerates that have slow energy release and can have deleterious two-phase flow and stability effects. To address this problem, reactive metal foils have been studied, the combustion of which leads to more rapid flame spread and decreased slag formation as compared to inert metal wires [89].

The degree of temperature rise achievable within an embedded wire depends on the thermal diffusivity and melting point of the wire as well as other properties. With traditional inert wire enhancement, all heat supplied to the wire is transported from the combustion wave at the burning surface. As such, selective control of heat distribution within the wire and dynamic control of burning surface are not possible. However, by adding energy to a wire by non-combustion methods, it may be possible to further enhance burning rate. Specifically, wires can be resistively joule heated through DC voltage bias application. At non-static frequencies, current flow within the wire becomes localized to the wire skin, where electric field is non-trivial, and heating occurs by eddy current flow. Unlike traditional inert wire enhancement, the AC field induced current density within wires is improved as wire diameter is reduced and wire perimeter/cross-section ratio is increased, suggesting that AC field enhancement techniques may reduce the volume fraction of a motor comprised of inert wires and may also reduce wire agglomerate effects. Heating is readily achieved through eddy current flow within the exterior skin of a number of conductive materials within high frequency oscillatory electric fields at microwave frequencies.

3. Research Aims

The overall aim of this effort is to develop strategies to dynamically control the energy output of an energetic material through interface of a solid propellant and its flame with microwave energy and is graphically described in Fig. 1. Specifically, the effort is divided into two thrusts (1) investigation of strategies to microwave-control propellant combustion through use of energetic material dopants to couple microwave energy to the propellant gas phase flame, resulting in weak microwave-induced plasma (WMIP) effects, including burning rate control and flame optical emission modulation (color shifting and brightness modulation); and (2) the development of condensed phase nanoscale ingredients and geometric control of propellant condensed phase conductivity in order to localize microwave energy absorption spatially within the energetic material condensed phase in order to rapidly effect changes in energetic material energy release rate.

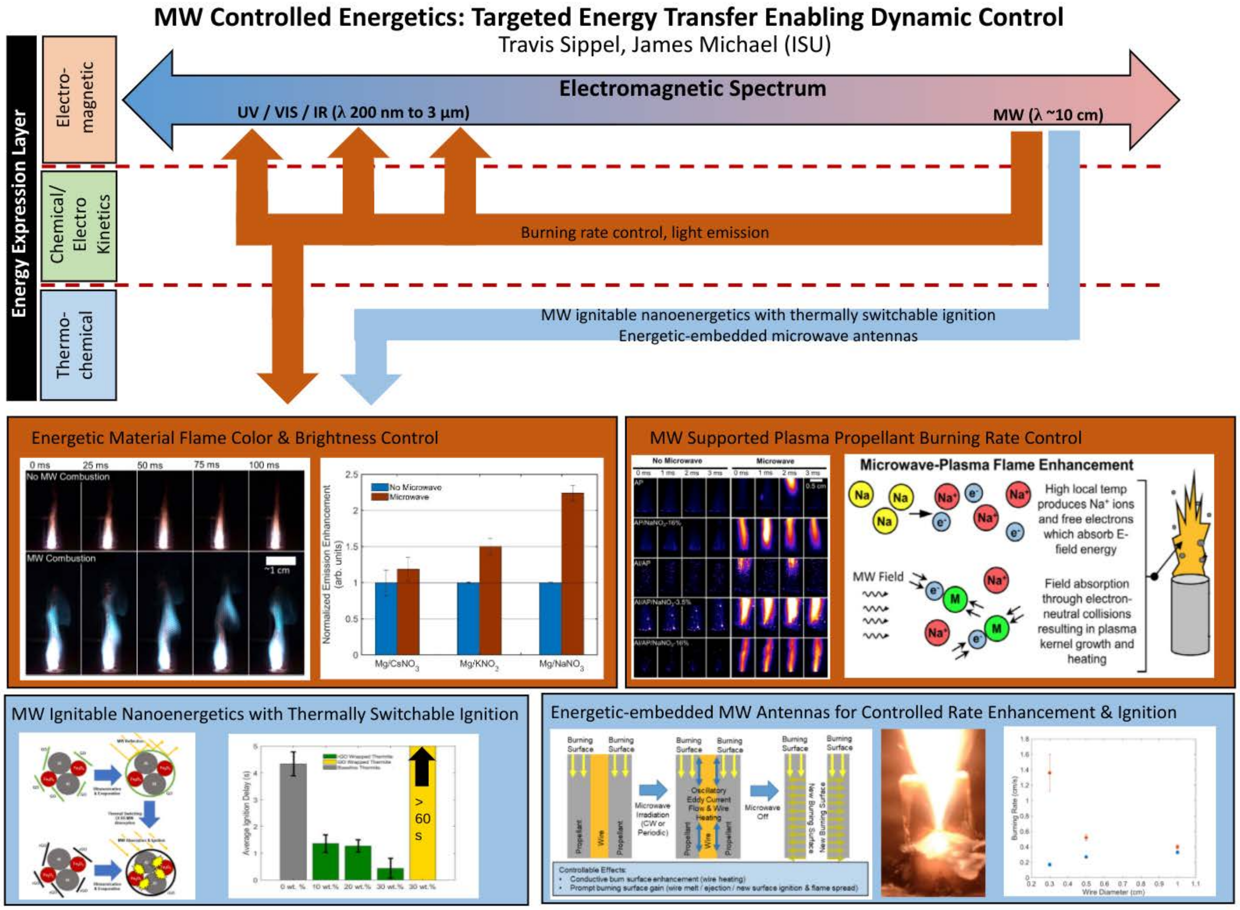

Figure 1. Conceptual description of the effort. The effort ais to fundamentally explore methods to interact, using microwave energy, with the combustion of a solid propellant--either in the gas phase of a propellant flame or to focus and localize microwave energy absorption to the energetic material condensed phase in order to achieve rapid change in and control of energy release rate.

With respect to methods of interface with the propellant gas phase, the effort specifically explores the potential to interface microwave energy with the gas phase flame through either (1) inclusion of additives that will increase the electron population of the gas phase flame, allowing microwave deposition of energy to the gas phase, or (2) addition of metals to the energetic material that through oxidation, will produce metal oxides that have high dielectric absorptivities at high temperature, allowing microwave absorption of energy to high temperature flame regions. These studies, respectively, focus on the use of sodium nitrate, NaNO3, as a material to increase the quantity of free electrons within the flame or the use of metals (i.e. aluminum, magnesium) in order to produce high temperature, microwave-absorptive metal oxides within the gas phase flame and product plume.

With respect to methods of interface of microwave energy with the condensed phase of an energetic material, exploiting the unique electrical properties of graphene oxide (GO) and reduced graphene oxide (rGO) is considered as a means to achieve dynamic control of microwave absorption. Specifically, nanoscale thermites of a model Al/Fe2O3 formulation are fabricated and wrapped with GO coatings. It is demonstrated that wrapping of the thermites with GO is highly efficient at preventing microwave ignition of the thermites under illumination of a high power microwave field. It is further shown that the microwave absorptivity of such thermites can be thermally switched by heating them, leading to rapid ignition of the thermites under illumination by a microwave field. Such thermites, as additives within a solid propellant, may enable localization of microwave energy to the high-temperature burning surface of a propellant. The rapid modification of the temperature profile at the burning surface of a propellant has been shown to enable both burning rate acceleration and propellant extinguishment.

4. Experimental and Computational Methods

4.1. Simulation and Numerical Methods

4.1.1. Equilibrium Chemical Calculations

Chemical equilibrium calculations were conducted on composite solid propellant and energetic material formulations to identify stoichiometries producing favorable translational temperatures, ion and electron populations, and condensed-phase flame products. The NASA Chemical Equilibrium with Applications (CEA) code [90] was used to make thermochemical predictions for (1) 68 MPa chamber pressure conditions and ideal expansion to 1 atm (propellants) and (2) atmospheric pressure combustion (10 wt.% excess air) energetic material combustion. In energetic material calculations, the assumed heat of formation of the epoxy binder (Epon/Versamid; $H_{98}C_{83}O_{14}N_4$) was -3,666 kJ-mol^{-1}. All calculations were conducted with ion chemistry enabled.

4.1.2. Microwave-Enhanced (VIS/NIR) Emission Model

Comprehensive modeling of microwave-enhanced energetic materials is a formidable challenge. A high-fidelity approach would require coupling radiation-transfer, electric field propagation, chemically reacting fluid dynamics, and non-equilibrium electron kinetics, covering a vast range of timescales over multiple dimensions. As a first step, we introduce a collisional-radiative model with the minimum components needed to capture the proposed WMIP effect for atomic alkali emission in quasi-steady state over plasma and optical timescales ($\approx 0.5 - 50$. This requires solving a radiation transfer equation where both the emission rate and probability of radiation escape vary as a function of distance into a model plume. The emission coefficient varies according to a kinetic rate balance regulated by the local electric field strength, which in turn is determined from the penetration characteristics of an applied microwave field. The result is a spectrally-integrated solution for radiance emitted perpendicular to the plume surface. Ratios of radiance with and without applied fields are then directly compared to ratios of irradiance in experiments computed in Eqn. 1.

Four key assumptions were necessary to simplify the dimensions and number of required parameters; the rationale for these assumptions are discussed in Appendix A. They are: (1) Except for alkali species, the plume is treated as a homogenous and quiescent post-combustion zone with a prescribed temperature and alkali mole fraction deviating from CEA equilibrium, with a hard interface to the ambient environment; (2) the microwave field does not significantly perturb the plume from Saha equilibrium or increase the plume temperature; (3) Planck equilibrium is maintained within the plume such that only a minor fraction of radiation escapes and is ultimately detected; and (4) the rates of alkali absorption and emission are negligible compared to kinetic pathways. As heat and mass transfer from entrained air are expected, the plume temperature $_0$ and alkali mole fraction are left as parameters to represent the conditions for the outer layer of the plume, averaged over time and plume surface.

For a single atomic alkali transition or doublet, the resulting radiance is a convolution integral of the rate of radiant energy emission and the frequency-integrated probability of photon escape from the plume. Integrating from the plume center line (s=L) to the edge (s=0), this takes the base form,

$$= \int_{0} \epsilon(\quad (\tag{4}$$

where: is the normalized plume depth described graphically in Fig. 2, is the radiance ($^{-2}\ ^{-1}$) at the surface of the plume; $\epsilon(\ )$ is the volumetric emission coefficient $\left(\ ^{-3}\ ^{-1}\right)$ at a given depth; is the width of the plume slab; and $(\ )$ is the transmittance, or normalized probability of photon escape to $= 0$. A sample configuration is shown in Fig. 2, where the field strength, transmittance, and emission coefficient all decline until a critical depth $= \delta$, or skin depth, where the field effect becomes negligible.

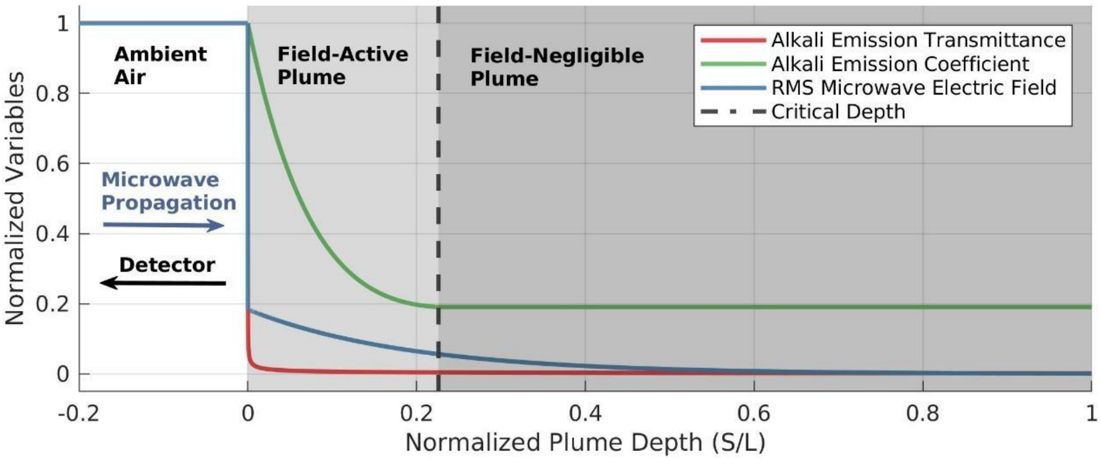

Figure 2. Example configuration of the homogenous plume model with an incident electric field propagating left to right, perpendicular to the plume surface. Radiance is computed at surface, $= 0$*, simulating light available for detection.*

The derivation of transmittance is described in Appendix B, which relies on the presence of resonant line broadening reviewed by de Groot and Vliet [44], and the frequency-averaged escape factors reviewed by Drawin and Emard [91]. The result depends only on the depth, , and the wavelength λ.

$$(\ ) = {}^{-\frac{1}{2}}\sqrt{\frac{\lambda}{4\pi^2}}, \qquad > \frac{\lambda}{4\pi} \tag{5}$$

For Eqn. 4, the integration of $< \lambda/4\pi$ can be neglected, as . The emission coefficient is obtained by

$$\epsilon(\ ) = {}_{21}\frac{h\nu}{4\pi}{}_{2} = \frac{1}{\lambda^3}\left(\frac{1}{{}_{2}}\frac{{}^{2}}{\epsilon_0}{}_{12}\right)\frac{h}{4\pi}{}_{2} \tag{6}$$

where $_{21}$ is the coefficient for spontaneous emission, $_{1}$ $_{2}$ is the ratio of ground to excited state degeneracies, ν is the photon frequency, $_{12}$ is the oscillator potential, and $_{2}$ is the non-equilibrium excited-state alkali population. The emission coefficient for sodium and potassium doublets were computed as single transitions. For cesium, only the higher-energy transition, Cs 6P(3/2), was measured and simulated. The local $_{2}$ population is obtained using assumption (4), which neglects emission and absorption in the steady-state rate balance

$${}_{2}(\ ) = {}_{1}\frac{(}{(} \tag{7}$$

where $_1$ is the ground state alkali density, and are the respective rate coefficients for alkali-neutral excitation and quenching, $_+$ and $_-$ are the same but for alkali-electron rates, is the mole fraction of molecular background gas, and is the mole fraction of free electrons. $_1$ is defined through the parameter for alkali mole fraction . The electron mole fraction, , is obtained through Saha equilibrium, and is set by CEA equilibrium calculations. Out of necessity, the quenching rate of all molecular species is assumed to match that of molecular nitrogen, which is already a sizeable fraction of the mixture. Because all the alkali-molecule interactions are treated as alkali-nitrogen, the effect of air entrainment on Eqn. 7 is contained implicitly in the free parameter and its relationship with .

At flame and energetic material temperatures, the quenching rate approaches the thermal limit

$$= \sigma \sqrt{\frac{{}_0}{\pi\mu}} \tag{8}$$

where σ is a cross section specific to each alkali, and μ is the effective reduced mass of the alkali species with N_2 [43]. The complementary excitation rate is then constrained by the requirement of detailed balance. Using Maxwell-Boltzmann statistics, an Arrhenius expression for can be obtained

$$= \left[\sigma \sqrt{\frac{{}_2}{\pi\mu \; {}_1}}\right] {}^{\frac{1}{2}}_{0} \left(- \frac{1}{\lambda \; {}_0}\right) . \tag{9}$$

The electron-alkali rate coefficients $_+$ and $_-$ are determined from the BOLSIG+ code, which uses a two-term approximation to the Boltzmann equation to solve for the non-equilibrium electron energy distribution with an applied field effects [46]. Cross-sections for equilibrium products are obtained from the LXCat database for N_2 [92], CO [93], and Mg [92], which are used to approximate non-alkali combustion products. Alkali cross sections for elastic, excitation, and ionization are obtained for sodium, potassium, and cesium [94–96]. The resulting rates are computed as functions of the reduced root-mean square (RMS) electric field ($_0$, units of Td) and fitted to quadratic and logarithmic functions of electric field magnitude ( ) once total number density inside the plume $_0$ is known.

$${}_+ = {}_1 (\;)^2 + {}_2 (\;) + {}_3, \qquad {}_- = {}_1 + {}_2 \ln (\;(\;)) \tag{10}$$

The microwave field solution ( ) is computed using Fresnel equations for an electric field in air incident on an absorbing medium:

$$( ) = \ (0)\left[\frac{2}{1+\left|\tilde{\mu}_0\right|}\right] \ \left(- \ _0\right) \tag{11}$$

where (0) is the incident RMS electric field magnitude, determined from the parameter for applied reduced field) in the cavity outside the plume. The magnitude of the complex index of refraction $\left|\tilde{\mu}_0\right|$ and attenuation coefficient α_0 are calculated for plume conditions using the equations for collisional plasmas listed by Laroussi [97], where electron collision frequency is estimated from BOLSIG+ results.

A complication of using the BOLSIG+ solver is that $_+$ curve fits are typically invalid below 10 to 20 Td. This occurs when the field strength becomes negligible and thermal electrons become the dominant source of excitation. The reduced field where this transition occurs (defined as $\left(\ _0\right)^*$), can be obtained by inspection of Eqn. 10. The skin depth $= \delta$ of this transition to a zero-field regime is found by manipulation of Eqn. 11.

$$\delta = -\frac{1}{\alpha_0} \ \left[\frac{\left(\ _0\right)^*}{\left(\ \right)}\left(\frac{}{_0}\right)\left(\frac{1+\left|\tilde{\mu}_0\right|}{2}\right)\right] \tag{12}$$

Where the minimum skin depth for is $\delta = \lambda/4\pi \approx 0$. Then Eqn. 4 for total radiance can be solved piecemeal with Eqn. 5-12 by isolating the zero-field emission term $\epsilon(\delta)$:

$$= \int_{\lambda/4\pi}^{\delta} \epsilon(\ \ (\ \ + \epsilon(\delta)\int_{\delta} (\ \ . \tag{13}$$

Finally, the ratio of radiance with and without microwave application can be obtained as

$$= \frac{\int_{\lambda/4\pi}^{\delta} \epsilon(\ \ (\ \ (\delta) \int_{\delta} (}{\epsilon(0)\int_{\lambda/4\pi} (}, \tag{14}$$

where the primary unknown parameters are , $_0$, and .

4.2. Materials Manufacture

4.2.1. Mg-based Energetic Material Manufacture

The energetic material formulations used in this study consisted of magnesium (Firefox; 190-325 mesh), one of three different alkali nitrate oxidizers, and the aforementioned epoxy binder. All compositions were formulated for stoichiometric combustion in order to achieve maximum equilibrium flame temperatures. Alkali nitrate oxidizers used in formulations consisted of one of the following: sodium nitrate (Hummel Croton Inc., MIL-S-322C, Grade B, Mg/$NaNO_3$/epoxy: 45.6/49.4/5 wt.%); potassium nitrate (Hummel Croton Inc., MIL-P-156B, Mg/KNO_3/epoxy: 42.8/52.2.4/5 wt.%); or cesium nitrate (American Elements Engineering, Mg/$CsNO_3$/epoxy: 28.5/66.5/5 wt.%). The epoxy binder used was a two-part thermoset-epoxy consisting of 70 wt. % Epon-813 and 30 wt.% Versamid-140. All energetic material compositions were hand-mixed in a grounded pan using a metal spatula in quantities of 10 g or less. First, the fuel and binder were hand-mixed until homogeneous. Oxidizer was then blended into the fuel/binder pre-mixture. The composition was again hand-mixed until homogeneous. To achieve the desired consolidation density, reactive compositions were shim-pressed in a 6 mm diameter circular die to a nominal length of 9 mm using a Carver 12-ton press and a dwell time of approximately 10 seconds. Prior to combustion, pellets were inhibited with an acrylic lacquer to prevent flame spread down the sides of the pellet.

4.2.2. rGO and GO Wrapped Thermite Synthesis

Ten variations of r-GO/GO thermite composites were studied. The effects of r-GO loading on the thermite composite was first investigated using four different loadings of 0, 10, 20, and 30 wt.% of r-GO. The effects of selectively encapsulating either fuel or oxidizer with r-GO (30 wt.%) was also studied. Lastly, the effects of thermal reduction of GO (30 wt.%) to r-GO thermite composite was studied, where thermal reduction occurred at different time intervals (0, 5, 10, 15 minutes).

Reagents were from the following sources: GO and r-GO (Goographene), n-Al (Novacentrix, 80 nm), n-Fe_2O_3 (Mach I, 3 nm), ethylene glycol (Fisher Scientific), and acetone (Fisher Scientific). To create the baseline thermite (0.5 g, 0 wt.% GO/r-GO), n-Al (0.15 g) and n-Fe_2O_3 (0.35 g) were sonicated (Branson Digital Sonifier S-450) in acetone (20 mL) for 1.5 minutes. The composite was transferred to an electrostatic dissipative puck and dried at roughing vacuum.

To prepare the GO wrapped thermite composite, GO (0.15 g for 30 wt.%) was sonicated in ethylene glycol (EG, 20 mL) for 3.5 minutes with a small quantity of surfactant. The dried baseline nano-thermite (0.105 g of n-Al and 0.245 g of n-Fe_2O_3) was sonicated into the EG mixture for 3.5 minutes. The mixture was then washed with acetone, centrifuged, and dried at roughing vacuum for a minimum of 4 hours. The same procedure was used to prepare the r-GO thermite composite, with varying amounts of r-GO (10, 20, or 30 wt.%) and thermite mass ratio held constant (3 to 7, n-Al to n-Fe_2O_3). To create the thermite formulations that selectively encapsulated only either fuel or oxidizer in r-GO, either n-Al or n-Fe_2O_3 was first sonicated, washed, and dried using the aforementioned procedure. After the selectively encapsulated fuel or oxidizer was produced, the mixture was sonicated with either n-Fe_2O_3 or n-Al, respectively, in an acetone solution and dried at roughing vacuum.

To study thermal tuning of microwave absorptivity, GO thermites (30 wt.%) were thermally reduced. The GO/thermite composite (0.3 g) was placed in an aluminum tray was heated under argon in a tube furnace (Across International, STF1200). The furnace temperature was ramped at 75 °C min^{-1} to 400 °C, at which time the temperature was held constant for (1) 5 minutes, (2) 10 minutes, or (3) 15 minutes. The chosen reduction temperature of 400 °C is close to the 350 °C optimal reduction temperature of GO [98]. Composites were cooled under argon to room temperature prior to removal from the furnace.

4.2.3. Wire Propellant Manufacture

Prior to wired propellant fabrication, a survey of different potential wire materials was conducted. Parameters of particular interest include the wire diameter and skin penetration depth, δs, which together determine the wire cross-section in which eddy currents flow, the wire resistivity, wire melting temperature, and wire cross-section thermal mass—the product of wire density, specific heat, and square of wire diameter. Wire materials considered include aluminum, copper, graphite, silicon, and silicon carbide. Wires of copper and graphite were selected for this study based on commercial availability in diameters relevant to the study. Properties of copper and graphite wires used in this study are shown in Table 1. Wires were placed onto borosilicate glass windows (~22 by 22 by 0.1 mm) and a thin layer of composite solid propellant was cast onto the glass surface, encapsulating the wire as shown in Figure 3a. The propellant formulation consisted of 76 wt. % bimodal distribution of ammonium perchlorate (4:1 coarse to fine ratio, 200 µm and < 90 µm, Firefox Chemicals) and 20 wt. % of hydroxyl-terminated polybutadiene (HTPB) binder system. The binder system consisted of R45 monomer (Firefox Chemicals), isodecyl pelargonate (IDP, Firefox Chemicals) plasticizer, HX-878 bonding agent (tepanol, Firefox Chemicals), and IPDI isocyante curative (Firefox Chemicals). The propellant formulations were mixed for three hours in a dual planetary mixer and deaerated at room temperature and under roughing vacuum for 30 minutes. Following casting, propellant was cure for seven days at 60 °C in an explosion proof oven. Before casting, a borosilicate glass view window and wire were placed in the mold. After curing, propellant strands were taken out of the molds. Measured densities of cured propellants were greater than 95% of theoretical maximum density (TMD). For combustion experiments, the surfaces of propellant strands were inhibited to prevent flame spread down the sides of the burning strands. Images of the wire propellant strands can be seen in Fig. 3b-e.

Table 1. Listing of wire materials used, dimensions, and properties: wire diameter, Dwire; wire length, ρMW; melting temperature, Tmelt; skin depth at 2.45 GHz, δs; and wire thermal mass per unit length, ρCDwire2 for a 1 mm diameter wire.

Wire Material	**Wire Diameter (mm)**	**Resistivity $\rho_{mw@\ 2.45\ GHz}$ ($\Omega x10^{-8}m$)**	**T_{melt} (K)**	**Skin Depth $\delta_{s\ @\ 2.45\ GHz}$ (µm)**	**ρCD_{wire}^{2} (J/m/K) (D_{wire}=0.5 mm)**
Copper	0.5	1.69	1358	1.3	3.44
Graphite	1.0; 0.5;0.3	1375	4300*	37.7	1.57

*Temperature indicates volatilization temperature of carbon

4.2.4. 3D Printed UV-Cured Propellant Manufacture with Functionalize Energetic Wires

To demonstrate the ability to microwave heat embedded wires, and to demonstrate use of 3D printing, which could be used to shape conductive structures into antennas with selectable bandwidth and directionality within propellant, UV curable AP composite propellants containing thermally cured, graphite nanoparticle doped propellant wire structures using a Hyrel Engine SR

3D printer. The binder system used in photocurable propellants was a urethane acrylate epoxy (Illumabond urethane acrylate 6115). The AP/binder matrix surrounding the energetic wire antenna comprised of 75 wt.% of fine AP and 25 wt. % of UV-curing epoxy. In order to print energetics wires with higher amounts of graphite nanoparticles, a thermally cured binder system was utilized because of the inability to cure with the UV curing epoxy due to the high optical density. The energetic wire propellant was comprised of 40 wt.% fine AP, 20 wt.% graphite nanoparticles

Photo curable propellants were mixed using the aforementioned procedure and placed into two different extrusion heads (KRA-5 and EMO-15). Both extruders were equipped with 1 mm, 17-gauge nozzles. The energetic wire of 1 mm diameter was printed first and was then surrounded by the photo-curable AP composite propellant, generating the same geometry of the solid wire propellants combustion articles. The photo-curable propellant was cured during the printing process using a bank of 370 nm LEDs applied for 30 seconds during the infill process after printing of every other layer. the propellant was bonded to borosilicate windows using the UV-epoxy and were placed in cure for seven days at 60 °C in an explosion proof oven to ensure the energetics wires were cured. An image of the printed propellants can be seen in Figure 3g.

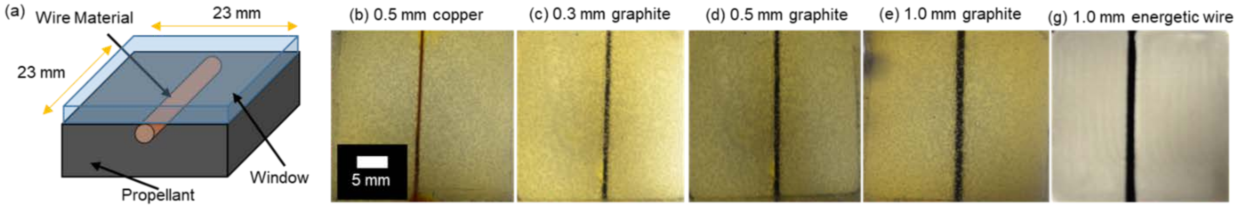

Figure 3. (a) Model of propellant strand with wire used during test. Backlight images of propellants with (b) 0.5 mm copper wire, (c) 0.3 mm graphite wire, (d) 0.5 mm graphite wire, (e) 1.0 mm graphite wire, and (f) 1.0 mm energetic wire comprised of graphite nanoparticle doped propellant within a 3D printed, photocured propellant matrix.

4.2.5. Propellant Fabrication for Dielectric Property Measurement

Each propellant formulation was modified by using different sizes of ammonium perchlorate (AP, 200 µm, < 90 µm Firefox Chemicals), sodium nitrate ($NaNO_3$, Firefox Chemicals) and aluminum (Al, 30 µm, Valimet) particles. Ammonium perchlorate and Al were used as-received (manufacturer specified sizes), while sodium nitrate was milled and sieved into size distributions (<75 µm) prior to use.

The propellants in this study were produced in batches of 800 g and formulations for propellants are shown in Table 1. Propellants utilized a HTPB binder system consisting of R45 monomer (Firefox Chemical), isodecyl pelargonate (IDP, Firefox Chemical) plasticizer, desmodour curative, and HX-878 (tepanol) bonding agent (RCS Rocket Motor Parts). Prior to mixing, ingredients were dried in an oven at 60 °C. Propellants were mixed for three hours in a six-quart dual planetary mixer. Propellant was deaerated at room temperature for 30 minutes at vacuum pressure and was cast using 3D printed rectangular casting molds and molds were placed in an explosion proof oven at 60 °C (140 °F) for a week to cure. The dimension of cured S-band propellant blocks was 7.264 x 3.450 cm (2.860 x 1.360 in) with length of 2.912 cm (1.1465 in). After curing, the propellant was finished to appropriate dimensions to be installed inside a WR-284 waveguide for dielectric measurement.

Table 1. Propellant formulations used in this study to investigate effects of NaNO3, AP, and Al particle size.

	Propellant Composition (wt. %)				
Formulation	**$NaNO_3$ (< 5 µm)**	**cAP (200 µm)**	**fAP (< 90 µm)**	**Al (30 µm)**	**HTPB**
f$NaNO_3$, bimodal AP	3.5	49.2	12.3	17	14
cAP, fine $NaNO_3$	3.5	61.5	---	17	14

4.3. Microwave Combustion Cavities

4.3.1. Microwave Cavity Simulation

A tuned, impedance-matched microwave applicator for use in atmospheric pressure propellant strand combustion experimentation was designed in COMSOL 5.1 Multiphysics. The cavity was designed to operate at TE_{10n} mode with a short and one lambda waveguide wavelengths WR-284 waveguide. Within the cavity, a 7 mm diameter propellant strand having as-measured homogeneous dielectric properties serves as the test article. The strand is positioned concentrically within a 32 mm ID by 36 mm OD quartz tube. The cavity was optimized to have minimum loss throughout and the strand was placed in the E-field antinode for maximum heating.

4.3.2. Resonant Microwave Combustion Cavity

Microwave-enhanced propellant combustion experiments were conducted in a single-mode, impedance-matched, resonant microwave cavity fitted with a flow through microwave applicator (Fig. 4a). Cavity energy is supplied by a circulator-protected 870 W, 2.46 GHz CW magnetron (National 2M107-825) launched into a WR284 waveguide cavity and propagated in a TE_{10} resonant mode. The cavity is impedance matched to the load using a three-stub tuner, and calibrated, rectifying Schottky diodes (Pasternack PE8003) are used to monitor forward and reflected microwave power via a high-speed oscilloscope (Tektronix MSO 70404C). The microwave applicator is a choke-modified rectangular waveguide section containing two optical access ports in the E-plane and gas inflow/outflow choke ports in the H-plane (Gerling Applied Engineering). To prevent exposure of microwave components to corrosive propellant combustion exhaust, the applicator is modified by insertion of 19.81 mm thick press-fit polytetrafluoroethylene (PTFE) blocks on both sides of the applicator. The propellant and flame structure are positioned within the microwave applicator atop a PTFE stand and to improve flame observation, smoke is evacuated from the cavity by an air co-flow produced by light vacuum application to the top applicator choke. The cavity is terminated by a sliding short circuit, which is adjusted to generate a standing wave electric field antinode at the propellant/flame location, as shown in Fig. 4b. To compensate for presence of the PTFE blocks within the cavity, COMSOL Multiphysics 5.0 was used to simulate the unloaded cavity and select the length of the sliding short circuit. To match cavity impedance to that of the propellant load, a half-length propellant strand (~1 cm) was placed in the cavity and the stub tuner was adjusted to minimize reflection. The quality factor (Q-factor) of the unloaded microwave resonant cavity was measured utilizing a vector network analyzer (VNA, Anritsu MS46322A Shockline) and was determined to be ~80.

Electric field strengths within the waveguide test section were estimated with analytical solutions of Maxwell's equations and a numerical solution of the exact cavity geometry. For the waveguide resonant cavity consisting of WR284 waveguide, the analytical solution of Maxwell's equations for a transverse electric field mode (TE_{101}) can be used to calculate field strength [99]. The root-mean-square (RMS) E-field strength is estimated as 91 kV/m at cavity test conditions within an adiabatic temperature, 3.5 wt. % $NaNO_3$-doped, aluminized propellant flame (1 kW magnetron output power, Q-factor of 80, 1 atm pressure, T_{ad}=3032 K). This E-field is cast as a reduced electric field by normalizing by the neutral gas number density, as estimated from the adiabatic flame temperature and pressure, giving an upper bound for E/N of 38 Td (10^{-21} V m^2). This upper limit estimate of field strength is based upon measurements of an empty cavity. The cavity with a propellant strand partially inserted gives a similar Q factor. A lower bound (e.g. worst case) estimate of the E-field strength of the experiment can be made from consideration of the case where no energy is stored in the cavity. A numerical simulation (COMSOL Multiphysics) was conducted on the modified geometry in the microwave waveguide pass-through test section with an input port (TE_{10} mode, 1 kW of power) (Fig. 4c). PTFE blocks and gas inflow/outflow choke ports were included in this simulation in order to match the experimental setup. The RMS electric field strength in the cavity test location is estimated as ~38 kV/m (~16 Td at previously noted experimental conditions). Therefore, we estimate the RMS E-field strength of the microwave resonant cavity experiment is between 38-91 kV/m (~16-38 Td for the atmospheric pressure propellant flame environment). This bounded estimate is relevant to times during plasma kernel formation and early growth only, as the formation of a large plasma is expected to act as an energy sink and would effectively spoil the quality of the cavity resonator.

For combustion experiments, ~2 cm long propellant strands were positioned such that the burning surface was located at the top of the applicator and over the duration of an experiment (typically ~10 s duration), the burning surface would traverse the entire E-field plane. Formulations of these propellants were chosen based upon free electron flame populations predicted from CEA equilibrium calculation results. Propellant strands were ignited by a one second duration, ~30 W CO_2 laser illumination. Immediately following CO_2 laser illumination, the microwave field was modulated on and data acquisition was started. Light diagnostics included direct emission observation via high speed video (Phantom ir300 with 50 mm Nikon lens at 1 kHz acquisition rate) and high magnification backlit observation (Photron Fastcam SA-X2 with Infinity K2 microscope lens at 12.5 kHz acquisition rate and 0.293 µs exposure). Measurements of microwave-enhanced and unenhanced propellant burning rate were made from analysis of high speed video. High magnification backlit imaging was used to observe microwave field effects on the combustion of burning aluminum agglomerates within the propellant flame structure. Spectroscopic measurements (VIS-IR, Ocean Optics USB4000 at 5 Hz) were made of flame emission to estimate sodium temperature by a two-line emission technique. The two emission bands for Na I at 589 and 818 nm were collected simultaneously and filtered with two long-pass Schott glass filters (Thorlabs, FGL590 and FGL610). Light emission was imaged onto a 200 µm multimode fiber with a 50 mm diameter achromatic lens and coupled to the spectrometer. During combustion experiments, forward and reflected diode power measurements were used to monitor time-dependent microwave absorption of the propellant flame. As burning surface regression of a propellant strand causes insertion length of the propellant within the microwave applicator to change over the duration of a combustion experiment, the microwave absorption of the condensed phase (no flame) was measured as a function of propellant insertion length. These measurements were then compared with online absorption measurements taken from burning propellants to estimate the respective microwave absorption of the condensed phase and the flame structure over the duration of combustion experiments.

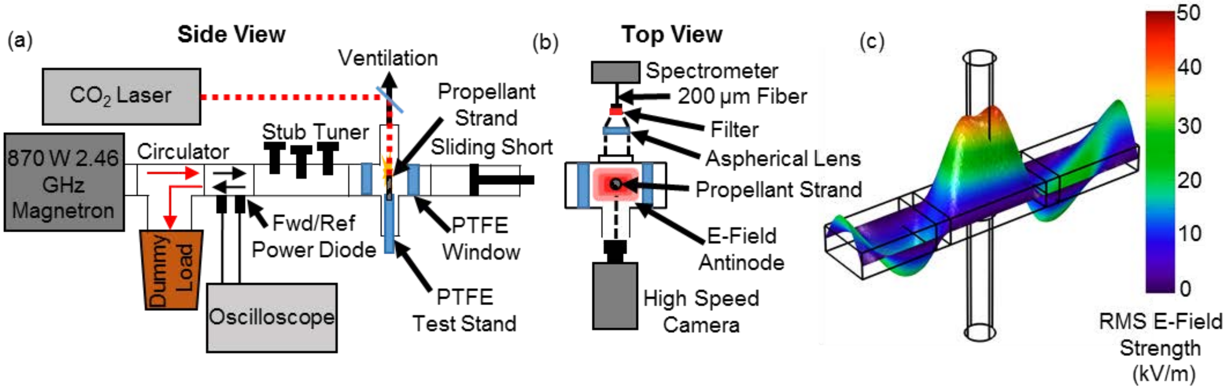

Fig. 4. (a) Schematic of experimental setup of the microwave resonant cavity, which includes a circulator-protected magnetron launch, forward and reflected directional coupler with diodes, a three-stub tuner to match propellant load impedance, a flow-through propellant combustion microwave applicator, and a sliding short circuit. (b) The top view of the combustion applicator shows optical access on both sides, where a high-speed camera and spectrometer collected data on burning rate and combustion flame emission. (c) COMSOL 5.0 simulation of microwave applicator test section E-field distribution with no energy stored in the system (lower bound E-field strength). The RMS E-field strength within the propellant flame volume is ~38-91 kV/m.

4.3.3. Multimodal Microwave Combustion Cavity

A multimode microwave cavity (Fig. 5a) connected to an 870 W, ~2.46 GHz magnetron and a high-voltage power supply modulated at 60 Hz (50 % duty cycle) was used for experiments. The energetic material was placed in an electric-field (E-field) antinode atop a microwave-transparent polytetrafluoroethylene (PTFE) block. The location of the field antinode was verified both experimentally and by numerical simulation. Experimentally, the E-field antinode location was found by imaging a liquid crystal film placed at various locations within the unloaded cavity during microwave application. The E-field distribution within the cavity was also determined by modeling the cavity using COMSOL Multiphysics 5.1 (Fig. 5b). The E-field strength in the volume occupied by the energetic material flame was estimated via dielectric heating of a 100 cm^3 volume of water according to the National Bureau of Standards procedure [100], yielding an average electric field strength of 2.1 ± 0.1 kV/m within the antinode of interest. Samples were microwave-ignited using an electromagnetically absorbing thin film (polyester/vapor deposited aluminum film), which was placed on the top of energetic materials and heated until ignition. For baseline experiments (without microwave), the energetic material composition was ignited directly using a hot wire ignition source.

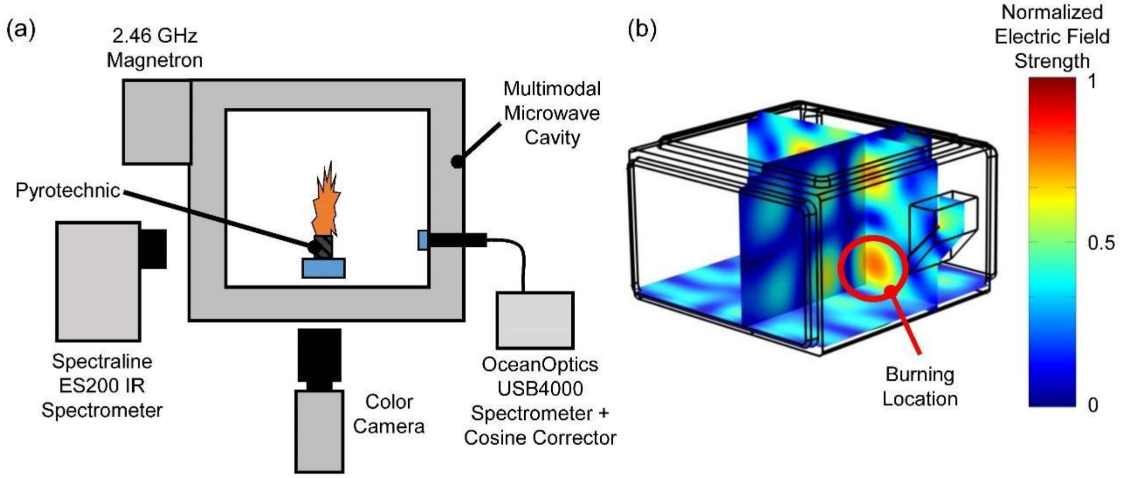

Figure 5. (a) Schematic of the experimental setup of the microwave cavity. Experiments were monitored with a color high-speed camera and two spectrometers (VIS/NIR and IR). (b) Distribution of the mean electric field strength simulated using COMSOL within the microwave chamber. The red circle indicates the location of the energetic material flame, which is located at an E-field antinode with an average field strength of 2.1 ± 0.1 kV/m in a 100 cm3 volume of water.

4.3.4. Alkali-seeded Combustion Burners

A premixed flat flame and an aluminized solid propellant flame, shown in Figure 6(a)-(b), were used to characterize the fluorescence behavior. The premixed flat flame burner, shown in Figure 6(a) was modified from the design of Hartung et al. [101]. All burner parts were fabricated from brass and the burner was cooled with a copper cooling tube brazed to the outer surface of the burner. The flame was established on the top plate of the burner, which consisted of 0.8-mm diameter holes resulting in a total open area of 35 percent. The plenum of the burner was filled with 2-mm glass beads. The premixed flame was established over the central portion of the burner using flow rates of 1 standard liter per minute (SLPM) of natural gas and 3 SLPM of air for an equivalence ratio of $\phi = 0.8$. The sodium-seeded flame in the burner is shown in Figure 6(a). Sodium was seeded into the gas-phase flames using an aerosol droplet seeder (TSI Aerosol Generator 3760) with sodium chloride dissolved in water at concentrations of ~360 g/L, respectively. Gas flow rates were metered with Alicat mass flow controllers with an accuracy of 1% and calibrated with a dry volume flow meter (MesaLabs Defender 530+). The gas flow rate of the aerosol seeder was measured by a Cole-Parmer flow meter. The sodium concentrations in the gas-phase flame is shown in Table 2 based on the measured flow rates for adiabatic chemical equilibrium using NASA Chemical Equilibrium with Applications (CEA) [90].

The aluminized solid composite propellant was manufactured using the same procedure as described by Barkley et al. [29] and consisted of 14.5 wt.% aluminium (35 , H-30, Valimet Inc.), 70.4 wt.% ammonium perchlorate (4:1 wt. 200 to <90 ratio, Firefox Enterprises LLC), 11.6 wt.% hydroxyl terminated polybutadiene binder system (HTPB), and 3.5 wt.% (>75 , Firefox Enterprises LLC). The was dried at 100 and roughing vacuum and then ball-milled and sieved to <75 prior to mixing and casting. The propellant formulations were mixed for three hours in a dual planetary mixer and deaerated at room temperature and under roughing vacuum for 30 minutes. Strands were cast into 6-mm diameter cylinders using polyethylene molds and allowed to cure for seven days at 60 in an explosion proof oven. After curing, propellant strands were cut to 20-mm lengths. The equilibrium sodium concentration from CEA at atmospheric pressure is shown in Table 2 for the sodium-doped propellant flame, and the adiabatic flame temperature is 3032 K .

Table 2. Mixture compositions and predicted equilibrium atomic sodium concentrations for the gas-phase and propellant flames.

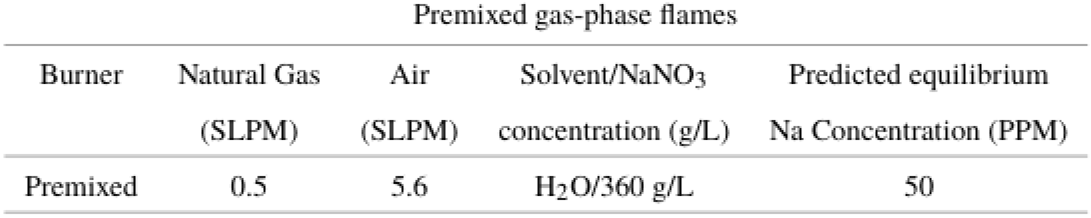

Premixed gas-phase flames

Burner	Natural Gas (SLPM)	Air (SLPM)	Solvent/$NaNO_3$ concentration (g/L)	Predicted equilibrium Na Concentration (PPM)
Premixed	0.5	5.6	H_2O/360 g/L	50

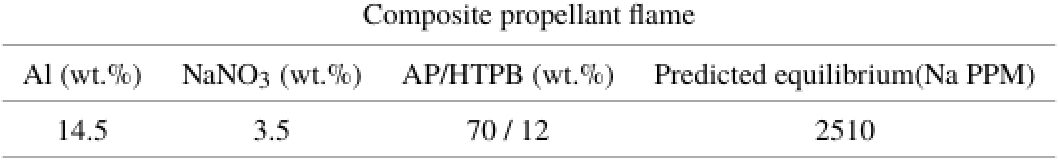

Composite propellant flame

Al (wt.%)	$NaNO_3$ (wt.%)	AP/HTPB (wt.%)	Predicted equilibrium(Na PPM)
14.5	3.5	70 / 12	2510

4.4. Combustion Diagnostics

4.4.1. Laser-induced Fluorescence Measurements

The nanosecond laser-induced fluorescence system used for all excitation schemes is shown in Figure 6(c). A 10-Hz Spectra-Physics Quanta-Ray Nd:YAG laser, operating at ~200 mJ/pulse at 532 , was used to pump a Continuum ND 6000 dye laser with Exciton Rhodamine 640 dye for the 3s–3d excitation of sodium (685-), yielding approximately 20 mJ/pulse. A portion of the dye laser output (10%) was used to monitor wavelength with a HighFinesse Wavemeter WS-6. A + 125-mm focal length lens was used to focus the remainder of light (90%) at the center of the flame for LIF characterization experiments, and a +400- plano-convex cylindrical lens was used to generate a sheet with a thickness of 0.6 mm (10/90 width) and 10 mm height for planar imaging experiments. A fast-gated intensified charge-coupled device (ICCD) camera (Princeton Instruments, PI-MAX 2) with a 55-, f/1.2 Nikon objective lens was set orthogonal to the laser sheet to image the fluorescence. And for the higher magnification PLIF imaging, an Infinity CF2 lens was placed in front of ICCD camera. A 1-inch diameter 820 bandpass filter (Thorlabs, FB820-10, 10 FWHM) was used to detect the 818 fluorescence emission and the ICCD gate was set to a duration of 10 . A digital delay generator (Stanford Research Systems, DG-535) was used to synchronize the laser and camera systems. For the other two-photon excitation 3s–4d at 578 , a mixture of Rhodamine 610 and Rhodamine 640 was used.

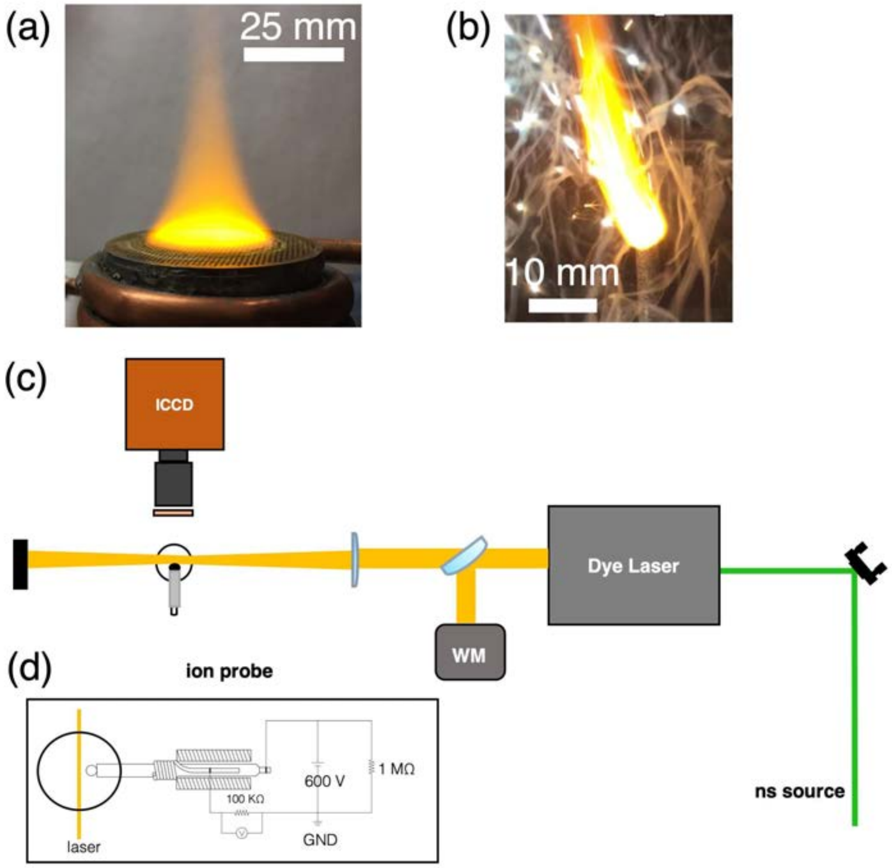

Figure 6. (a) Sodium-seeded premixed flame and (b) sodium-doped aluminized solid propellant flame. (c) The dye-laser excited fluorescence signal was collected with an fast-gate intensified CCD (ICCD) with monitoring via a wavemeter (WM) and ion probe, depicted in inset (d).

For two-photon excitation, a significant degree of ionization and amplified spontaneous emission were expected due to the high sodium levels present in these flames and the low ionization threshold for sodium. Weiland et al. [51] reported data on several two-photon excitation schemes of atomic sodium, but they did not address some of the challenges presented by the high concentrations in sodium-doped propellant flames. In addition, the 3s–3d excitation was not examined. The experimental setup for the measurement of ASE, ionization, and fluorescence is detailed in Figure 6(d). For these tests, the laser was focused to a focal beam waist of 900 with a +200- plano-convex spherical lens. Single-shot monitoring of the laser energy, ASE, fluorescence, and ionization signals was performed with a boxcar integrator (Stanford Research Systems 250) and data-acquisition system (National Instruments, BNC2110). The boxcar integrator was triggered at 10 Hz, and the gated analog signals were captured for each shot by the data acquisition system to allow for correlations between signals. The laser energy was monitored using a photodiode, and the output of the boxcar integrator was calibrated against a power meter. Fluorescence emission for these test was collected with a +60- plano-convex spherical lens onto a photomultiplier tube (PMT, Hamamatsu, H10722-20). An 820 ultra-narrow filter (Alluxa 820-2006) and RG780 longpass filter were used for the PMT. To collect forward-propagating amplified spontaneous emission (ASE), a dichroic mirror (Semrock, FF801-Di02) was used to reflect the excitation laser and transmit the 818 ASE signal. For collection, the expanding ASE signal beam was focused onto a photodiode (Thorlabs, DET36A) using a +150-mm plano-convex spherical lens and filtered with an 820-nm bandpass filter (Thorlabs, FWHM 10 nm).

Finally, to monitor laser-induced ionization, an ionization probe was constructed similar to that developed by Cool et al. [102] for use in low-pressure flames. The probe layout is shown in Figure 6(d), where the anode is a 0.8- diameter spherical bead of platinum on the end of a piece of 0.4-mm diameter platinum wire. A ceramic insulator was used to shield the anode except for the bead end, and the cathode consisted of a platinum wire wound around the first insulator and enclosed by a second coannular ceramic insulator. The probe was set ~2 from the laser focus in the premixed flat flame. The ionization signal was detected with a Tektronix MDO3054 oscilloscope and an attenuating voltage probe (Tektronix P6139B, 10). Acquisitions were AC-coupled to minimize the contribution from the flame ionization signal (a constant voltage offset). For the boxcar integrator measurement, a 1-kHz high-pass filter (100 and 1.5) was used to replace the voltage probe.

4.4.2. Sodium Two-line Thermometry

Utilizing the spectra collected during non-microwave- and microwave-enhanced propellant combustion experiments, the electronic temperature of sodium was estimated based on a pair of emission lines at 589 and 818 nm. Emission at 589 and 818 nm (3p-3s and 3d-3p transitions, respectively) are a result of the electronic excitation of Na by inelastic collisions with atomic and molecular species as well as free electrons. For the applied RMS electric field strength of ~30-90 kV/m, a typical free electron temperature in the microwave plasma might be ~0.5 to 1 eV [103]. The temperature measurement resulting from comparison of the emission strengths of these two lines should lie between the translation and electron temperature for the system. For spontaneous emission from the two transitions considered, the total emission intensity can be written as the product of the spontaneous emission rate, the degeneracy, and the population fraction in the upper state for the transition. Assuming local thermal equilibrium (LTE) [104], a Boltzmann distribution giving the population fraction can be used to infer the electronic temperature of sodium T_{Na} by using the signal intensity ratio for spontaneous emission from two transitions corresponding to transitions from state *j* to *i* and state *n* to *m*. The ratio between signals is given by

$$\frac{\quad}{\quad} = \frac{\eta(\lambda\quad)}{\eta(\lambda\ )}\frac{(\lambda\quad)}{(\lambda\ )}\frac{\overline{\quad}}{\overline{\quad}}, \qquad (15)$$

where g_j is the degeneracy of state *j*, $A_{j,i}$ is the spontaneous emission rate from state *j*, E_j is the energy of the upper state, and k_B is the Boltzmann constant. Constant factors η and *QE* represent the optical collection efficiency and quantum efficiency, respectively, which are constant for each line transition *j,i* or *n,m* tied to the respective transition wavelength $\lambda_{j,i}$. The spontaneous emission coefficients and degeneracies are taken for sodium [105,106] for the given transitions. By writing the ratio of emission bands, factors including the emission collection efficiency, filter transmission functions, and sensor quantum efficiency can be neglected. This was particularly important due to the relative differences in emission intensity between the 589 nm and 818 nm features. The 589 nm emission was attenuated via filtering to allow both features to fit well within the dynamic range of the spectrometer sensor. Spectra were collected during the entire duration of the propellant burn and the integrated emission over each band was taken as the total band intensity. The broadband contribution from blackbody emission due to condensed phase products was baseline subtracted and the intensity of both 589 nm and 818 nm bands were calculated by integrating emission from the two peaks.

Sodium two-line temperature experiments were conducted on burning propellant strands exposed to a 200 ms duration microwave pulse at 1 Hz during the 10 s duration propellant combustion event. The intensity ratios were calculated for each acquisition frame, and were used to determine an average intensity ratio for microwave-irradiated and unirradiated flame conditions. The average signal ratio for the unirradiated case was used to establish a baseline emission peak ratio associated with an estimated temperature given by the adiabatic flame temperature (3032 K). When the microwave was then switched on, the change in the ratio was used to estimate a new temperature by taking the factors η, QE, A, and g, as constant between the two cases. This inferred temperature represents the change in distribution of the states of electronic sodium and we assume these states are in LTE to infer a temperature.

4.4.3. Mg-based Energetic Material Light Emission Measurements

A Phantom v7.0 color complementary metal-oxide semiconductor (CMOS) camera and Canon zoom lens were used to capture high-speed video of the energetic material combustion (500 Hz, 10 to 100 µs exposure). To monitor the VIS/NIR spectral emission, an Ocean Optics USB4000 spectrometer (200 to 900 nm, 25 µm slit, 600 lines/mm, ~100Hz, 10 ms integration time) was used with an OceanOptics multimode fiber (400 µm diameter, P400-0.25-SR). Light was collected onto the fiber end using a cosine corrector (OceanOptics, CC-3-UV-S) to capture a large field of view within the white (optically reflective) microwave cavity. Prior to testing, the VIS/NIR spectrometer was calibrated using a deuterium tungsten-halogen light source (OceanOptics, DH-2000-CAL) to correct for detector responsivity and achieve relative spectral irradiance measurements. Emission spectra were post-processed using MATLAB to correct for dark noise level and detector responsivity. From calibrated spectra, measures of time-integrated spectral emission were calculated as

$$(\lambda) = \frac{1}{\qquad}\sum \quad (\lambda, \quad), \tag{16}$$

where (λ) is the time-integrated relative spectral irradiance per gram energetic material for the entire burn (arb. units per gram), m_{sample} is the energetic material article mass, F_s is the spectrometer sampling frequency, $\left(\lambda, \quad\right)$ is the relative spectral irradiance, λ is wavelength, and t_i is experimental time. A measure of time-integrated emission is calculated by numerically integrating (λ) over all wavelengths between 400 to 880 nm. Emission outside of this spectral range suffered low signal to noise levels and was omitted from the analysis.

The dominant visible wavelengths from the energetic material flame emission were calculated for comparison on a CIE 1931 chromaticity diagram. In doing so, the procedure of Ref. [107] was followed. Briefly, tristimulus values for each spectrum in the time series,

$$(\ ) = \int_{\lambda=0}^{\infty} (\lambda,\ )\bar{\ }(\lambda \qquad (\ ) = \int_{\lambda=0}^{\infty} (\lambda,\ )\bar{\ }(\lambda \qquad (\ ) = \int_{\lambda=0}^{\infty} (\lambda,\ )\bar{\ }(\lambda \tag{17}$$

were calculated, where $(\ )$, $(\ )$, and $(\ )$ are the tristimulus values of the relative spectral irradiances in the time series, and $\bar{\ }(\lambda)$, $\bar{\ }(\lambda)$, and $\bar{\ }(\lambda)$ are the CIE 1931 two-degree field of view color-matching functions. The chromaticity coordinates, $(\ )$ and $(\ )$ of each spectrum in the time series are then calculated as

$$(\ ) = \frac{(\ )}{(\ )\quad(\ )\quad(\ )} \qquad\qquad)\ = \frac{(\ )}{(\ )\quad(\ )\quad(\ )}\,. \tag{18}$$

To capture the infrared emission spectra, a Spectraline ES200 IR spectrometer (1.2 to 5.5 μm, 1,320 Hz, ~0.03 μm resolution) was used. The collection angle of the spectrometer is 0.5 degrees and captured an approximately 0.5 mm wide by 6 mm tall area at the experimental distance. This sampling volume was positioned 25 mm above the energetic material sample. As such, unlike visible spectra, which are representative of entire flame emission, IR emission spectra are from a small volume above the energetic material article and not representative of the entire flame. Prior to use, the IR spectrometer was calibrated using a gray body source placed at the experimental observation distance to produce measures of absolute irradiance. IR emission was post-processed in MATLAB to calculate time-integrated emission. The rise time of the E-field is expected to be short (on the order of milliseconds or less), which is much shorter than UV/VIS instrumentation that is used to assess the degree of light emission enhancement.

4.4.4. Wrapped Thermite Microwave Ignition Delay Measurement

Microwave ignition delays of thermites were measured in a single-mode, impedance-matched, resonant microwave cavity fitted with a microwave combustion applicator. Cavity energy was supplied by a circulator-protected 2.46 GHz continuous-wave (CW) magnetron (National, 2M107-825, 1 kW output), which was powered by a DC power supply (Glassman High Voltage Inc., LT5R400, 1.8 kW output). The field was launched into a WR284 waveguide cavity and propagated in a TE_{10} resonant mode. The cavity is impedance matched to the load using a three-stub tuner, and calibrated, rectifying Schottky diodes (Pasternack PE8003) were used to monitor forward and reflected microwave power via a high-speed oscilloscope (Tektronix MSO 70404C). The microwave applicator consisted of a modified rectangular waveguide section containing two optical access ports in the E-plane and gas inflow/outflow choke-modified ports in the H-plane (Gerling Applied Engineering, GA6002A). To prevent exposure of microwave components to thermite combustion products, the applicator is modified by insertion of two 19.81 mm thick press-fit polytetrafluoroethylene (PTFE) blocks on both sides of the applicator. To prevent contamination of the cavity, smoke is evacuated from the cavity by light vacuum application to the top applicator choke. The cavity is terminated by a sliding short circuit, which is adjusted to generate a standing wave electric field antinode at the thermite location. To match cavity impedance to that of the thermite composite load, an empty PTFE bowl was placed in the cavity and the stub tuner was adjusted to minimize reflection. The quality factor (Q-factor) of the unloaded microwave resonant cavity was measured utilizing a vector network analyzer (VNA, Anritsu MS46322A Shockline) and was determined to be ~985. The electric field strengths are estimated to be from ranges of 38 to 108 kV m^{-1}. Additional details of the experimental setup are available in Ref. [29].

For each ignition delay experiment, each thermite composite (~ 20 mg) was placed in a PTFE bowl, which was positioned atop a PTFE stand in the microwave applicator. A new PTFE bowl was utilized in each experiment to avoid any contamination from previous thermite combustion. Thermites were microwave illuminated till ignition and microwave illumination was continued for ~5 s after ignition. For thermite formulations where no ignition occurred, the sample was continually microwave illuminated for up to ~60 s at which time the field was turned off.

Emission from the thermite ignition and combustion was observed by a photo diode (Thorlabs, DET10A) and a high-speed camera (Phantom ir300 with Nikon Micro-NIKKOR 60mm f/2.8D lens at 500 Hz acquisition rate). Image magnification was ~63 pixel cm^{-1}, with a corresponding field of view of 9.5 by 12.7 mm^2. To measure ignition delay, the photo diode and rectifying Schottky diodes were acquired via high-speed oscilloscope and a custom MATLAB program was used to measure the difference in rise time. Ignition delay was defined as the difference between the 50% rise of the forward power diode measurement and first light emission measured as 10% increase in voltage signal of the photo diode (maximum 5 V). The microwave, high speed camera, and oscilloscope utilized a digital delay generator (Berkley Nucleonics Corp., Model 575) to trigger all events. Experiments on all formulations were performed in triplicate.

4.5. rGO, GO-wrapped Thermite Characterization

Scanning electron microscopy (SEM) images were taken of thermite composites to characterize the physical wrapping of the r-GO sheets on the nanoparticles using a FEI Quanta 250 FE-SEM microscope, with accelerating voltage of 10 kV at working distances of 300 µm to 600 nm. X-ray photoelectron spectroscopy (XPS) analysis of neat r-GO and GO powders, and thermally reduced GO/thermite composites was conducted using a Kratos Amicus X-ray photoelectron spectrometer to determine the extent of GO reduction as a function of heat treatment time.

Thermal decomposition behavior of the composites, and their precursors was analyzed using simultaneous thermogravimetric analysis (TGA) and differential-scanning calorimetry (DSC) with coupled mass spectroscopy (MS) of evolved gas. TGA and DSC data was collected using a Netzsch STA449 F1 Jupiter DSC/TGA instrument while MS data from mass/charge ratios of 10 to 100 were collected with a MS module (Netzsch QMS 403 C Aeolos) connected to the DSC/TGA instrument by a borosilicate capillary transfer line. Prior to running trials, the DSC/TGA furnace was evacuated and argon purged twice. Each trial was conducted in an inert environment, using a constant flow (20 mL min^{-1}) of UHP argon, and was calibrated using an empty crucible to mitigate artifacts from the instrument. Four different materials were evaluated including the individual components n-Al/n-Fe_2O_3 thermite, GO, washed GO, and thermites wrapped in GO. Five to fifteen milligrams of each sample were added to an alumina crucible and heated from 100 to 750 ºC at a rate of 10 °C min^{-1}.

4.6. Dielectric Property Measurement

Calibration and measurement procedures were followed based on the National Institute Standard and Technology (NIST) standard for transmission line dielectric properties measurement [108]. Prior to dielectric property measurement, the VNA was calibrated with WR-284 sliding short and waveguide section via the short-short-short-thru (SSST) method to establish the reference planes. Composite propellant test articles were placed into WR-284 waveguide sample holder. An Anritsu Shockline MS46322A vector network analyzer was used to measure S parameters (S_{11} and S_{21}) at 0.002 GHz intervals from 2.30 GHz to 2.65 GHz (Fig. 7,8). Propellant articles are assumed to be perfectly dielectric, with real permittivity (μ') of unity and imaginary permittivity (μ") of zero. This is because the propellant under test only contains AP, $NaNO_3$, Al, and HTPB, all nonmagnetic material. From these measurements the real and imaginary parts of the permittivity, loss tangent and conductivity are obtained utilizing the Nicholson-Ross-Weir (NRW) model [109,110] and Damaskos MUEPSLN post processing software. The NRW method is commonly used to measure dielectric properties of low-loss materials over broadband frequency ranges [110]. Dielectric properties were additionally determined from accurately machined samples of Teflon and compared to literature values to verify both dielectric measurement techniques, and instrumentation calibration.

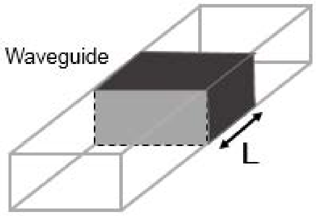

Figure 7. Schematic of propellant test article in waveguide transmission measurement. Propellant test articles are 2.912 cm long (~λ/4 at ~2.7 GHz).

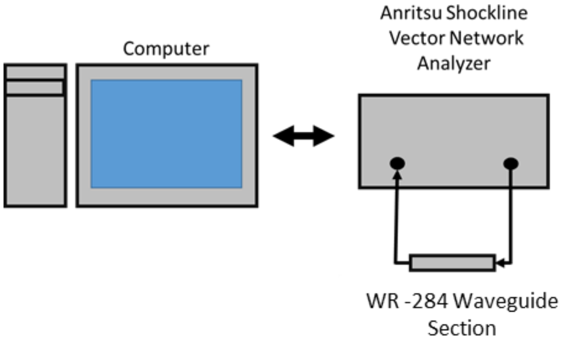

Figure 8. Experimental setups for measuring dielectric properties using the cavity perturbation technique with a vector network analyzer.

1. 5. Results

5.1. Gas Phase Microwave-Energetic Material Flame Interaction

5.1.1. MW Supported Plasma Enhancement of Composite Solid Propellant Combustion

5.1.1.1. Equilibrium Chemical Calculations

Chemical equilibrium calculations were conducted to identify formulations resulting in high equilibrium electron populations. The NASA Chemical Equilibrium with Applications (CEA) code [90] was modified to perform ternary compositional calculations. Calculations were performed with ionic chemistry enabled and at the 0.101 MPa, pressure condition of the experiments conducted in this work. The code was used to calculate atmospheric pressure adiabatic flame temperature ($T_{\text{flame, ad}}$), equilibrium ion/electron concentrations, and equilibrium specific impulse (I_{SP}), which is a measure of the thrust efficiency of a rocket. Specific impulse calculations were conducted with a chamber pressure of 6.89 MPa and an expansion ratio of 68 to match typical solid rocket motor conditions. Calculations were conducted for a range of propellant formulations, varying the weight percentage of aluminum (Al), ammonium perchlorate (AP), and sodium nitrate ($NaNO_3$) dopant from 0 to 90 percentage by weight (wt. %) and using a fixed 12 wt. % hydroxyl-terminated polybutadiene (HTPB) binder.

Equilibrium calculations conducted with varying propellant reactant composition and sodium dopant levels (Fig. 9**)** indicate that Na ion concentration and free electron concentration are optimized for formulations containing ~22 wt. % aluminum, where the highest adiabatic propellant flame temperatures occur and are expected to produce the greatest level of sodium thermal ionization. However, Na ion concentrations are maximized at lower $NaNO_3$ loadings as compared to free electron concentrations. Holding aluminum content constant at 15 wt. %, the overall effect of dopant addition is a reduction in flame temperature and a subsequent decrease in specific impulse (I_{sp}), determined for typical motor pressures of 1000 psi. Replacement of 16 wt. % AP with $NaNO_3$ in a 15 wt. % aluminized propellant (Table 1) is found to reduce I_{sp} by 11 s from 262 to 251 s. However, at lower dopant levels, replacement of 3.5 wt. % of AP with $NaNO_3$ reduces I_{sp} by only 2 s. While higher equilibrium free electron concentrations are accessible with $NaNO_3$ dopant addition beyond 16 wt. %, the associated decrease in I_{SP} performance is significant. However, low dopant additions present an advantageous opportunity to increase free electron populations within propellant flames at the cost of only a small specific impulse reduction.

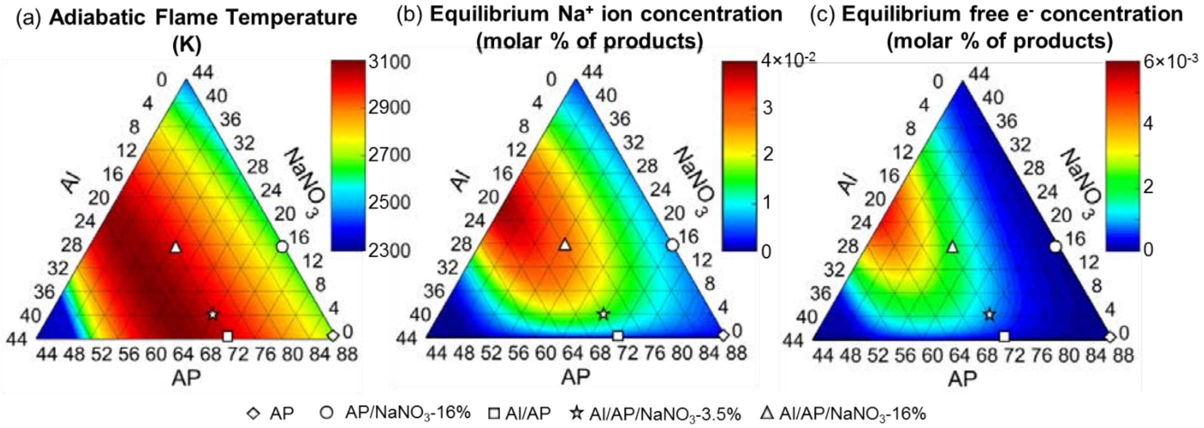

Figure 9. Equilibrium calculation of adiabatic flame temperature (a), Na ion concentration (mol. % of chamber products) as a function of propellant formulation weight percentage (b) and calculation of free electron concentration (mol. % of chamber products) as a function of propellant formulation (c). Calculations are conducted at 1 atm pressure. Each corresponding datum point indicates a corresponding formulation experimentally investigated and shown in Table 1.

5.1.1.2. Electron-Neutral Energy Absorption Calculations

In order to estimate the effect of sodium dopant on microwave energy absorption pathways, solutions to the Boltzmann equation were approximated for a swarm of electrons moving through a representative gas. To select a gas mixture, a constant enthalpy, constant pressure (1 atm) CEA equilibrium calculation was conducted for the aluminized propellant with 3.5 wt. % $NaNO_3$. The equilibrium product mixture was then simplified to create a model gas that could be simulated using a single database of electron cross-section data. To this end, the equilibrium-predicted product species OH, Al_2O_3, Cl, NaCl, AlOH, and AlCl were excluded from the mixture, leaving Na, CO, H_2, H_2O, HCl, N_2, H, CO_2, O, and O_2. The reduced gas composition, reflecting 86.2 mol. % of the CEA-predicted product composition, was then used as an input to the BOLSIG+ software package (Ref. [46], released March 2016), where the Triniti database was selected for the necessary elastic and inelastic cross-section inputs [92]. The complete description of this mixture, as well as the relevant CEA and BOLSIG+ inputs, are available in a supplementary data file. The product atomic sodium mole fraction in the CEA calculation was 0.245 mol. %, which corresponds to 0.284 mol. % in the representative mixture. Simulations were conducted over a range of reduced fields between 5 to 100 Td. To produce a conservative estimate of high-energy electron processes, electron-electron and super-elastic collisions were neglected, thereby eliminating the need for ad hoc estimates of electron and excited state species concentrations. Neutral gas temperature had a negligible effect on the relevant inelastic processes. Rotational energy absorption was neglected for the high range of reduced field in question.

Results of the BOLSIG+ simulations are displayed in Fig. 10. The electron energy loss rates for each inelastic collision pathway were weighted by the target species mole fraction and grouped into vibrational, electronic, and ionization pathways. All non-sodium species were grouped together. Analysis of the BOLSIG+ data showed that the most favorable targets for vibrational energy coupling were, in decreasing order, H_2O, CO, HCl, H_2, and N_2. Additionally, the trend lines for ionization suggest that a mole fraction of only 0.284% atomic sodium is capable of absorbing significantly more field energy for the purposes of ionization than the rest of the gas mixture. Sodium excitation and ionization is expected to be more favorable than other species due to the low electronic and ionization energies, and over the range of 40-80 Td, the absorption of field energy into electronic excitation is dominated by inelastic electron collisions with atomic sodium. This significant increase in ionization is observed in experiments, to be discussed in the experimental results to follow. Additional simulations neglecting sodium confirmed that the energy absorption rates for the remainder of the gas mixture were not significantly modified by the presence of sodium.

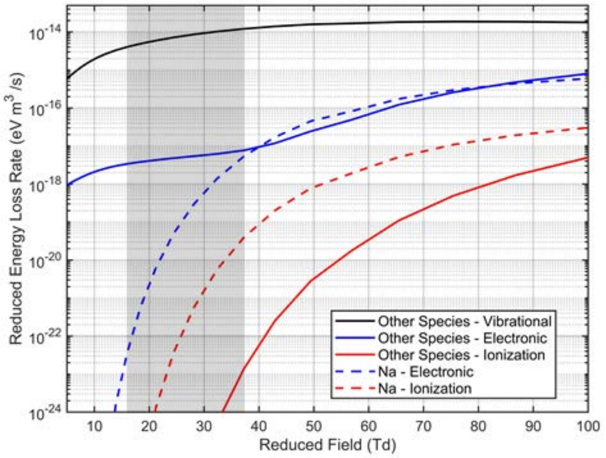

Figure 10. Electron energy loss rates, normalized by number density, are shown over a range of simulated reduced field strengths. Sodium pathways are plotted individually, with the remaining species (CO, H2, H2O, HCl, N2, H, CO2, O, and O2) summed together. RMS field strength at each reduced field value is reported using the temperature and pressure conditions described in Table 1 to obtain ideal gas number density. The grey region indicates the estimated range of reduced fields observed in the following experiments.

5.1.1.3. NaNO3-Doped Propellant Design and Manufacturing

Five different composite propellant formulations were designed based upon CEA equilibrium calculations of Na ion and electron concentrations. To investigate the mechanism of alkali doping of the flame, both unaluminized and aluminized composite propellants containing several degrees of $NaNO_3$ dopant were manufactured. The propellant formulations, shown in Table 3, consisted of aluminum (~35 µm, Valimet-H30), AP (200/90 µm, 80/20 coarse/fine wt. %, Firefox Chemicals), $NaNO_3$ (Firefox Chemicals), and an HTPB binder system. Prior to propellant fabrication, $NaNO_3$ was milled and sieved to achieve particle sizes of < 75 µm and propellant solids were dried under roughing vacuum at 50 ºC for one day. The binder system consisted of R45 monomer (Firefox Chemicals), isodecyl pelargonate (IDP, Firefox Chemicals) plasticizer, HX-878 (tepanol, Firefox Chemicals) bonding agent, and IPDI isocyante curative (Firefox Chemicals). The propellant formulations were mixed for three hours in a dual planetary mixer and deaerated at room temperature and under roughing vacuum for 30 minutes. Strands were cast into 6-mm-diameter cylinders using polyethylene molds and allowed to cure for seven days at 60 °C in an explosion proof oven. After curing, propellant strands were cut to ~2 cm lengths. Measured densities of cured propellants were greater than 95% of theoretical maximum density (TMD). For combustion experiments, the surfaces of propellant strands were inhibited to prevent flame spread down the sides of the burning strands.

Table 3. Solid propellant formulations with corresponding equilibrium predictions of electron mole fraction ([e-]), equilibrium specific impulse (ISP), adiabatic flame temperature (Tflame,ad), and experimentally observed atmospheric pressure propellant burning rate (rb) with and without microwave enhancement. All formulations contain ~12 wt. % HTPB binder. Specific impulse (ISP) is computed with a chamber pressure of 6.89 MPa with an expansion ratio of 68. All other data are computed/measured at 1 atm pressure. Burning rates (rb) are reported as the average and standard deviation of three experiments.

Formulation, balance HTPB	$NaNO_3$ Dopant (wt. %)	[e^-] (mol. frac.)	I_{SP} (s)	$T_{flame, ad}$ (1 atm), (K)	r_b w/o MW (mm/s)	r_b w/ MW (mm/s)	r_b Enhancement
AP (88 wt. %)	0%	1.11x10^{-10}	251	2713	1.17±0.008	1.20±0.031	3.0%
AP/$NaNO_3$ (72/16 wt. %)	16%	8.65x10^{-7}	240	2664	0.624±0.028	0.753±0.047	20.7%
AP/Al (73/15 wt. %)	0%	2.13x10^{-7}	262	3031	1.07±0.039	1.17±0.027	10.1%
AP/Al/$NaNO_3$ (70.4/14.5/3.5 wt. %)	3.5%	7.54x10^{-6}	260	3032	0.988±0.017	1.26±0.015	27.5%
AP/Al/$NaNO_3$ (57/15/16 wt. %)	16%	2.03x10^{-5}	251	3011	0.522±0.012	0.847±0.006	62.3%

5.1.1.4. Microwave Effects on Flame Structure and Plasma Formation

Experiments were conducted for aluminized and unaluminized formulations of varying $NaNO_3$ content. For these experiments, with estimated RMS electric field strengths of 38-91 kV/m, visible light emission was significantly enhanced during microwave application for all propellant formulations. In Fig. 11, still image sequences are shown for each propellant formulation burning both with and without microwave field application. For propellants without microwave enhancement (Fig.11, left), the structures and emission intensities of flames from all propellant formulations appear uniform over the three-millisecond duration of the image sequences. Under microwave application (Fig. 11, right, and in supplementary video), flame emission intensity increases by ~4-13 times for all the propellant formulations. In comparing image sequences of microwave-enhanced flames, the advantageous effects of dopant addition in promoting ionization and electronic state populations and enhancing overall microwave coupling are demonstrated.

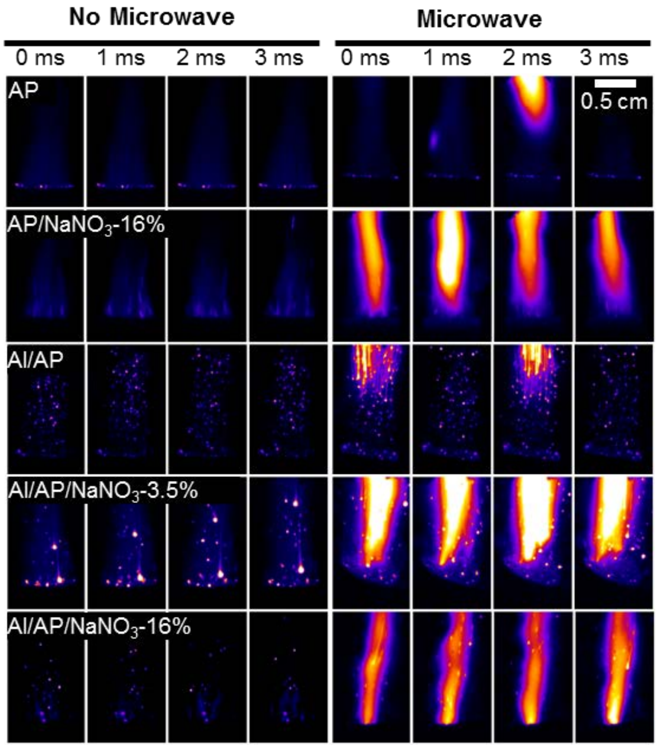

Figure 11. Still frame image sequences of the combustion emission of all formulations without (left) and with (right) microwave field application. Frames are shown with an inter-frame spacing of 1 ms. False coloring is used to indicate emission intensity. Camera exposure and aperture settings are the same for each formulation with and without microwave.

Propellants without $NaNO_3$ dopant exhibit periodic plasma formation and emission enhancement. Energy deposition to these propellant flames suggests that even without a dopant, the flame temperatures are high enough, local electron populations are high enough, and densities are low enough to allow the rapid ionization of products and the formation of transient localized plasmas. The periodic emission seen in AP and Al/AP formulations without sodium dopant addition suggests the local electric field strength is only sufficient to sustain a plasma for short durations. One possible and significant source of electrons within undoped, unaluminized flames is from impurities in the propellant ingredients. Emission spectra (not shown) from microwave-irradiated, undoped, unaluminized AP composite propellant flames indicate calcium, potassium, and sodium atomic species and CaCl molecular species from the combination of the impurities with flame species [111]. Enhanced flame regions in undoped propellants are also not anchored with respect to the burning surface and can be seen translating away from the burning surface with the product flow. Finally, the periodic nature of these emission features suggests that other effects like field-induced polarization or local field enhancement due to local structures such as aluminum agglomerates may be important.

In comparing emission image sequences of undoped AP and Al/AP propellants, there are several distinct differences in microwave coupling regions which occur with the addition of aluminum to the propellant formulation. Within unaluminized AP propellants, kernel formation and growth are observed to occur within the propellant gas phase as shown by the diffuse structure of the luminous region during microwave field application. Within aluminized AP composite propellants, significant emission enhancement can be observed from long vertical structures. The unique emission enhancement structure of aluminized propellants that results from microwave irradiation is suggestive of either ionization of atomic aluminum (5.99 eV ionization energy) or aluminum diffusion flame structures via another mechanism. Addition of $NaNO_3$ dopant in microwave-irradiated propellant strands is found to stabilize emission enhancement by anchoring plasma regions close to the propellant burning surface. Enhanced near-burning surface anchoring was observed to be improved in propellants with increased $NaNO_3$ dopant concentration and/or with aluminized formulations. The most effective anchoring was observed in 15 wt. % aluminized propellants containing 16 wt. % $NaNO_3$ dopant, which have the highest equilibrium-predicted free electron population of all experimentally investigated formulations.

Estimates for the Na electronic temperature were made using the ratio of two Na spontaneous emission lines in aluminized, 3.5 wt. % $NaNO_3$-doped propellant flame with and without microwave enhancement. From the emission ratio, the sodium temperature difference was calculated from the 818/589 nm ratio, as previously described. Briefly, the mean of the ratio without microwave application was assigned a temperature corresponding to the adiabatic flame temperature calculation. To determine a temperature increase, the baseline ratio was calculated for the situation with no microwave application. The emission ratio during the application of the electric field was then measured, as shown in Fig. 12. The measured 818/589 nm ratio of a propellant flame is approximately 4 times higher as a result of microwave irradiation, indicating an increase of sodium electronic temperature of ~1000 K. In addition, the absolute emission intensity increased by a factor of ~4 for the 589 nm emission and ~16 for the 818 nm emission. The increase in the relative rate of emission from these states suggests both an increase in temperature and a potential increase in the processes resulting in population of the excited states of atomic sodium. These processes likely consist of inelastic collisions of sodium with excited atomic and molecular species as well as inelastic collisions with electrons. The increase in equilibrium-predicted electron population (without microwave irradiation) and the microwave-induced sodium temperature enhancement indicate the important role of an alkali dopant such as sodium in lowering the threshold for microwave absorption and initial plasma formation in the propellant flame.

Collectively, these results suggest that electron populations within both aluminized and unaluminized composite solid propellant flames, regardless of whether a dopant is used, are high enough to couple with and allow energy deposition from a ~38-91 kV/m, 2.46 GHz E-field, and that energy deposition results in significant excitation of electronic states and emission enhancement. While the enhancement from undoped propellants appears periodic and unanchored, addition of either or both sodium nitrate dopant and aluminum to a propellant more effectively anchors plasma-enhanced regions near the propellant burning surface. Application of a microwave field to a sodium-doped propellant flame results in significant increases in sodium temperature and sodium emission intensities. Both of these observations suggest that microwave irradiation results in large increases in free-electron populations and an increase in excitation of electronic states of sodium, which occur through inelastic collision with electrons and excited neutrals. Although absolute electron number density is not estimated, these results are consistent with the formation of a low density plasma controlled by the application of the microwave field.

Plasma enhancement has been shown to play an important role in other reacting systems, where the processes can be classified as mainly thermal (where populations are in LTE) and non-thermal, where certain species may be far from equilibrium and may result in the activation of additional important kinetic pathways [112]. These pathways may well be important for the propellant microwave-enhancement but are not directly observed on the timescales in this experiment. Ultimately, the burning rate enhancement is largely due to thermal feedback from the various energy deposition mechanisms to the propellant burning surface. However, the individual processes resulting in thermal energy transfer may be rate-limited by processes which deviate from thermal equilibrium and include the production of significant radical populations.

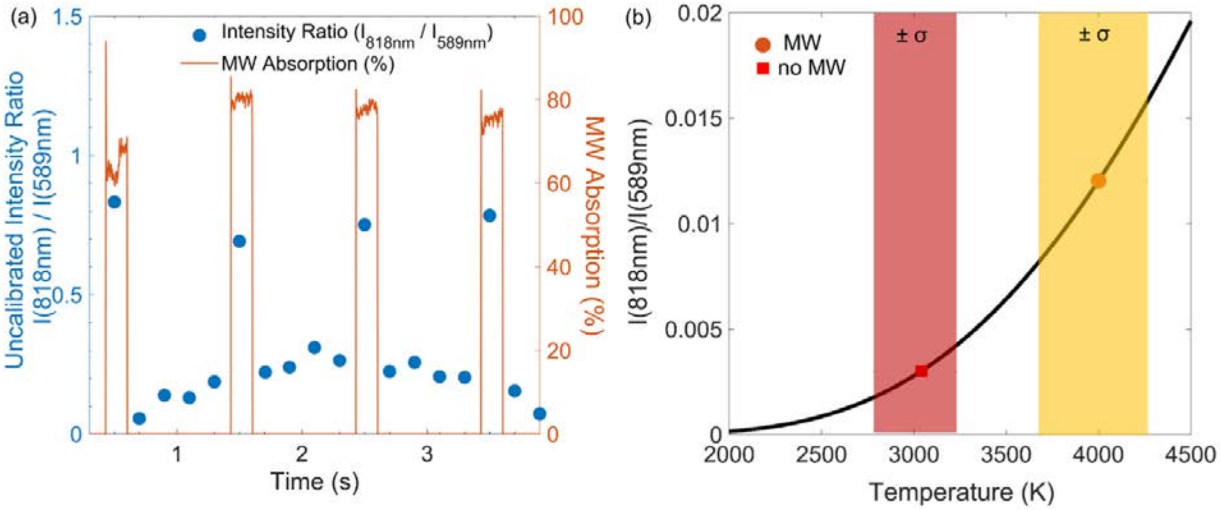

Figure 12. (a) Time history of line intensity ratio shown with the microwave absorption during a propellant burn with a 20% duty cycle modulated microwave field. (b) Average inferred sodium electronic temperature of aluminized, doped composite propellant (Al/AP/NaNO3-3.5%) with and without microwave enhancement. Banded temperature regions indicate temperature ranges corresponding to +/- one standard deviation of measured sodium band emission intensity ratios for three propellant strand combustion experiment.

5.1.1.5. Oxide Thermal Runaway Dielectric Absorption

From image sequences of microwave-enhanced propellant combustion (Fig. 13), energy deposition to aluminized propellant flames differs from unaluminized propellants significantly. In the aluminized AP propellant without dopant (Al/AP/HTPB), connected vertical emission-enhanced features are observed. The typical aluminum agglomerate flame structure consists of a molten aluminum droplet/agglomerate, an attached lobe of aluminum oxide, a diffusion flame, and a condensed aluminum oxide smoke trail. High magnification imaging of the aluminum diffusion flame of an undoped propellant flame (Fig. 13 and supplementary video) show that with field application, increased luminosity and emission is observed in both the aluminum oxide condensed smoke and the aluminum oxide lobe attached to the burning aluminum agglomerate. Field application results in growth of the aluminum diffusion flame envelope in small aluminum agglomerates (~100 μm diameter and smaller), indicating faster liquid aluminum volatilization rates due to increased heat transfer to the aluminum through conduction (contact with the oxide lobe) and radiation (feedback from the oxide smoke envelope).

The image series in Fig. 13 and supplemental video shows increased aluminum oxide luminosity of approximately 2 times as a result of energy absorption. This increase in graybody luminosity suggests increases in the aluminum oxide condensed phase product temperatures, which is hypothesized to result from strong dielectric microwave energy absorption by the aluminum oxides products. While the microwave-frequency dielectric absorption (tan δ) of aluminum oxide at room temperature is low (tan δ = 0.0003), at elevated temperature the dielectric absorption increases exponentially due to electron promotion to valence shells. At an elevated temperature of 1500 K, the loss tangent of aluminum oxide is 300 times higher than at room temperature [113,114]. In an aluminized propellant combustion environment, where the surface of an aluminum agglomerate is at the aluminum boiling temperature (~2740 K, 1 atm) and aluminum diffusion flame temperatures are in excess of this temperature, microwave energy deposition to oxide products is expected to be even more efficient. The efficient deposition of microwave energy to aluminum oxide in a thermal runaway condition is similar to behavior demonstrated in several oxides [113,114]. As burning aluminum particles are convected away from the propellant burning surface, microwave energy deposition is localized in the hot aluminum oxide products and this process continues until the hot products convect out of the microwave cavity.

Within a composite solid propellant, the ability to enhance the temperature of the high emissivity, high specific surface area oxide product smoke of burning metals is of high utility, as radiation heating of a propellant burning surface is significant. The maximum oxide smoke temperature that can be achieved through microwave irradiation enhancement is limited thermodynamically by the oxide boiling temperature (3250 K, Al_2O_3, 1 atm). Thermodynamic scaling of these limiting conditions to a 2.03 MPa rocket motor environment with 900 K propellant burning surface temperature [115] and ~5000 K oxide volatilization temperature shows the energy envelope for sensible enthalpy enhancement of aluminum oxide is large. The nanoscale oxide smoke from aluminum diffusion flames within composite solid propellants are high flux emitters which re-radiate energy to the propellant burning surface and may provide significant, microwave-controlled enhancement to the propellant burning rate.

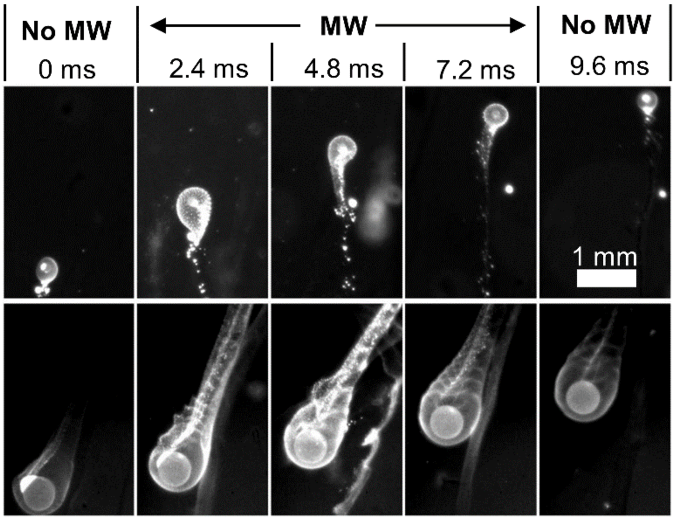

Figure 13. Two representative high magnification image sequences of microwave combustion enhancement of a small (~150 µm, top panel) aluminum agglomerate and large (~600 µm, bottom panel) agglomerate near the burning surface of an Al/AP/NaNO3-3.5% propellant with microwave field modulation at 60 Hz. The average pixel intensity of images in the bottom panel approximately doubles as a result of microwave application.

5.1.1.6. Microwave Energy Partitioning and Burning Rate Enhancement

The two previously described mechanisms (plasma formation and energy deposition to the gas phase, and dielectric loss to aluminum oxides) are expected to result in enhancement of composite solid propellant burning rate through improved heat feedback to the burning surface. In addition, it is expected that some microwave energy may be deposited directly to the condensed phase of the composite solid propellant through both dielectric loss and for aluminized propellants, Maxwell-Wagner losses [116]. The total amount of incident microwave irradiation absorbed by both the propellant flame and condensed phase is apparent from comparing both forward and reflected power measurements over the duration of a propellant combustion experiment (Fig. 14(a, b)). Energy absorption remains high over the duration of the experiment (~60-90% absorption) but decreases as propellant combustion progresses, which is due to either cavity detuning or reduced condensed phase loss (Fig 17(a)).

In order to quantify the partitioning of microwave energy deposition to either the gas phase flame or directly to the propellant condensed phase, measurements of the condensed phase absorption of Al-AP-$NaNO_3$-3.5 wt. % propellant were taken as a function of strand height within the microwave applicator cavity. These were compared to online absorption measurements of the same propellant burning within the cavity (Fig. 14(b)). During experiments, however, it was observed that for some formulations, flame spread occurred down the sides of latex-coated propellant strands, resulting in nonplanar burning surfaces and artificially enhanced burning rates. Flame spread is likely due to either/both dielectric absorption of the latex inhibitor or plasma erosion of the surface. To prevent flame spread, propellant strands were burned within the 0.38 mm thick polyethylene tubes in which they were cast. The complex permittivity of polyethylene is relatively low (0.0005 at 1 GHz) and thermal loss to the polyethylene tube is low. As a result, there is only ~5% difference in burning rates between latex-coated (uninhibited) and polyethylene-coated (inhibited) propellant combustion rates (Fig. 14b).

Considering the partitioning of energy to the flame or condensed phase (Fig. 14b), at the beginning of propellant strand burn experiments (strand height ~2 cm), absorption is high and is observed to decrease as the burning surface regresses. The absorption of the condensed phase remains high (~60%) from the beginning of the burn until strand height has regressed to ~1 cm and then decreases. A local absorption maxima of all burning propellant strands (flame present) were observed at a height of ~1 cm, which could be due to the shift in the cavity resonance during the burn, as the cavity was optimized for maximum quality using a half-height propellant strand. In comparing absorption of both the condensed phase and propellant with flame, roughly 20-25% of the incident microwave energy is deposited to the propellant flame structure and 40 to 60% is deposited to the condensed phase, while the remainder is reflected.

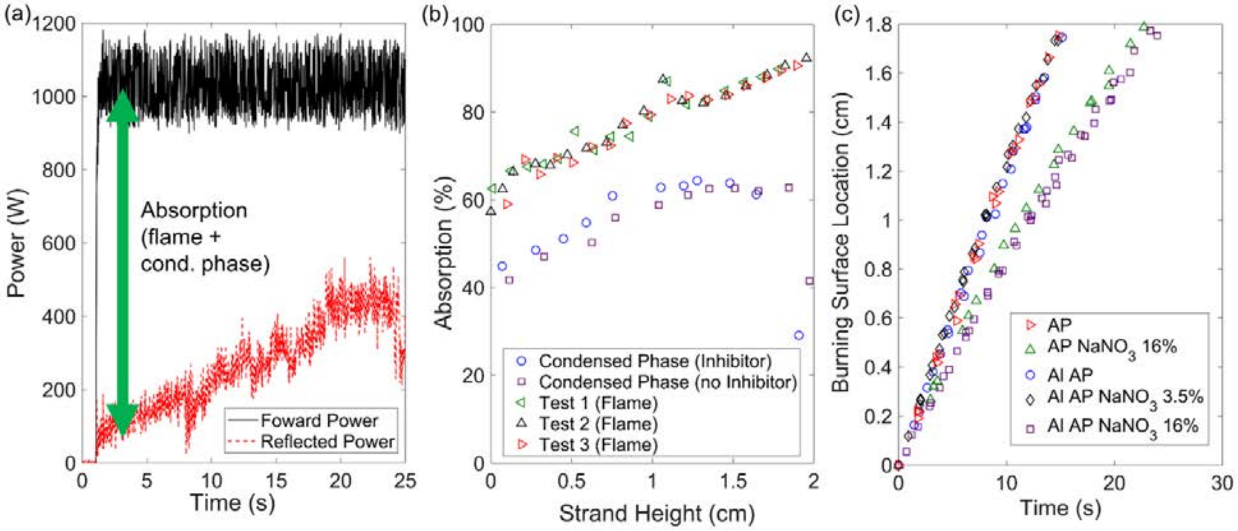

Figure 14. (a) Typical forward and reflected microwave power measurements taken during Al-AP-NaNO3 combustion. (b) Typical microwave absorption measurements from three experiments conducted with an Al-AP-NaNO3 3.5 wt. % propellant as a function of propellant strand height within the cavity for both propellant condensed phase (no flame, with and without polyethylene inhibitor tube) and burning propellant (flame and condense phase present in microwave cavity). The propellant height was measured with respect to the bottom of the optical viewing window. (c) Typical measurements of burning surface location as a function of time for all formulations under microwave field application.

The burning rates of composite solid propellant formulations studied in this effort were measured both without and with microwave irradiation through direct measurement of the regression surface location in time (Fig. 14(c)). In measurement of burning surface location with time, no acceleration of burning rate in time is observed in the formulations, which suggests microwave absorption directly by the condensed phase is not primarily responsible for burning rate enhancement. Average burning rates of propellants both with and without microwave irradiation are shown in Table 3. A decrease in unenhanced burning rate from the addition of $NaNO_3$ is observed in both the unaluminized and aluminized propellants. We attributed this to presence of a nitrate oxidizer. Slow burning rates of ammonium nitrate (AN) composite propellants are pervasive, and AN propellants suffer from excessively high low pressure deflagration limits (above 1 MPa); reasons for slow burning rates are myriad and are described in a review by Jos and Mathew [117]. We expect some of the same complications with sodium nitrate composite propellants. The microwave burning rate enhancement of undoped, unaluminized propellant was 3%, and addition of 16 wt. % dopant increased the percent microwave burning rate enhancement to 20.7%. Aluminized propellants without dopant exhibited a 10.4% microwave burning rate enhancement as a result of microwave irradiation. Addition of 3.5 wt. % dopant to the aluminized propellant increases microwave burning rate enhancement to 27.4%, and further addition of dopant (16 wt. %) results in a 62.3% burning rate enhancement.

In considering the percentage burning rate enhancement observed with all propellants, we observe that the degree of burning rate enhancement possible under conditions of the experiments is increased by both addition of sodium nitrate dopant and addition of aluminum to the propellant formulation. These findings are supportive of the proposed microwave energy deposition mechanisms, shown in Fig. 15, as (1) sodium nitrate addition increases the equilibrium flame free electron pool, enabling more efficient plasma support within the flame and leads to plasma anchoring nearer to the burning surface, (2) energy deposition to aluminum oxide smoke features can enhance burning rate directly through enhanced thermal irradiation of the burning surface or indirectly through aluminum agglomerate burning rate enhancement, and (3) dielectric heating of the condensed phase can lead to preheating and increases in the surface regression rate.

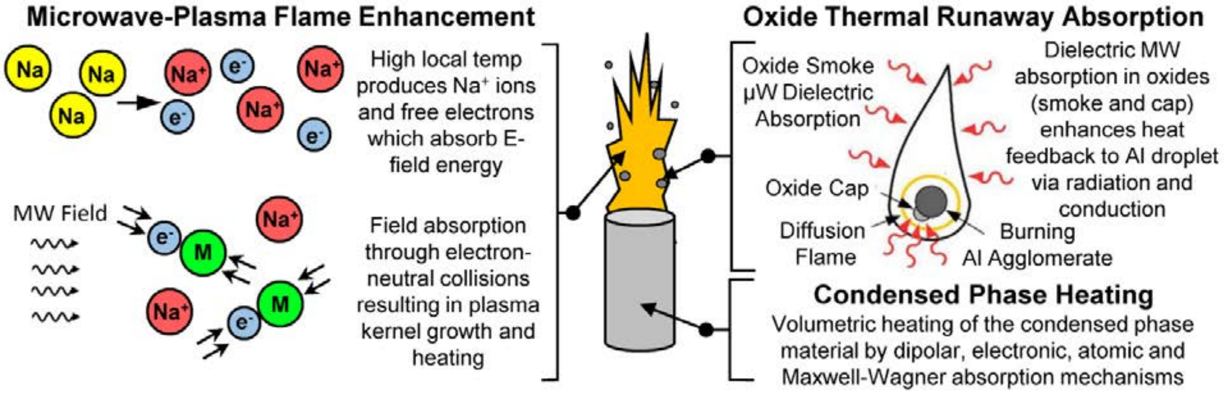

Figure 15. Illustration of proposed mechanisms for burning rate enhancement. Plasma kernel seeding occurs in regions of high local flame temperature (high ion and free electron density) due to electron-neutral collisions and subsequently grows through the flame volume. Energy can also be deposited through dielectric absorptions to high temperature aluminum oxide features (oxide smoke and oxide cap) within aluminum droplet diffusion flames. Condensed-phase heating can contribute to the burning rate enhancement through dielectric absorption mechanisms.

5.1.2. MW Interaction With High Alkali, Mg Containing Energetic Material Flames

5.1.2.1. Equilibrium Chemical Calculation

The predicted adiabatic flame temperature ($T_{adiabatic}$) and prevalent ion and neutral product species of the three energetic material formulations investigated are shown in Table 4. Stoichiometric formulations of Mg/alkali nitrate systems were found to maximize predicted free electron and ion concentration due to high flame temperature. In addition to maximizing free electron populations, the predicted equilibrium products contain several neutral atomic gas species with low ionization and low energy electron transitions (e.g. Na, K, Cs, Mg). From the list of major atomic gas-phase species, transitions with the highest spontaneous emission rates are listed in Table 5. Only Mg I (517.8 nm) and Na I (589.2 nm) are transitions with high spontaneous emission rates that are in the visible spectrum, while Cs I (852.1 nm) and K I (767.6 nm) are transitions with high spontaneous emission rates in the NIR spectrum. Equilibrium calculations indicate that combustion products at adiabatic flame temperature consist of both vapor-phase and condensed-phase species. Contrary to gas phase species, condensed phase species are expected to undergo sensible enthalpy change proportional to species' dielectric loss characteristics when subjected to microwave illumination. The product composition also consists of 1.0 to 3.1 mol.% vapor phase MgO and 31.2 to 35.2 mol.% $MgO_{(cr)}$. As discussed previously, the presence of both condensed phase and gas phase species are important in consideration electric field interaction, as energy absorption by condensed phase is typically by dielectric modes and energy absorption by gas phase species typically occurs by electronic modes. The major neutral gas-phase species shown in Table 4 were used in the 1-D microwave-enhanced emission model.

Table 4. Equilibrium predictions of adiabatic flame temperature and prevalent charged/neutral combustion species of experimental compositions using CEA. Calculations assume atmospheric pressure with 10 wt.% air, and the most prevalent species are noted. For the emission model in Sections 2.5 & 3.4, the gas mixture was derived from normalizing the most prominent gases.

Formulation	**$Mg/NaNO_3$/epoxy (45.6/49.4/5wt. %)**	**Mg/KNO_3/epoxy (42.8/52.2/5 wt. %)**	**$Mg/CsNO_3$/epoxy (28.5/66.5/5 wt. %)**
$T_{adiabatic}$ (K)	3088	3055	2943
Cations (mol.%)	Na^+ - 0.03	K^+ - 0.10	Cs^+ - 0.17
e^- (mol.%)	0.03	0.10	0.17
Neutral Gas-Phase species (mol.%)	64.8	65.4	68.6
	Na - 15.7	N_2 - 15.9	N_2 - 18.1
	N_2 - 15.6	Mg - 15.3	Mg - 15.1
	Mg - 13.4	K - 14.2	Cs - 12.3
	CO - 7.1	CO - 7.9	CO - 11.4
Condensed-phase species (mol.%)	$MgO_{(cr)}$-35.2	$MgO_{(cr)}$-34.5	$MgO_{(cr)}$-31.2

Table 5. Electronic transitions of prevalent gas-phase atoms observed in Mg/alkali-nitrate flames [118].

Species	**Wavelength (nm)**	**Transition**	**Spontaneous Emission Rate, A_{ki} (10^8 s^{-1})**	**Transition Energy (eV)**
Cs I	852.1	6s-6p	0.328	1.455
Na I	819.1	3p-3d	0.495	1.514
K I	767.6	4s-4p	0.385	1.615
Na I	589.2	3s-3p	0.615	2.104
Mg I	517.8	3s3p-3s4s	1.040	2.394

5.1.2.2. Microwave Effects on Flame Structure

Image sequences (Fig. 16) and the supplemental video show an example of the effect of modulated microwave illumination on the flame structure of a Mg/KNO_3/epoxy energetic material. Without microwave illumination, the primary flame intensity varies with a visible flame height between 1 to 1.5 cm. With microwave illumination, flame emission and size modulate in phase with the application of electromagnetic field (60 Hz duty cycle). During the microwave illumination period emission intensity increases and the flame volume grows. The emission region grows to 3 to 4 cm in height from the burning surface. The emission enhancement of the flame is expected, in part, from the high alkali metal content of the formulations, which results in emission from low-lying electronic states [23–27]. For all formulations tested, microwave field application increased both the visible flame volume and emission intensity.

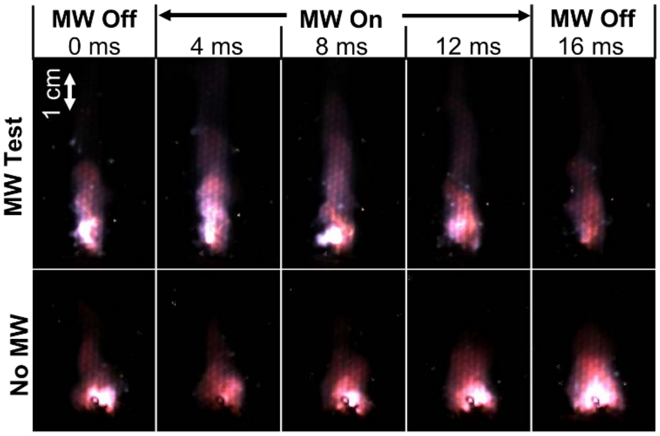

Figure 16. Image sequence of the Mg/KNO3/epoxy energetic material combustion with (top) and without (bottom) microwave illumination, where the microwave field is sinusoidally modulated at 60 Hz. During the microwave illumination period, flame growth and emission increase can be seen above the main flame. Both images are taken with the same exposure and frame rate (20 µs, 500 Hz).

For all energetic material systems evaluated, sustained visible light emission after energetic material flame extinguishment was also observed. The resulting post-combustion emission, shown in Fig. 17, occurs near the top of the multimodal cavity at a probable E-field antinode. The post-combustion products continue to emit periodically in phase with the 60 Hz microwave field modulation for long durations of time (~10 s or longer after energetic material extinguishment).

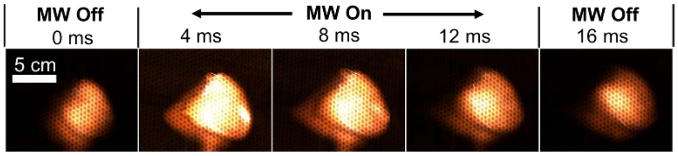

Figure 17. Image sequence of the microwave field enhancement of Mg/NaNO3/epoxy post-combustion products where the microwave field is sinusoidally modulated at 60 Hz. The energetic material article is out of view in these images.

5.1.2.3. VIS/NIR Spectral Emission Enhancement

Time-resolved VIS/NIR emission spectra from combustion of Mg/NaNO$_3$/epoxy energetic materials are shown in Fig. 18. As compared to non-microwave illuminated conditions, significant atomic emission enhancement is detected. For the Mg/NaNO$_3$/epoxy system, enhanced emission was observed at the expected atomic emission lines at 589 nm (Na I, 3p-3s), 819 nm (Na I, 3d-3p), 568 nm (Na I, 4d-3p), 615 nm (Na I, 5s-3p), 670 nm (Li I, 2p-2s), 766 nm (K I, 4p-4s), and 850 nm (Cs I 6p(3/2)-6s). Emission from Li I, K I, and Cs I seen in the Mg/NaNO$_3$/epoxy system is likely due to contamination in the microwave cavity from prior experiments.

The typical combustion duration for each energetic material experiment was approximately four seconds with microwave illumination and five seconds without microwave illumination. Emission from the sustained post-combustion plasma can be seen in the right panel of Fig .18 between experiment times of approximately five to fifteen seconds. The post-combustion emission from the Mg/$NaNO_3$/epoxy system is primarily from atomic sodium emission (Na I, 3p-3s). This effect was also observed in the other two alkali-nitrate energetic material formulations, but to a lesser extent. In all formulations, atomic emission enhancement primarily occurs from the lowest energy electronic transition of the respective dopant alkali atom. By inspection of Eqns. 7 and 9, it is apparent that without substantial electron-alkali excitation or continual heat transfer to maintain plume temperature, sustaining non-equilibrium excited-state alkali population $_2$ is not possible. The long-duration sustained emission is therefore strong evidence that WMIP is directly responsible for generating increased excited-state alkali species, especially for post-combustion periods where the ratio of intensities is nearly infinite.

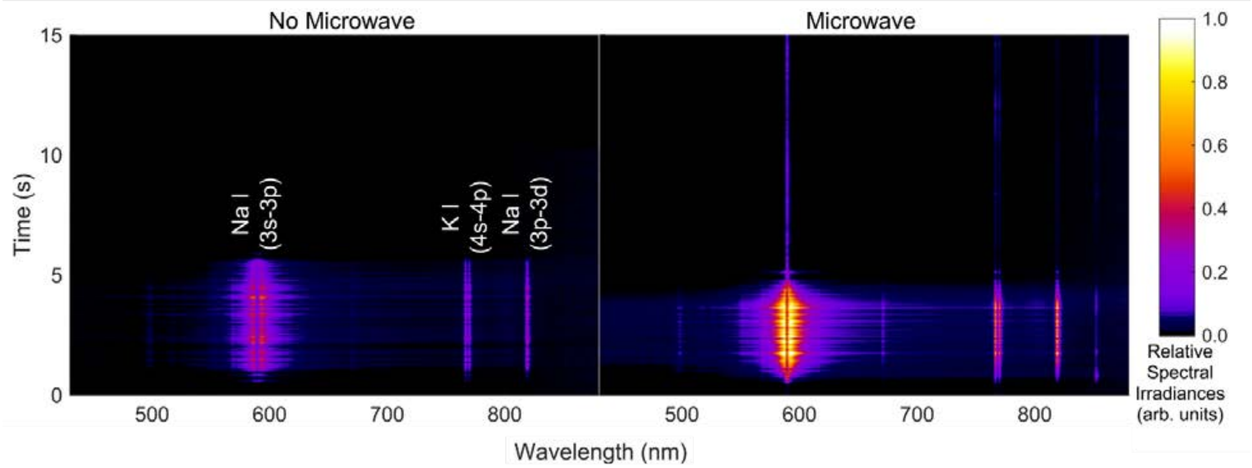

Figure 18. Time histories of Mg/NaNO3/epoxy energetic material combustion emission from the baseline condition (no microwave, left) and with microwave illumination (right). Continuous emission from the atomic species long after energetic material extinguishment can be seen (~5 to 15 seconds) as a result of microwave illumination of combustion products. Spectra intensities are normalized based on detector exposure time such that intensities of the two experimental trials are relative to each other.

Microwave illumination of other Mg/alkali nitrate energetic material systems resulted in atomic emission enhancements similar to Mg/$NaNO_3$ formulations. These results are summarized in time-integrated, VIS/NIR spectral irradiance measures of the three energetic material formulations (Fig. 19a). Similar to the sodium nitrate-based formulation, the majority of emission enhancement observed in both the potassium and cesium nitrate energetic material formulations was due to enhanced emission from low energy electronic transitions from excited state alkali neutrals (Mg/KNO_3/epoxy: K I, 4p-4s, and Mg/$CsNO_3$/epoxy: Cs I, 6p(3/2)-6s). As expected, resonant broadening and self-absorption of the alkali resonance-line continuum is apparent (Fig. 19) without microwave illumination. Self-absorption also occurs in microwave illuminated emission from all formulations, though is not apparent in time-integrated spectra of Fig. 19a due to the additional emission contribution of the microwave-supported plasma that occurs after energetic material extinguishment. Self-absorption and resonance broadening can be more clearly seen in typical time-resolved emission spectra from Mg/$NaNO_3$/epoxy (Fig.19b).

Other, lower intensity peaks are also observed that correspond to additional electronic transitions of the alkali metals. These emission features are noted in Fig. 19a. Some atomic emission enhancement is also observed from contaminant alkali species that are present in the multimode microwave cavity which are excited during combustion and microwave illumination (e.g. Li, Na, K, and Cs). Even though equilibrium-predicted Mg populations are similar to those of alkali metals and spontaneous emission rates are even higher, little Mg I emission is observed for conditions with and without microwave illumination at the two transitions of interest (383.5 nm, 3s3p-3s3d and 517.8 nm, 3s3p-3s4s, shown in Table 5). We postulate that the higher transition energy of Mg I and shorter lifetime of Mg vapor due to oxidization contribute to lower Mg I emission. Additionally, little gray body continuum emission enhancement is observed in VIS/NIR spectra even with high predicted concentration of condensed phase MgO; it is expected that within the combustion plume, microwave absorption primarily occurs to the gas phase plasma.

For energetic material formulations investigated in this effort, microwave energy is expected to be preferentially absorbed electronically to the gas-phase through inelastic electron-neutral collisions rather than dielectrically by the condensed-phase reactants. Some dielectric heating of the condensed phase does occur, however, as demonstrated by microwave-based auto-ignition of energetic material articles which can be achieved after ~40 seconds of microwave illumination. Assuming energetic material article microwave heating is spatially uniform and assuming autoignition occurs between 467 °C and 565 °C [119], and neglecting convective losses, we estimate the average microwave absorption of condensed phase reactants is 6.0 W to 7.3 W. Much of the condensed phase reactant heating is expected to be a result of microwave loss in the metal nitrate. Studies on microwave sintering of Mg particles have found Mg heating to be slow (17.1 K/min, 1.0 kW multimodal cavity) [120]. The dielectric loss of the metal nitrate reagents used in this effort are expected to be higher than Mg particle heating, as the microwave heating rate of ammonium nitrate to ignition has been reported in literature to be on the order of minutes (178.8 K/min, 1.1 kW single mode cavity) [35].

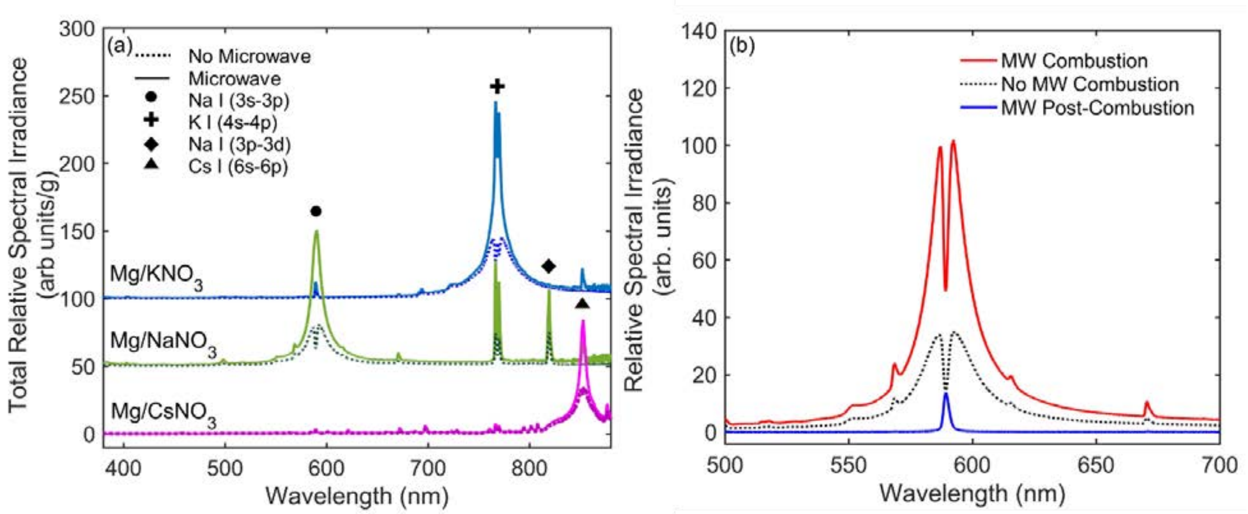

Figure 19. (a) Time-integrated, relative spectral irradiance of each energetic material during combustion, both with and without microwave illumination in arb. units per gram energetic material reagent. Species responsible for strong electronic transition features observed in VIS/NIR emission are noted. Increased emission from atomic transitions can be seen with illumination. Some atomic emission enhancement is also observed from contaminant alkali species that are present in the multimode microwave cavity which are excited during combustion and microwave illumination (e.g. Li, Na, K, and Cs). Spectra intensities are all relative and spectra from each

formulation are offset for clarity. (b) Typical emission spectral features from Mg/NaNO3/epoxy energetic material combustion with and without microwave.

5.1.2.4. VIS/NIR Emission Enhancement Mechanism

In order to compare the proposed model to experimental results, integration of the spectral irradiance from 400 to 880 nm in Fig. 19 was used to produce an estimate of the ratio of time-integrated irradiance with and without microwave exposure (green dots, Fig. 19a). Surprisingly, this emission enhancement was found to correlate positively with shorter wavelength, higher energy, transitions. The energetic material with the highest alkali transition energy, $NaNO_3$, yielded a ratio of 2.2, or 120% increase in time-integrated irradiance when microwaves were applied. Potassium and cesium cases experienced an average of 50% and 20% irradiance enhancements, respectively. These results were compared directly to simulated ratios of radiance computed using Eqn. 14.

Given the challenges in grounding simulation parameters (gas temperature $_0$, field strength , and alkali mole fraction) firmly in measurements, we instead show that a suitable parameter set exists that can replicate all three alkali enhancement ratios simultaneously. Such a case was found for reduced field strength of 42 Td, plume temperature of 2725 K, and an alkali fraction of 6 vol.%, and is within experimental margin of error for all alkali species (blue dots, Fig. 20a). This serves as an initial demonstration of consistency for the WMIP model for energetic material emission enhancement. For comparison purposes, we also present calculations for the same case but with a gas temperature near CEA equilibrium temperatures (red dots, Fig. 20a).

As the reliance of Eqn. 14 on wavelength (or transition energy) could not be obtained by simple inspection of Eqn. 4-13, the various wavelength dependencies within the model were artificially perturbed from line center λ_{21} to identify the dominant terms (solid and broken lines, Fig. 20a). To simplify the results, wavelength parameters λ_- and λ_+ were used to group terms with similar effects on emission enhancement. Specifically, the λ_- group followed the experimental trend of diminishing enhancement with increasing wavelength, whereas λ_+ opposed it. From initial calculations, it was immediately clear that only the wavelength dependence of (Eqn. 9) contributed to λ_-. The λ_+ term contained all other wavelength dependencies, including: (1) calculation of transmittance via optical depth (Eqn. 5), (2) spontaneous emission coefficient (Eqn. 6), and (3) cross-sections for electron-alkali excitation, where cross-section curves were artificially shifted in energy space to correspond to an alternate transition energy ($\Delta\epsilon =$ $_+$). The procedure for altering cross-sections does not account for hypothetical changes in cross-section shape, however the curves are roughly comparable across alkali species, independent of transition energy. Finally, both λ_+ and λ_- were also varied together to show the cumulative sensitivity to wavelength.

With the results displayed in Fig. 20a, a preliminary hypothesis can be constructed to explain why WMIP emission enhancement in the VIS/NIR range is maximized for alkali species with shorter wavelength (higher-energy) transitions. Photons with shorter wavelengths (Eqn. 5) have a diminished probability of escape, which restricts the effect of any enhancement. Likewise, alkali species with an increased energy threshold for electron-alkali excitation collisions $_{+}$ plainly counters the ability of an electric field to promote non-equilibrium emitters. The same can be said for emission coefficient, which increases the baseline emission rate independent of the microwave field by the third power of wavelength (Eqn. 6). Despite these effects, the model for enhancement is most sensitive to neutral-alkali excitation rate (Eqn. 9), which falls off exponentially for transition energies above the gas thermal energy ($> {}_{0} \approx 0.25$ eV). The net effect is that falls off faster with lower wavelength than $_{+}$ (whose rate is field-driven and not limited by equilibrium Maxwell-Boltzmann statistics). Hence, $_{+}$ develops a proportionally larger effect than on emitter population $_{2}$ (and hence, emission rate ϵ) through Eqn. 7.

To further reinforce that this result is independent of parameter selection, simulations at line-center wavelength were conducted across a wide domain of parameter space ($_{0} = [2400, 3000$, $= [0.05, 0.2]$, ,=[20, 45] Td), and the eight combinations were plotted in the background of Fig. 20a. These show that the general trend between the alkalis hold for all but one case. The extraneous limit with very low enhancement was a result of strong shielding properties ($_{0} = 3000$ $= 0.20$, ,=20 Td). To show the parameter space in more detail, the intensity ratio solution computed in Fig. 20a for sodium was expanded in Fig. 20b over a broad range of temperature and field strength values (matching the above limits, but with $= 0.06$). Contours representing the experimental mean and standard deviation are shown, identifying a locus of temperature and field strength values that provide high-quality fits. This demonstrates that the enhancement for sodium is consistent with relatively weak microwave fields (<30 Td), provided the plume temperature is significantly lower than equilibrium temperature ($_{0} \ll 3000$). This is also consistent with the intense enhancement observed during the cool post-combustion time period shown in Figure 20, where a large reduction in thermal energy, $_{0}$, in Eqn. 9 can diminish , a change consistent with a shift to a higher energy (lower wavelength) transition.

While the proposed WMIP model appears consistent with experiments, it is not free of limitations. Most immediate to the wavelength sensitivity analysis, the evaluation of rate coefficients may be incomplete, as: (1) the wavelength dependence of alkali cross-sections are only crudely approximated; and (2) the two-term Boltzmann approximation may carry significant error for high-pressure molecular discharges. These limitations require further review. For the model, the lack of a well-prescribed temperature distribution, field strength, and alkali mole-fraction prevents rigorous validation, and the homogenous plume assumption must be tested against spatially-resolved temperature and radiance data. These limitations reinforce the need for further investigation with more capable numerical methods and improved diagnostics.

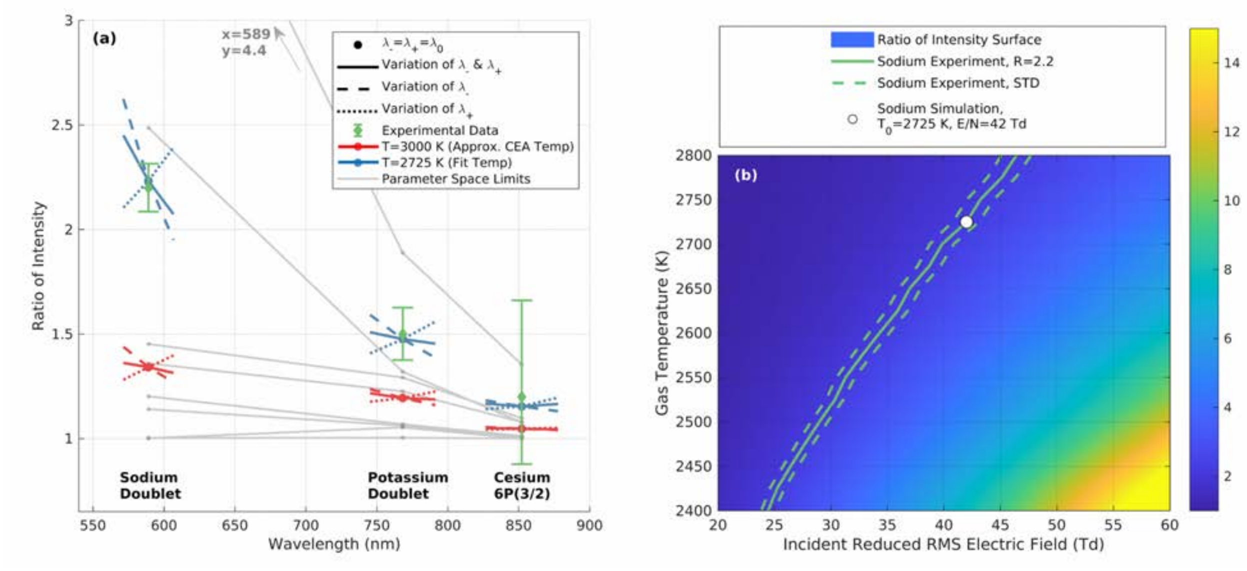

Figure 20. (a) Model results for ratio of radiance with and without applied microwave is shown (Eqn. 14). A best fit solution was found for incident RMS field strength of 42 Td, alkali mole fraction of 6 vol.%, and temperature of 2725 K (blue). A high temperature case representative of CEA equilibrium conditions is also shown (red). Each case is plotted at line center λ_{21}*, with perturbations in wavelength showing the local sensitivity from several terms in Eqn. 3-15 producing positive change with wavelength* (λ_+) *, the single term producing negative change (* λ_-*), and total change (*λ_- λ_+ *). Experimental frequency-integrated irradiance ratios are also plotted, with error bars representing the standard deviation of three trials (green). Lastly, a set of eight simulations are shown covering the practical limits across the three major parameters (gray). (b) The enhancement ratio in (a) is computed for sodium over a range of temperature and field strength values. Contours representing the corresponding experimental value plus/minus one standard deviation are overlaid with simulations, along with the fitted temperature and field strength.*

5.1.2.5. Microwave Effects on Luminosity and Chromaticity

Emission from the Mg/NaNO$_3$/epoxy time-series spectra were plotted on chromaticity diagrams (Fig. 21) for three conditions: baseline energetic material combustion without microwave illumination, energetic material combustion with microwave illumination, and microwave illumination of post-combustion products. Fig. 21 shows high color purity for all three conditions. Emission for all three conditions is dominated by the 589 nm Na I emission (3p-3s transition, Fig. 21) and Fig. 21 furthers shows that all three conditions produce light emission of similar dominant wavelength. With respect to the subtle trends in emission, with microwave illumination, emission becomes more monochromatic and follows the 589 nm emission line. This effect is particularly evident in emission post-extinguishment. Color purity of the post-combustion plasma light emission is found to vary more than either of the other two conditions, which may be due to the low intensity of post-combustion emission, and amplification of noise during calculation of the dominant color (spectrometer integration time during experiments was optimized for sampling during the combustion period rather than the post-combustion period). The chromaticity analysis of the Mg/NaNO$_3$/epoxy formulation suggests overall that emission color of the energetic material produced from microwave enhancement is similar to that of the baseline energetic material emission. The potassium and cesium-based systems were not analyzed because their primary emission bands are outside the visible spectrum.

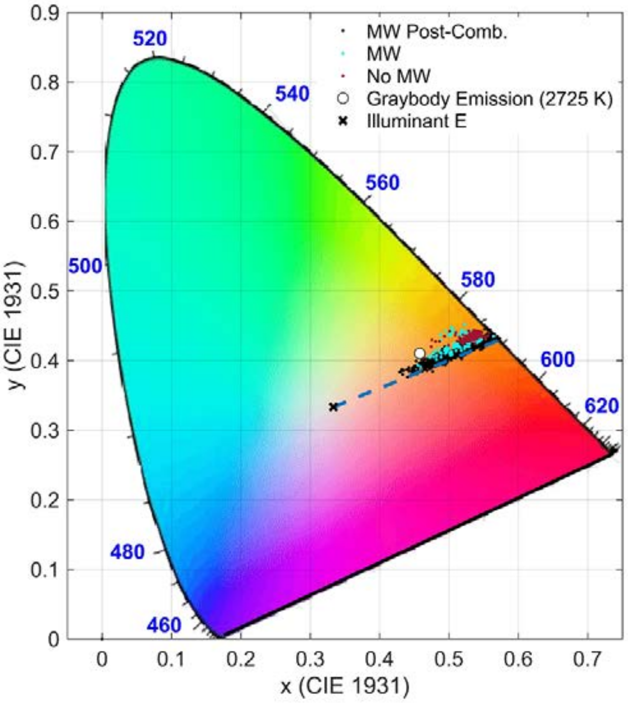

Figure 21. CIE 1931 chromaticity diagram showing time-resolved color and purity of emission from Mg/NaNO3/epoxy energetic materials (1) without microwave illumination, (2) with microwave illumination, and (3) emission acquired from microwave illumination of combustion products post-extinguishment. Graybody emission at 2725 K and the Illuminant E point is indicated on the diagram. The dash line represents dominant wavelength of 589.2 nm of varying color purity.

5.1.2.6. IR Emission Enhancement

Measures of time-averaged IR spectral irradiance of each alkali-nitrate formulation (Fig. 22) showed that emission enhancement resulting from microwave illumination of the three formulations extended beyond the visible spectrum and into the IR. Specifically, enhancement of emission from Na I (0.947 µm), K I (1.048, 1.177, and 1.415 µm), and Cs I (1.358, 1.469, 3.010, 3.490, and 3.614 µm) electronic transitions were observed. Additionally, slight emission enhancement of the CO_2 (~4.2 to 4.8 µm) and H_2O (~2.5 to 3.0 µm) IR emission bands were observed for all formulations.

Similar to the visible enhancement results (Fig. 19), little gray body continuum emission enhancement was observed in the near infrared as a result of microwave illumination. This is in contrast to the high concentration of equilibrium-predicted condensed-phase products within the flame (Table 4, 31.2 to 35.2 mol.%) and the high equilibrium flame temperatures of compositions (2943 to 3088 K). In similar studies involving microwave illumination of aluminized AP composite propellants containing NaNO3 dopant [29], continuum emission enhancement of alumina products from aluminum agglomerate diffusion flames was observed as a result of the exponentially temperature-dependent increase in aluminum oxide microwave absorptivity (i.e. microwave loss tangent) that has been observed by others [30]. The high temperature increase in microwave absorptivity, referred to as 'thermal runaway' in microwave sintering literature, is observed in many ceramics as a result of a shift in heating mechanism from dielectric at low temperatures to eddy current heating at high temperature due to increased charge mobility at higher temperatures [121]. In the aforementioned propellant study, aluminum oxide exists in liquid phase, where its acts as an ionic conductor due to enhanced charge mobility [122]. Consequently, application of an electric field to liquid aluminum oxide can result in more efficient energy absorption and conversion to heat. Conversely for the MgO products within energetic material flames of this study, the MgO remains in solid phase due adiabatic flame temperatures that are lower than the melting point of MgO. Dielectric absorption of solid MgO products may be inefficient at energetic material flame temperatures, as little continuum emission enhancement is observed.

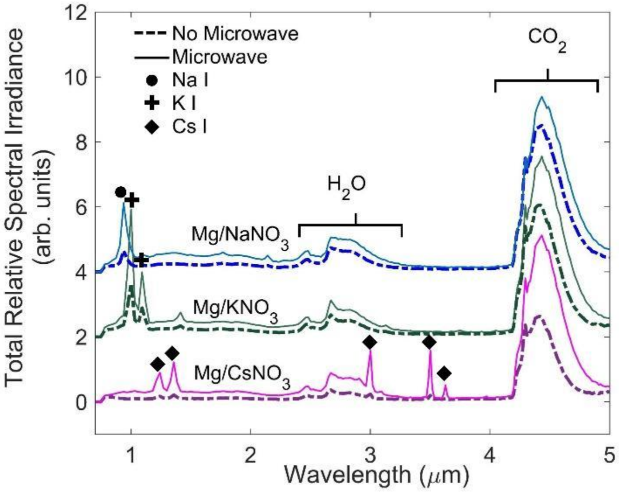

Figure 22. Time-integrated, infrared total spectral irradiance of each Mg/alkali nitrate/epoxy energetic material with and without microwave illumination. Species of significant electronic atomic and molecular emission enhancements observed are noted. Irradiance values for each formulation are offset for presentation purposes.

5.1.3. Two-photon Planar, Laser-induced Fluorescence (PLIF) of Microwave-supported Plasmas In Sodium-doped Flames

The subsequent sections present results for two-photon excitation of atomic sodium in gas-phase flames and multiphase propellant flames. First, a comparison of fluorescence emission at 818 between the 3s–4d excitation and 3s–3d excitation was carried out to assess the potential signal-to-noise and fluence dependence in gas-phase flames. Ionization excitation spectra are then presented, and a rate-equation model is compared to the fluence dependence of two-photon excited fluorescence (3d–3p), amplified spontaneous emission, and ionization specifically for the 3s–3d excitation. This scheme is then demonstrated for sodium distribution mapping at the near-surface of a composite solid-propellant flame.

5.1.4. Comparison Between Two-photon Excitation Schemes

A direct comparison of two-photon 578 and 685 excitation was carried out using the sodium-doped premixed flat flame burner to directly compare fluorescence emission from the same states (3d–3p) at 818 . The emission at 818 was compared for both two-photon excitation schemes, and is presented in Figure 23. For the two-photon 578 excitation, the detected fluorescence does not originate directly from the excited 4d state. Instead, the 818 emission originates from the 3d state and relies on collisional or non-radiative energy transfer for excitation following the two-photon pumping to the 4d state. This excitation, which was previously considered by Weiland et al. [51], may be non-optimal due the indirect excitation pathway. As an alternative, two-photon excitation at 685 was evaluated—leading to a directly excited fluorescence transition at 818 . The fluence dependence of the 818 fluorescence is shown in Figure 23 for both two-photon excitation schemes. The symbols and error bars show the mean integrated signal and variance, respectively, for 500 laser shots. The fluorescence resulting from 685 excitation shows an order of magnitude increase in signal over the 578 excitation, which is a result of the direct fluorescence emission from 3d–3p state. For two-photon excited laser-induced fluorescence an ^{2} dependence is often expected, but sodium exhibits significant deviations even at low excitation fluence. As reported by Weiland et al., fluorescence fluence variation yielded power-laws of 1.0 for 3s–4d excitation. The results shown in Figure 23 result in power-law fits of $= 0.38$ for 685 excitation (3s–3d) and $= 0.88$ for 578 excitation (3s–4d) [51]. The significant deviation from quadratic dependence can be attributed to loss mechanisms of ASE and ionization, which will be discussed in the subsequent sections.

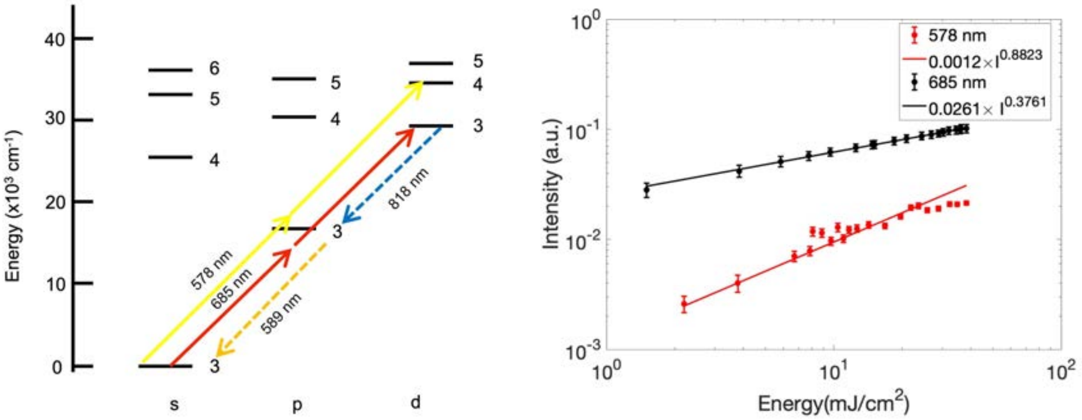

Figure 23. Left: Sodium energy level diagram depicting two-photon excitation strategies from the ground state (3s–3d and 3s–4d), indicated with solid lines. Possible detection wavelengths directly or indirectly populated are shown as dashed lines (4d–3p and 3p–3s). Right: Lasr fluence-dependence of the fluorescence signal at 818 for two-photon excitation at 685 and 578 in the premixed sodium-seeded flame.

5.1.5. Resonance-enhanced Multiphoton Ionization In Sodium

To examine loss mechanisms detrimental to the fluorescence yield, both ionization and amplified spontaneous emission occurring during the multi-photon excitation process were evaluated. Laser-induced ionization was measured using the ionization probe as detailed in Figure 24 and collected using a boxcar integrator. The ionization excitation spectrum near the two-photon 3s–4d transition (578) is shown in Figure 24 for fluences of 1.4 and 16.7 . Symbols indicate the average total ion probe signal averaged over 500 laser shots. For the low fluence case (red symbols), the laser-induced ionization is absent when tuning far from the two-photon resonance, while significant REMPI signal is collected on-resonance. For the high fluence case (black symbols), the off-resonant signal is significant, made evident by the increased width of the excitation line and the non-zero baseline at a signal of 5 . At the peak, the signal increases by a factor of ~4 over the off-resonant contribution. In comparison, the signal ratio on- and off-resonance for the low fluence condition is ~60. In both cases, the on-resonance ionization is readily measurable and likely represents a significant loss mechanism. This will be discussed further in the next section using a rate-equation model.

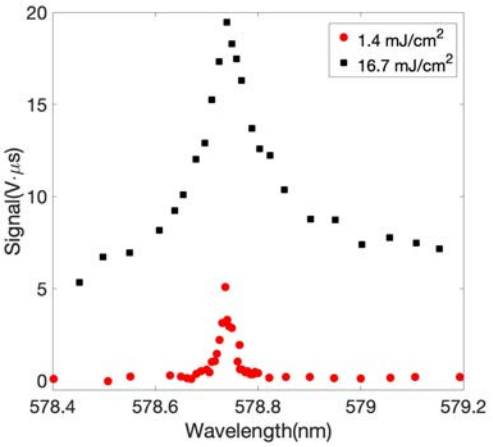

Figure 24. Multi-photon ionization spectra for the 3s–4d (578) two-photon transition for two different fluences: 1.4 (red) and 16.7 (black).

5.1.6. Two-photon Rate Equation Model

To further evaluate the relationship between laser energy, fluorescence, ionization, and amplified spontaneous emission, 685 excitation was monitored in the sodium-doped flat flame burner and compared with a one-dimensional model capturing ASE and ionization effects. For these comparisons, the fluence was varied while monitoring fluorescence (collected with a photomultiplier tube), ionization level (detected by the ion probe) and amplified spontaneous emission (collected with a photodiode) using a boxcar integrator as previously described. Due to the limited number of available channels, each of the three signals was collected simultaneously in pairs while monitoring the laser energy on a shot-to-shot basis.

In order to assess the losses in the fluorescence signal due of multi-photon ionization, fluorescence, and ASE processes, the following section presents a rate-equation model capturing these effects. Rate equation models have been used to represent atomic systems, as previously described by Amorim et al. [123,124] for atomic oxygen and Zhao et al. [125] for atomic hydrogen. These models captured the growth of ASE and the fluence dependence of the two-photon fluorescence signal.

For atomic sodium, a four-level system was considered with number densities corresponding to the following: ${}_1$ to Na(3s), ${}_2$ to Na(3p), ${}_3$ to Na(3d), and to . The processes incorporated in the rate equation model include two-photon excitation, ionization from the excited 3d state, and emission and quenching from the 3d state. Atoms in the excited state can either absorb another photon resulting in ionization, spontaneously emit a photon to proceed back to the intermediate 3p state, undergo collisional quenching, or participate in amplified spontaneous emission for the 3d–3p transition. The stimulated emission wave was considered for a given laser focusing geometry and incorporated using a one-dimensional numerical model and a rate equation system similar to that implemented by Zhao et al. [125] and Amorim et al. [123,124] for atomic oxygen. The rate equations involving the four population number densities were:

$$\frac{{}_1}{} = -\left({}_1 - \frac{{}_1}{{}_3}\, {}_3 \right)\frac{\alpha_{1,3}\phi^2}{h\nu} + {}_2\left({}_{2,1} + {}_{2,1}\right) + {}_3\, {}_{3,1}, \tag{19}$$

$$\frac{{}_2}{} = {}_3\left({}_{3,2} + {}_{3,2}\right) - {}_2\left({}_{2,1} + {}_{2,1}\right) + \frac{{}_{3,2}}{}\Gamma\left({}_3 - \frac{{}_3}{{}_2}\, {}_2\right), \tag{20}$$

$$\frac{{}_3}{} = \left({}_1 - \frac{{}_1}{{}_3}\, {}_3 \right)\frac{\alpha_{1,3}\phi_1^2}{h\nu} - {}_3\left(\frac{\sigma\ \phi}{h\nu} + {}_{3,2} + {}_{3,1} + {}_{3,2}\right) - \frac{{}_{3,2}}{}\Gamma\left({}_3 - \frac{{}_3}{{}_2}\, {}_2\right), \tag{21}$$

and

$$\frac{}{} = {}_3\frac{\sigma\ \phi}{h\nu}. \tag{22}$$

Here, and h are the speed of light and Planck's constant, respectively; ϕ is the excitation laser pulse irradiance, and ν is the frequency of the pump laser. The degeneracy for each level is , the Einstein spontaneous emission coefficient from level to is and are collisional quenching rates estimated from Fourkas et al. [126]. The two-photon absorption cross section is $\alpha_{1,3}$ and the photoionization cross section from the 3d state is σ . The rate of loss due to ASE incorporates the stimulated emission rate , the linewidth of the stimulated emission ($\Delta\nu$) and Γ is the overlap integral of absorption transition and ASE radiation line shape profile. We consider $\Gamma = 0.5$ as constant [127] and $\Delta\nu \ = 1$ [124]. The stimulated emission coefficient is related to the spontaneous emission rate through ${}_{3,2} = {}_{3,2}\ {}^3/8\pi h\nu^3$.

In order to account for the traveling gain of the stimulated emission wave, two transport equations are included for the stimulated emission in the forward and backward directions and were solved simultaneously with the rate equations. The forward and backward stimulated emission transport equations are given by

$$\frac{}{} = \left(\frac{{}_{3,2}}{}\Gamma\left({}_3 - \frac{{}_3}{{}_2}\, {}_2\right) + {}_3\, {}_{3,2}\frac{\Delta\Omega}{4\pi}\right)h\nu \tag{23}$$

and

$$\frac{}{} = \left(\frac{_{3,2}}{}\Gamma\left(_{3} - \frac{_{3}}{_{2}}\,_{2}\right) + \,_{3}\,_{3,2}\frac{\Delta\Omega}{4\pi}\right)h\nu. \tag{24}$$

For each element in the domain of interaction, the solid angle for the forward (Ω) and backward (Ω) stimulated emission is written in terms of the height of the beam focusing ( ), the approximate beam thickness ( ), and the total length of the region ( ):

$$\Delta\Omega \;=\; ^{-1}\left(\frac{}{}\right)\;\left(\;^{-1}\left(\frac{}{}\right)\right) \tag{25}$$

and

$$\Delta\Omega \;=\; ^{-1}\left(\frac{}{}\right)\;\left(\;^{-1}\left(\frac{}{}\right)\right). \tag{26}$$

The two-photon excitation and ionization cross sections for 685- excitation were unavailable in literature. In order to estimate these cross sections, the approach of Zhang et al. [57,128] was followed, where time-dependent perturbation theory was used to model a resonance-enhanced multiphoton ionization (REMPI) process involving 3s–5s excitation and subsequent ionization of sodium. This model showed good agreement with microwave radar REMPI measurements of ionization [128], and the same procedure is used here to calculate the 3s–3d two-photon excitation cross section. To summarize the approach, the two-photon cross section can be expressed in terms of a two-photon process by considering excitation through an intermediate virtual state [57,128–130]. The two-photon excitation cross section is given by

$$\alpha_{1,3} = (2\pi)(2\pi\alpha)^2(2\pi\nu\;)^2\left|\sum\frac{}{\sqrt{\left(2\pi(\nu\;\;-\nu\;)\right)^2+\gamma^2\;/4}}\right|^2. \tag{27}$$

Here, and are the ground and final states and are the the intermediate states. The frequency difference ν corresponds to the energy difference between the ground and intermediate state, $\nu \;=\; \;-\;\;)/h$. In the expression, α is the fine-structure constant ($\approx 1/137.036$), ν is the frequency of the exciting incident laser, and γ is the natural linewidth of the intermediate state given by the inverse of the spontaneous emission rate. In (27), we sum over 10 intermediate states given by allowable transitions from the ground state (3s–3p, 3s–4p, etc.).

The dipole transition matrix element for two states and is related to the Einstein spontaneous emission rate by [129,131]:

$$\left|\langle\alpha\;\;\;\;{}'\;{}'\;{}'\rangle\right|^2 = (\;{}'+1)\left(\;{}'\;-\;\;{}'\right)^2\times\frac{{}^{2}_{0}}{0.66702\sigma^2}. \tag{28}$$

Here, each state is denoted by the orbital angular momentum (and ′), the spin angular momentum (and ′), the total angular momentum (and ′) and the -component of the total angular momentum (and ′). is the energy gap between two states in units of Rydberg, σ is the transition energy in , and $_0$ is the Bohr radius (5.2918×10^{-11}).

The ionization cross section from the excited state of an alkali atom can be approximated as [128]

$$\sigma \quad = \frac{8\times10^{-22}}{(\quad)^{1/2}(h\nu \quad)^{3}}, \tag{29}$$

where is the net charge on the ion, is the ionization potential for the atom in the excited state, is the Rydberg constant (13.60569) and $h\nu$ is the photon energy.

The state data and rate constants incorporated in the rate equation model are summarized in Table 6, based on relevant selection rules and standard reference data [132]. The calculated ionization cross section from the 3d state and the two-photon cross section for 3s–3d excitation are given.

Table 6. Rate constants used in the 1D model including ionization and stimulated emission loss processes.

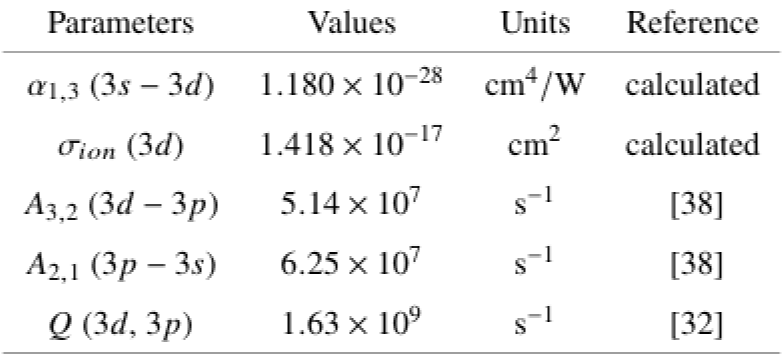

Parameters	Values	Units	Reference
$\alpha_{1,3}$ $(3s - 3d)$	1.180×10^{-28}	cm^4/W	calculated
σ_{ion} $(3d)$	1.418×10^{-17}	cm^2	calculated
$A_{3,2}$ $(3d - 3p)$	5.14×10^{7}	s^{-1}	[38]
$A_{2,1}$ $(3p - 3s)$	6.25×10^{7}	s^{-1}	[38]
Q $(3d, 3p)$	1.63×10^{9}	s^{-1}	[32]

The model was evaluated in comparison with the sodium-seeded gas phase flame experiments, where the number density of ground state Na atoms was assumed to be 2.0×10^{15} as estimated from equilibrium calculations. The experimental focusing was incorporated using a one-dimensional domain with a length of 60 mm and diameter of 0.9 mm for calculation of the solid angle, Ω, in the stimulated emission transport equations. No other free parameters exist in the model, and these experimental inputs were estimated from the experiment for the subsequent comparison of model and experiment. The system of equations was integrated using a hyperbolic partial differential equation solver [133]. Using the coupled equations, the time-dependent fluorescence emission from the domain and the total ASE intensity are given by

$$\propto \quad _{3} \quad _{3,2} \tag{30}$$

and

$$= \quad + \quad . \tag{31}$$

A comparison of the measured and calculated fluorescence, ASE, and ionization are shown in Figure 25 for a range of laser fluences. The experimental measurements were not calibrated for absolute photon or ion yield, so the modeled results were scaled for comparison to the experimental data. The model values (ion number density, total integrated fluorescence intensity of the 3d–3p transition, and integrated stimulated emission) are normalized to the experimental values at a fluence of 90 . For each experimental measurement, the symbols indicate the mean value and the error bars indicate the variance across 2000 laser shots.

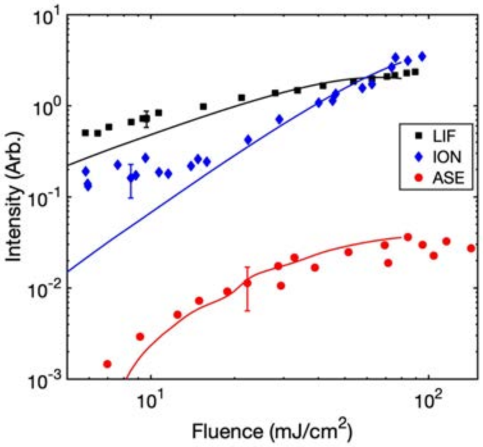

Figure 25. Comparison between 1D model and experimental measurements of two-photon excited LIF, ionization, and stimulated emission. Points indicate mean values over 2000 laser shots from the experimental measurements and lines indicate the model result, which has been normalized to experimental values at 90 for comparison. Error bars indicate the typical variance for each series.

The model and experiment show similar trends across the range of fluences considered. Fitting a power law for the experimental and model data for fluorescence showed powers of 0.88 and 1.35 with the fluence, respectively. The rapid increase of ASE at low fluence and the trend of increasing ionization are captured by the model. For the ionization yield, there is significant deviation between experimental and modeled results at low fluence which is attributed to the low signal-to-noise of the ion probe measurement. It should be noted that the experimental measurement of ionization should not be interpreted quantitatively, as the significant effects of ion transport and recombination at atmospheric pressures limit quantitative interpretation. However, the rate equation model captures the overall variation of the desired fluorescence signal and the parasitic loss processes of ionization and ASE. These experimental and rate equation model results reveal potential limitations for quantitative imaging using two-photon Na LIF.

The fluorescence signal fluence dependence departs significantly from a $= 2$ power law, even at very low fluence. This behavior is dominated by single-photon ionization of the 3d state of sodium. In addition, the saturation of the two-photon transition is readily achieved (at a fluence of 44) when other losses are not present. The rate equation model showed losses due to ASE were dominated by both ionization losses and saturation of the two-photon transition.

The modeled results highlight several significant challenges for quantitative measurement of sodium concentration by two-photon excited fluorescence. However, two-photon excitation has the advantage of avoiding resonant fluorescence emission of particle scattering and high concentration fluorescence trapping. In addition, the novel 3s–3d excitation allows for detection from directly-excited 3d state which has higher fluorescence yield than 3s–4d excitation. This scheme has the potential for improved signal-to-noise ratio detection of fluorescence in multiphase combustion systems due to improvement of fluorescence yield, which will be discussed in the next section.

5.1.7. Two-photon LIF In Solid Propellant Flames

Sodium-doped composite propellant flames, which have recently been studied for active modulation of the burning rate with microwave fields [29], present multiple challenges for imaging. The propellant flame environment is highly luminous due to electronic emission from atomic and molecular species and continuum emission from condensed phase products, contains numerous scattering particles and drops, and has high atomic vapor concentrations. To minimize signal trapping, avoid scattering interferences, and avoid strong emission from the lowest-lying state of atomic sodium, the two-photon excitation at 685 (3s–3d) was employed with detection of fluorescence at 818 (3d–3p).

As detailed in the experimental description, a laser sheet was formed above the burning composite solid propellant strand to examine the two-dimensional structure of atomic sodium at the propellant burning surface. In these propellant formulations, the distribution of atomic sodium vapor controls the regions of interaction with electric fields due to thermal ionization of Na in the high-temperature flame. The laser sheet was propagated from left to right, so for certain geometries, only the nearside sodium distribution was visible in the fluorescence images.

Two representative planar two-photon excited fluorescence images are shown in Figure 26. The upper panel (a) shows the result for two-photon excitation at 578 (3s–4d) and detection at 818 –the scheme previously investigated by Weiland et al. [51]. Panel (b) shows the result for the directly-excited spontaneous emission at 818 from the 3d state for two-photon excitation at 685 (3s–3d). As in the gas phase flame results, the overall signal yield at 818 is significantly improved for excitation at 685 . Both images are shown on a logarithmic color scale to better display features across the entire dynamic range. Figure 26(a) shows the result for 578 excitation at a fluence of 52 . A profile along the white line was chosen to highlight a region with little particle interference. The signal-to-noise ratio (SNR), defined as the mean signal level in the highlighted box divided by the standard deviation of the signal over the same area in the image (= μ/σ) was approximately 10. In Figure 27(b) the sodium distribution above the propellant burning surface is shown using two-photon excitation at 685 with a fluence of 55 . The image quality is superior, with a SNR of 112 within the highlighted box. Again, the signal along a vertical line was plotted on a linear-scale in the right panel. Small fluctuations in signal visible across the line plot are due to particle interference. This scheme (3s–3d excitation at 685 ; detection of 3d–3p at 818) offers the possibility of mapping atomic sodium concentration in high density, multiphase environments such as aluminized composite propellant flames.

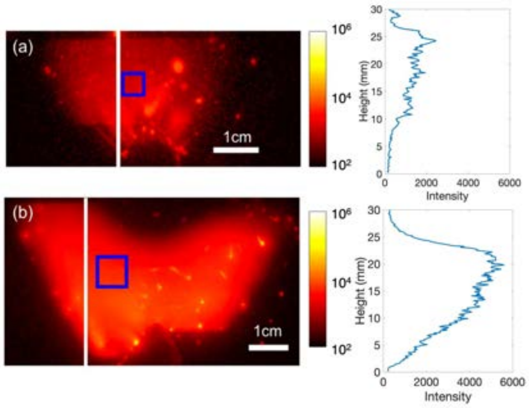

Figure 26. Comparison of 578- (3s–4d) and 685- (3s–3d) excited two-photon planar laser-induced fluorescence of doped aluminized composite propellant flame. Detection for both fluorescence emission wavelengths was at 818 nm, with (a) 578 excitation at a fluence of 52 and (b) 685 excitation at a fluence of 55 . Both images show a logarithimic color scale and fluorescence intensity line profiles are shown to the right.

To illustrate the utility of mapping the Na distribution in the multiphase combustion environment, a series of high-magnification two-photon excited Na LIF images are shown in Figure 27(a). With this magnification, in comparison with Figure 26, significant spatial variation in the Na vapor distribution is evident immediately above the burning surface (the dark region). This local variation is attributed to the formulation of the composite propellant. In manufacture of the propellant, (<75), oxidizer (bi-modal AP 90-200), and metal particles (Al, 30) are mixed in powder form and then cast. This results in crystals dispersed through the composite propellant. The two-photon LIF imaging indicates local decomposition of the leads to local high concentration pockets of Na formed from decomposition at the burning surface. Further downstream, the Na distribution viewed via two-photon excited LIF is more uniform, as the Na vapor advects and mixes with other evolved products from the burning surface.

For qualitative comparison with the two-photon fluorescence imaging near the burning surface, a set of representative emission images are shown in Figure 27(b) from plasma formation in propellant during microwave illumination of the flame using the procedure of Barkley et al. [29]. During this experiment, microwave field application resulted in plasma formation and increased burning rates of the composite propellant. The emission images show regions of plasma kernel formation above the burning surface, indicated by locally bright, filamentary regions which extend towards the burning surface. In atmospheric-pressure flames, this plasma formation is restricted to regions of high local free electron concentration and low density (high temperature). In comparing these filamentary structures to the two-photon LIF from sodium near the burning surface, it appears that plasma initiation and energy deposition to the flame is spatially non-uniform and controlled by local variations in the atomic sodium concentration. The two-photon excited fluorescence scheme allows for near-surface qualitative mapping of the sodium distribution in the multiphase propellant flame. The confirmation of high local Na concentration regions near the burning surface via this two-photon excitation scheme (Figure

27(a)) provides a mechanistic pathway for near-surface energy deposition in the propellant flame structure–in regions of both high local temperature and local Na concentration.

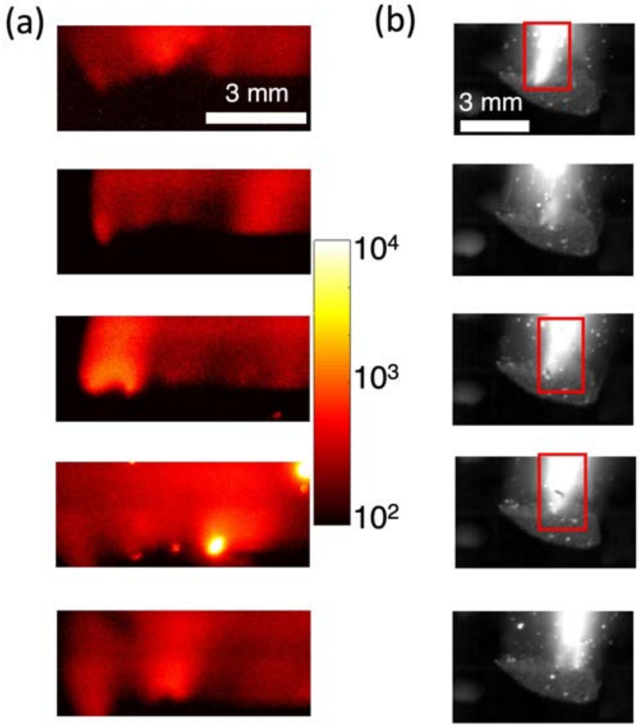

Figure 27. Images of the sodium distribution in -doped, aluminized composite propellant flames (a) near the burning surface with 685 (3s–3d) two-photon planar laser-induced fluorescence. In panel (b), typical filamentary structures formed during the application of the microwave field are shown, observed here by increased sodium emission intensity at 589 . The plasma filament formation is highlighted with the boxes in (b).

The potential signal loss due to ionization and ASE should be considered in the evaluation of Na LIF results from the propellant flame. Although the ionization probe could not be used in the multiphase propellant flame, a photodiode was used to evaluate ASE at 818 in the forward direction. The photodiode was placed after the laser sheet and filtered with a dichroic beamsplitter and bandpass filter at 818 , as described for the gas-phase flame experiments. For the increased sodium concentration in the propellant flame, ASE was observed even at fluences which did not exhibit any detectable gas-phase flame ASE. The presence of ASE on such strong oscillator strength transitions (alkali atoms) is likely unavoidable at these very high atomic concentrations. No signal depletion in the fluorescence images was evident in the test burner (at a lower concentration), but these effects have not been quantified.

The images presented in Figs. 26-27 indicate the sodium distribution in propellant flames with alkali-dopant concentration of 3.5% wt.. From these results, variations in the local sodium concentration are evident, but the quantitative interpretation is challenging. Although the rate equation modeling and gas-phase flame studies showed power laws of $= 0.8 - 1.3$, depending on fluence, additional data were taken with varying sodium concentration in gas-phase flame (6.25 and 50) to evaluate the ability for relative concentration imaging. In these flames, the mole fractions of 2.1 ppm and 12.5 ppm corresponded to a mean flame signal ratio of

1 to 4.32. This suggests that with careful calibration, it may be possible to use the presented two-photon excitation scheme for relative quantitative measurements of the sodium concentration. However, the dynamic propellant flame environment limited the quantitative concentration determination. Nevertheless, the variation in local concentration in these flames is clearly evident for the novel two-photon excitation and detection scheme presented (3s-3d excitation, with detection for the 3p-3d fluorescence).

5.2. Material Techniques For Microwave Interaction With The Energetic Material Condensed Phase

5.2.1. Microwave Ignitable, GO-wrapped Thermites With Thermally Switchable Microwave Ignitability

5.2.1.1. Microscopic Characterization

The synthesis of GO and rGO-wrapped thermites and their unique, switchable microwave effects are described graphically in Figure 28. The morphologies of the r-GO/GO thermite composites were examined by SEM using compositional backscatter detection. As seen in Figure 28a, the 30 wt.% r-GO thermite composite completely encapsulates the thermite nanoparticles. Clusters of r-GO wrapped thermite are very large, on the order of ~10 to ~100 μm (not shown) and are comprised of r-GO-wrapped clusters of n-Al/n-Fe_2O_3. Figure 28b-c shows the morphology of thermites with selectively encapsulated n-Al (Figure 28b) or n-Fe_2O_3 (Figure 28c). In these micrographs, particles of either n-Al or n-Fe_2O_3 are observed to be excluded from the r-GO wrapping. Lastly, Figure 28d shows GO wrapped thermite composites, where most of the thermite appears to be surrounded by the GO sheets. However, the boxed region in this micrograph indicates possible presence of high atomic weight thermite features that are not coated. Considering the use of a two-step sonication and wash process used to fabricate GO wrapped thermite composites and the presence of small n-Fe_2O_3 particles surrounding the n-Al particles, we expect the identified region may contain particles having incomplete GO coating.

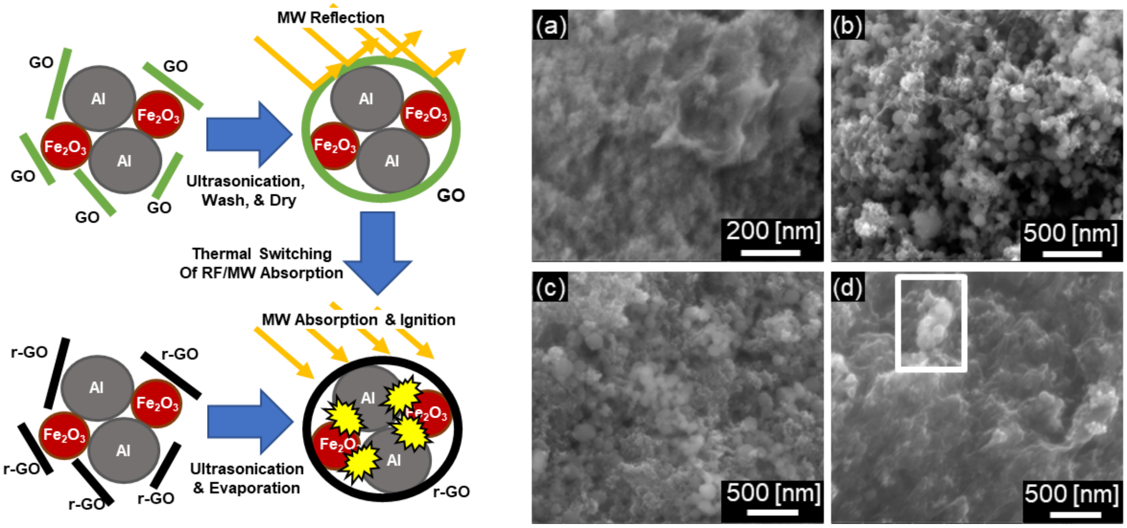

Figure 28. Left: Illustration of synthesis of r-GO or GO-wrapped n-Al/n-Fe2O3 thermites with thermally switchable microwave ignitability. Through thermal treatment, GO is reduced to form r-GO, which enhances the microwave absorptivity of the wrapped thermite and facilitates ignition. Right: SEM images of (a) r-GO-wrapped n-Al/n-Fe2O3 thermite (30 wt.% r-GO) (b) r-GO-wrapped n-Al with n-Fe2O3 (c) r-GO-wrapped n-Fe2O3 with n-Al and (d) GO-wrapped thermite with a box to indicate incomplete GO coating.

5.2.1.2. Thermal Characterization

DSC/TGA histories for n-Al/n-Fe_2O_3 thermites, GO, and GO-wrapped thermites heated in argon at 10 °C min^{-1} are shown in Figures 29a-b. Both GO and GO-wrapped thermites exhibit an exotherm at 212 °C, which is assigned to GO disproportionation and is reported by others [134,135]. At this temperature, oxygenated functional groups of GO are destroyed in redox reactions corresponding to both heat release and a mass loss of 20% (GO) or 10% (GO-wrapped thermite). This is further confirmed by mass spectroscopy of the DSC/TGA purge exhaust gas flow, which shows simultaneous rise in CO, CO_2, and H_2O concentration (Figure 29c). At temperatures above disproportionation, neat GO displays no remarkable features, but both the thermite and the GO-wrapped thermite exhibit a series of thermal features that are hypothesized to be a result of phase changes of Al and Fe_2O_3 and/or oxidation of aluminum by Fe_2O_3.

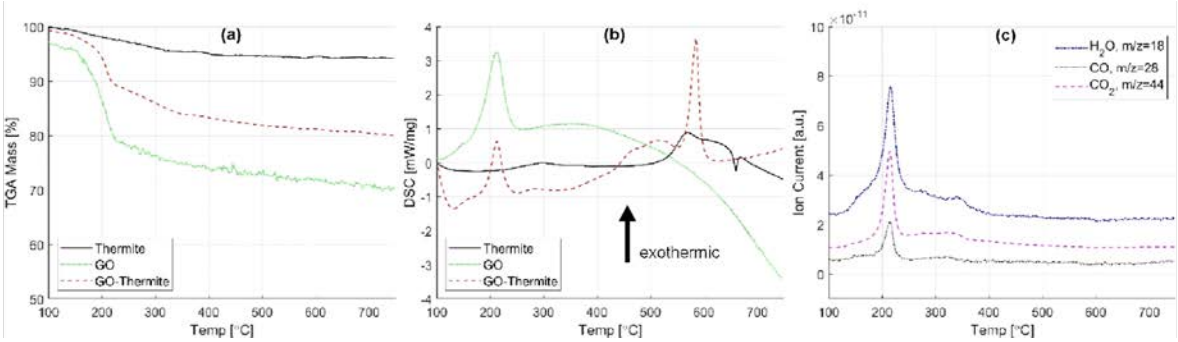

Figure 29. TGA (a) and DSC (b) of n-Al/n-Fe2O3 thermite, GO, and GO-wrapped thermite (30 wt.% GO) with mass spectrometry of significant evolved products for GO-wrapped thermite (c).

Turning attention to the unwrapped thermite, a small, broad exothermic feature around 300 °C occurs, which is assigned to the crystallization of amorphous Fe_2O_3 to γ-Fe_2O_3 [136]. Though not observed here, a more ordered crystallization (γ-Fe_2O_3 to α-Fe_2O_3) has also been observed by others in Fe_2O_3 at 350 °C and continues until 450 °C to 550 °C [137]. The onset temperature and observed heat release of this phase change has been noted to vary significantly based on external conditions due to its weak activation energy. The next thermal feature of the unwrapped thermite onsets near 500 °C, where a broad exothermic feature corresponds to the end of the α-Fe_2O_3 crystallization and the onset of crystallization of amorphous Al_2O_3 to γ-Al_2O_3 [138,139]. An exotherm near this temperature is frequently observed in thermites containing n-Al and is attributed to enhanced species transport at the Al/oxide interface caused by densification-induced cracking in the oxide shell during crystallization [140]. The thermite reaction then begins to occur according to,

$$ {}_{2}\;{}_{3} + \qquad {}_{2}\;{}_{3} + \qquad + \Delta h \ , \tag{1} $$

where reaction progress is limited by reactant transport [141], and continues until the remaining aluminum melts, exhibiting an endotherm at ~660 °C. The absence of sharp mass losses and evolved gases observed in TGA and MS data within this temperature range seems to further support the hypothesis of exothermic phase changes and a condensed phase thermite reaction.

The DSC/TGA traces of GO-wrapped thermites indicate that the presence of GO significantly enhances heat release of the stoichiometric thermite. The exothermic crystallization of Fe_2O_3 at 300 °C is observed. However, the GO-wrapped thermite displays a broad exothermic feature that begins at 350 °C and continues through ~565 °C, after which a sharp exotherm centered at 585 °C is observed. The sharp exothermic feature is related to the reaction of the GO carbon skeleton with an oxidizer [134,135,142], such as Fe_2O_3, and has been observed in Al/CuO nanothermites containing multilayer graphene as well [143]. It has also been suggested that GO could promote the dissociation of oxygen through the formation of small amounts of Al-C species, catalyzing the oxidation of aluminum [134,142]. The broad exothermic feature appears very similar to the one observed in the unwrapped thermite but with a much lower temperature onset (~100 °C lower). While other studies have also found an enhancement of the thermite reaction at ~550 °C due to the addition of graphene, this is the first evidence, to the authors knowledge, of a reduction in the onset temperature of the thermite reaction due to the presence of graphene. A similar effect has been observed in Al/CuO nanothermites containing multilayer graphene platelets and was hypothesized to be a result of enhanced thermal conductivity caused by multilayer graphene inclusion, which increases the rate of heat diffusion between particles [141,143]. In the present study, for the case of DSC/TGA of GO-wrapped Al/Fe_2O_3 nanothermites, the authors believe it is plausible that the presence of GO wrapping helps trap evolved gas species (e.g. CO, H_2O, CO_2), improving oxidizer availability for aluminum oxidation and the thermite reaction. This hypothesis is supported by literature that describes GO and r-GO being used as impermeable layers in various gas and molecular filtering applications [144,145], though they are typically used in multiple layers to further decrease permeability. Regardless of mechanism, this enhancement of energy release and reduction in reaction temperature warrant additional investigation to determine both the degree of enhancement and the mechanisms responsible.

5.2.1.3. Ignition Delay of rGO Wrapped Thermites

Microwave ignition of all r-GO wrapped thermites and the baseline thermite (0 wt.% r-GO) was observed in the resonant cavity. Figure 30 shows typical image sequences of the microwave ignition process for both the baseline thermite and an r-GO wrapped thermite composite (30 wt.% r-GO). Ignition of the thermites appeared to be a result of localized hot spots, which can be seen in visible emission prior to bulk ignition (time of first light, t_{FL}). In the baseline thermite, the subsequent reaction generates heat and accelerates the redox cycle until full ignition of the thermite occurs at an average time of ~4.34 s during microwave exposure for three trials, which Figure 31 shows a typical ignition delay measurement of the baseline thermite. However, in 30 wt.% r-GO wrapped thermite composite formulations, microwave ignition is an order of magnitude faster than the baseline thermite (0.43 s) and flame spread occurs much faster than all other formulations once a hot spot is formed (Figure 30).

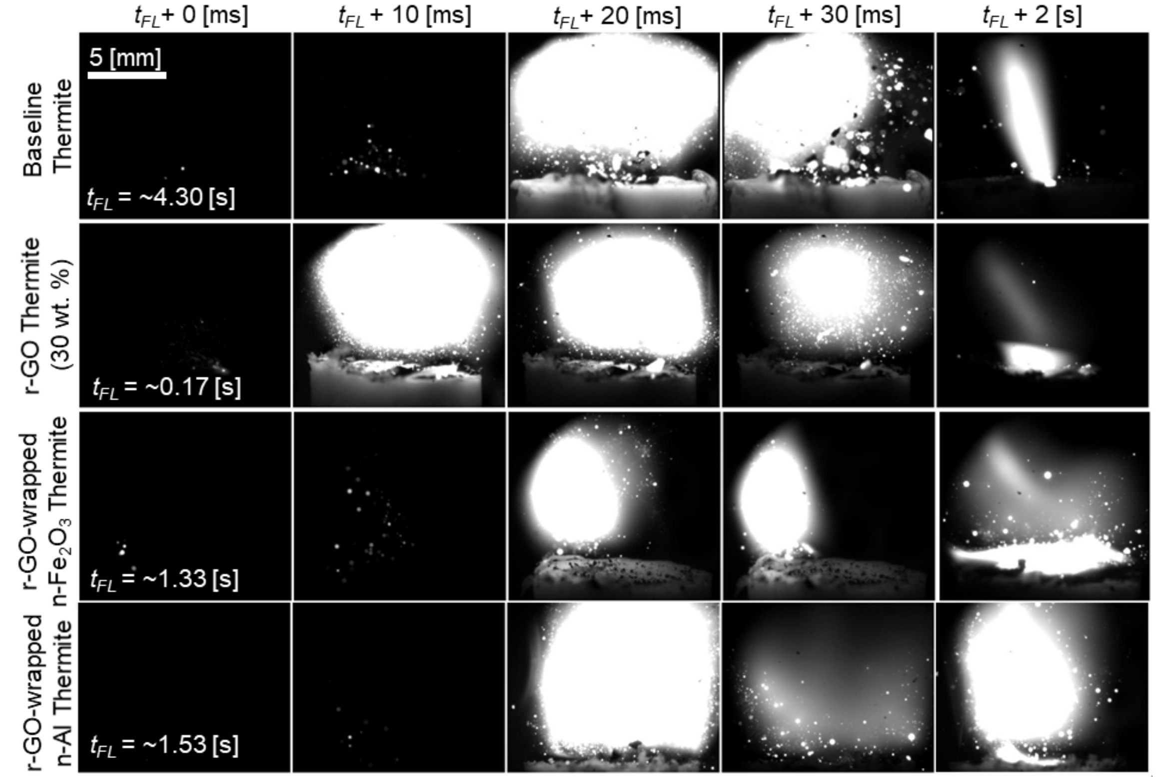

Figure 30. Image sequences of the microwave ignition (20 mg) of (a) pure n-Al/n-Fe2O3 thermite, (b) r-GO composite thermite (30 wt.% r-GO), (c) r-GO selectively wrapped n-Fe2O3 with n-Al (30 wt.% r-GO), and (d) r-GO selectively wrapped n-Al with n-Fe2O3 (30 wt.% r-GO) in a single-mode resonant microwave cavity. Time of first light (tFL) indicates the first frame of an image sequence where emission is observed in the camera.

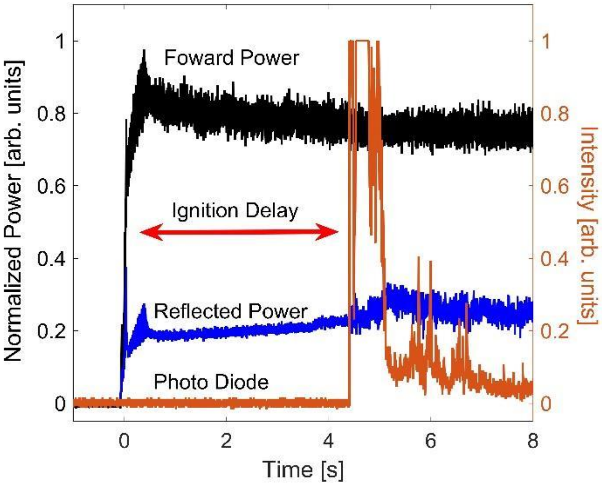

Figure 31. Typical time series from a test of microwave illumination of 0.2 g of baseline (no GO or r-GO wrapping) in the resonant microwave cavity. A time series of microwave forward and reflected power is shown with the photodiode signal to indicate the ignition delay.

For both thermites, bulk ignition is followed by high intensity emission which is maintained until the microwave field is shut off (~5 s after ignition). This high emission reaction region is diffuse (Figure 30) and characteristic of the electric field antinode shape [29,146] rather than a buoyancy driven energetic material flame. Based on prior studies of microwave enhancement of aluminized composite solid propellants [29] and energetic material flares [146], where emission enhancement of atomic metal and aluminum oxide condensed combustion products were observed, this region represent a plasma kernel formation in the gaseous thermite products. Based on prior studies, the high flame temperatures and electronically excited flame zone and products begin to couple with the electric field and microwave energy is deposited to the flame zone by 1) electronic and 2) dielectric loss mechanisms, which creates a weak plasma enhanced flame zone [29,146].

Average microwave ignition delays as a function of r-GO content are shown in Table 7**.** Baseline thermites (0 wt.% coating) exhibited an average microwave ignition delay of ~4.34 s. Ignition of the baseline thermite is expected to occur primarily due to electric field, as suggested in Meir et al. [65], Fe_2O_3 heating through an induction loss mechanism is lower than dielectric heating for large particles (orders of 100 μm) [147], and induction losses are expected to be negligible for the experimental conditions studied, as magnetic field amplitude is lowest at the electric field antinode for a transverse electric field mode. Moreover, nano-size particles have been shown to heat faster, due their higher specific surface area, which results in a greater volume of the particles that interact with the electric field [148].

By wrapping the thermite with r-GO, an increase in ignition delay is observed with higher amounts of r-GO, which is summarized in Table 7. With 30 wt.% r-GO, an average microwave ignition delay of ~0.43 s was observed. The shorter ignition delay in r-GO wrapped thermites may be a result of an increase in dielectric losses from interface polarization between r-GO and the thermite, and residual functional groups of r-GO, creating polarization centers [77]. Decreasing the amount of r-GO results in an increase of average ignition delay of 1.27 s for 20 wt.% r-GO and 1.37 s for 10 wt.% r-GO, as shown in Table 7. In a previous study by Xu. et al.

[78], measurement of microwave attenuation within paraffin containing r-GO wrapped Fe_2O_3 nanoparticles showed that dielectric losses increases with added weight percentage of r-GO.

Selectively choosing to encapsulate either n-Al or n-Fe_2O_3 with r-GO (30 wt.%) resulted in longer microwave ignition delays (1.53 s and 1.33 s, respectively) when compared to the 0.43 s ignition delay of the fully encapsulated thermite of the same composition (Table 7). Shown in Figure 30, after microwave ignition (greater than 2 s), thermites with selectively wrapped n-Al or n-Fe_2O_3 exhibited longer combustion times than either the baseline (0 wt.% r-GO) or the r-GO wrapped n-Al/n-Fe_2O_3 composite. We hypothesize that a selective r-GO coating of either n-Al or n-Fe_2O_3 inhibits fuel/oxidizer transport during reaction.

Table 7. Average ignition delay and standard deviation of three trials of the baseline thermite, r-GO wrapped thermite formulations, selectively r-GO wrapped thermite, GO wrapped thermite, and heat-treated GO wrapped thermite in the single-mode resonant microwave cavity. Reported averages and standard deviations are from 3 trials of each formulation.

Material	Average Ignition Delay [s]
r-GO Thermite Composite (10 wt.% r-GO)	1.37 ± 0.33
r-GO Thermite Composite (20 wt.% r-GO)	1.27 ± 0.23
r-GO Thermite Composite (30 wt.% r-GO)	0.43 ± 0.37
r-GO wrapped n-Fe_2O_3 with n-Al (30 wt.% r-GO)	1.33 ± 0.13
r-GO wrapped n-Al with n-Fe_2O_3 (30 wt.% r-GO)	1.53 ± 0.33
Thermite (30/70 wt.% ratio n-Al to n-Fe_2O_3)	4.34 ± 0.45
Untreated GO Thermite Composite (30 wt.% GO)	>60[a]
Heat-Treated GO Thermite Composite (30 wt.% GO, 5 min)	1.28 ± 0.26
Heat-Treated GO Thermite Composite (30 wt.% GO, 10 min)	0.24 ± 0.25
Heat-Treated GO Thermite Composite (30 wt.% GO, 15 min)	4.88 ± 1.85

a) 4 out of 6 trials had no ignition after 60 s, and 2 out 6 trials had ignition delay averaging ~4.3 seconds.

5.2.1.4. Thermal Switching of Thermite Microwave Ignitability

The heat-treated GO wrapped thermite composites (30 wt.% GO) were microwave ignited under the same conditions as the r-GO wrapped thermites. Untreated GO wrapped thermites exhibited no ignition after 60 seconds of microwave illumination in four out of six experiments (Table 7). In these formulations, when ignition did occur, it did so after an average time of ~4.3 s—an ignition delay time similar to that of baseline thermite (no wrapping). We hypothesize the reason for this drastic difference in ignition delay times for the same material is a result of incomplete GO wrapping of the thermite, which was observed in SEM images (Figure 29d). In the majority of GO-wrapped thermite microwave ignition experiments, ignition inhibition is a result of oxygen-containing groups present on the graphene lattice, which inhibit charge localization and electron mobility, resulting in low microwave absorptivity and high reflectivity [72].

By thermally treating GO wrapped thermites, reduction of the GO occurs, which causes a decrease of ignition delay times. Ignition delay experiments indicate that the optimum heat treatment time in argon at 400 °C for GO-wrapped thermites is between 5 to 15 minutes. GO composite thermites with 5-minute heat treatments exhibit average ignition delays of ~1.28 s. By increasing the heat treatment time to 10 minutes, the thermite ignition delay is further reduced to

~0.24 s, which is a shorter ignition delay time than that of thermites wrapped in vendor-supplied r-GO (Table 7). The reduction in ignition delay times resulting from increasing the heat treatment from 5 to 10 minutes is a result of further GO reduction, as confirmed by XPS of heat-treated thermites (Figure 32), which show that increasing heat treatment duration from 5-minute to 10-minute produces an increase in C1s to O1s atomic ratio consistent with graphene reduction [74]. However, increasing the heat treatment duration from 10 to 15 min produced an increase in average ignition delay to 4.88 s and associated decrease in C1s to O1s atomic ratio from 1.18 to 0.84. The 15 min heat treatment ignition delay times are similar to the baseline thermite (4.34 s). This increase in ignition delay and associated decrease in C1s to O1s atomic ratio are consistent with graphene lattice damage occurring during extended heat treatment beyond 10 minutes duration.

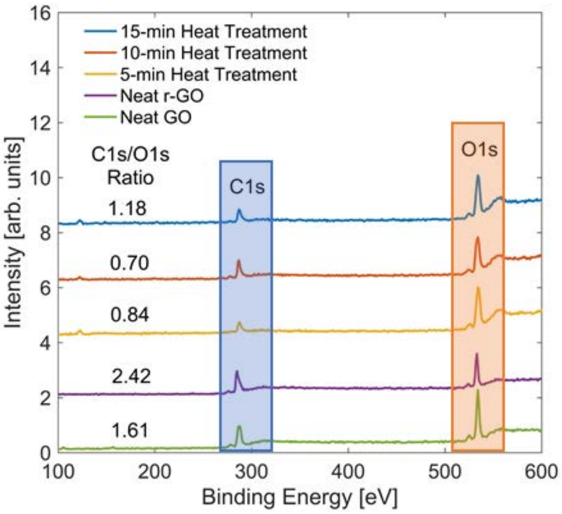

Figure 32. X-ray photoelectron spectroscopy of neat r-GO/GO powder and heat treated, GO-wrapped thermite formulations. XPS data for each heat treatment condition are offset for presentation.

5.2.2. Microwave Burning Rate Modulation of Wired Propellants Through Eddy Current Loss Mechanisms

5.2.2.1. Wire Propellant Combustion Experiments

The method through which burning rate can be microwave modulated within wired propellants is described in Figure 33. Wire propellant experiments were conducted in a microwave single mode resonant cavity with field strengths of 38-91 kV/m. Under microwave application, significant increase of wire heating is observed, which results in burning rate enhancement. In Figure 33, still images sequences are shown of the four different wires tested with and without microwave. For the wire propellants burned without microwave application, acceleration of burning rate near the wire is observed as a result of increased heat transport within the wire. When a continuous microwave field is applied to the propellant, the burning rate of the propellant near the wire increases significantly. The resulting burning rate increase is a result of both aforementioned improved thermal transport and eddy current heating of the wire. Other heating mechanisms, discussed in Ref. [29] including direct coupling to background electron populations resulting in higher temperature plasmas feeding back to the burning surface may be possible. Condense phase dielectric heating of the composite propellant could be another mechanism, however previous study suggested that dielectric heating should be low [29,34,35,149].

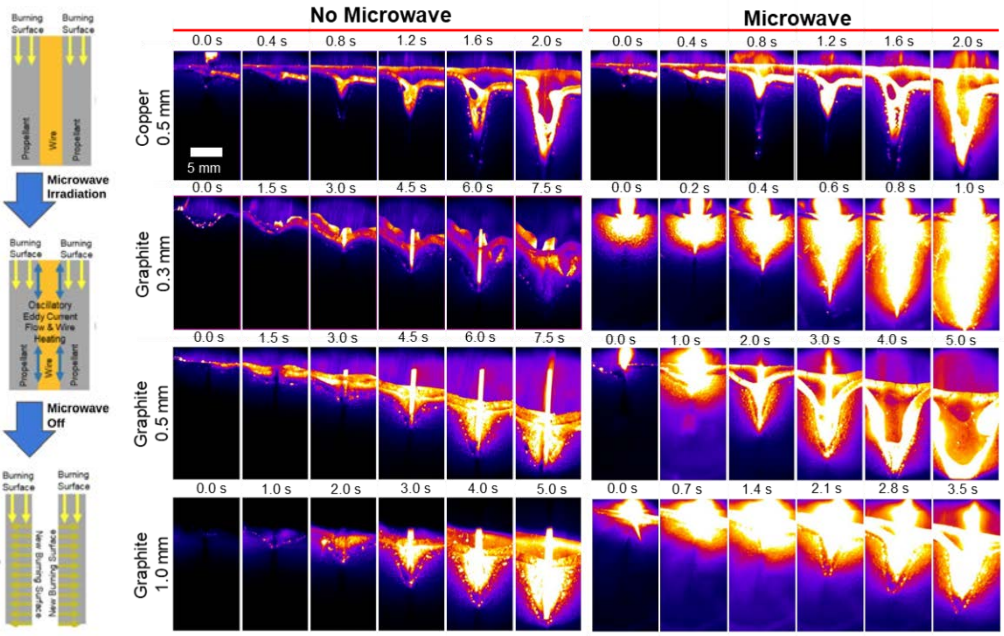

Figure 33. ***Left:*** *Phenomenological description of microwave burning rate modulation of wired propellants.* ***Right:*** *Light emission still image sequence of wire propellant strands burning without (left) and with (right) microwave field application. False coloring is used to indicate emission intensity. Camera exposure and aperture settings are the same for each formulation with and without microwave.*

Eddy current heating occurs when an alternating field is applied to a conductive material and induces a flowing current through the resistance of the conductor, which results in energy dissipation in the form of heat. As frequency increases, eddy current heating will increase quadratically, where the electromagnetic field fully penetrates the material resulting in no skin effects [150]. However, in the case of fast alternating fields such as microwave frequency, full penetration of the field into the wire does not occur, as skin depths are smaller than wire diameters, resulting in lowering power dissipation when compared to the quasi-static condition, but will still increase at higher field frequency. Moreover, eddy current heating increases as electrical resistivity decreases. Experimental results show for 0.5 mm diameter wires, that the copper wire has a higher degree of burning rate enhancement (138%) than graphite wire (95.7%) (Table 8). This may be a result of copper having both a lower electrical resistivity of approximately 800 times and higher thermal conductivity when compared to graphite. However, with lower electrical resistivity, the field penetration depth decreases, as seen in Table 7, which may result in lower heating in the wire core. As the wire diameter decreases, the burning rate enhancement near the wire increases. Comparing a 1 mm and 0.3 mm graphite wire propellant burning rates enhancement, the degree of enhancement increases by 10 times, from 62.5% to 700%, respectfully. The increased burning rate enhancement occurring with decreased graphite wire diameter are expected to be a result of a combination of decreased thermal mass of the 0.3 mm wire and higher field penetration depth per volume.

Table 8. Wire propellant material with corresponding wire diameter, experimentally observed atmospheric pressure propellant burning rate with and without microwave enhancement measured at the flame front near the wire, and burning rate enhancement percentage. Burning rates are reported as the average and standard deviation of three experiments.

Wire Material	**Wire Diameter (mm)**	**No Microwave Burning Rate (cm/s)**	**Microwave Burning Rate (cm/s)**	**Burning Rate Enhancement (%)**
Copper	0.5	0.37 ± 0.14	0.88 ± 0.04	137.8
Graphite	0.3	0.17 ± 0.02	1.36 ± 0.24	700
Graphite	0.5	0.23 ± 0.08	0.45 ± 0.05	95.7
Graphite	1	0.24 ± 0.06	0.39 ± 0.01	62.5

5.2.2.2. Functionalized, Wired Energetic Combustion Experiments

To further investigate eddy current heating, functionalized energetic wire propellants were tested at the same conditions. Under atmospheric pressure without microwave enhancement, the propellant strand burned approximately linearly for 8 seconds (Figure 34). Conductive heat transfer down the wire is expected to be lower as compared to the solid wired propellant conditions because little increase in burning rate near the wire can be observed in the baseline case (without microwave). This is due to higher conductivity nanographene particles being encapsulated in a matrix of AP and HTPB. However, under microwave field application, the propellant burning near the energetic wire increases significantly. In Figure 34, a burning surface pocket can be seen in the microwave case at 0.8s, which is a result of microwave energy heating of the energetic wire. This is expected to be a result from eddy current heating of the nanoscale graphite in the energetic wire. In this case, eddy current heating can be more uniform due the graphite being several orders of magnitude smaller than the skin penetration depth and the RF-transparency of AP and binder surrounding the nanographene allows for microwaves to be transmitted. It was not possible to determine a burning rate enhancement due to the high optical density of the graphite propellant blocking emission.

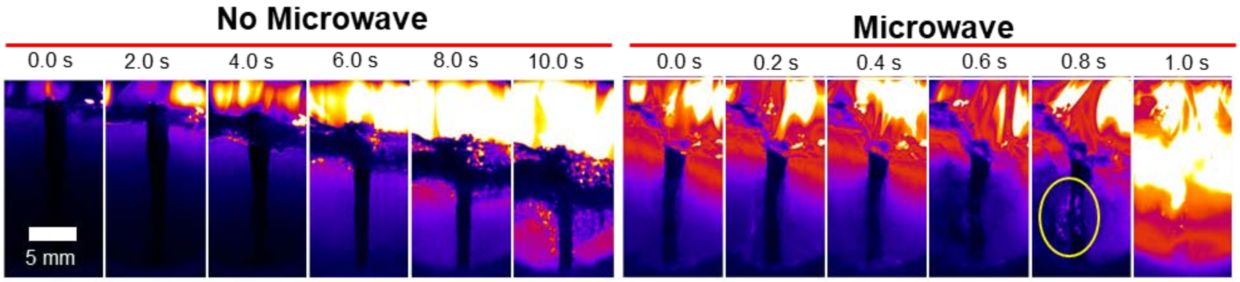

Figure 34. Light emission still image sequence of UV-Cured Propellant Manufacture with Functionalize Energetic Wires strands burning without (right) and with microwave field application. False coloring is used to indicate emission intensity. The yellow circle indicates a burning surface pocket formed near the energetic wire. Camera exposure and aperture settings are the same for each formulation with and without microwave.

5.2.3. Dielectric Property Measurement of AP Composite Solid Propellants

5.2.3.1. Dielectric Property Measurement

A summary of the results for all room-temperature data collected is given in Figure 35. The transmission line method was collected continuously from 2.3 GHz to 2.65 GHz. The data overlays cAP fNaNO$_3$, BiAP fNaNO$_3$, and Teflon (standard), as a function of frequency. In the transmission line setup, Teflon measured real permittivities of 1.97 are within a 5% error of the actual value [109], validating experimental configuration and analytical techniques. The average real and imaginary permittivities of CAP fNaNO$_3$ propellant articles is 5.83 and 0.228, respectively and average BiAP fNaNO$_3$ real and complex permittivities are 5.87 and 0.266 respectively. The loss tangent for both materials is <<1, which is considered to be a low-loss medium and good dielectric. Furthermore, BiAP fNaNO$_3$ is more susceptible to microwave heating. This is expected to be a result of crystal interface. This is due to the number of interfaces within the bimodal AP propellant having more binder crystal interfaces. However this is a small difference between the two propellant dielectric properties, which changing the aluminum loading should change dielectric properties considerably more [69].

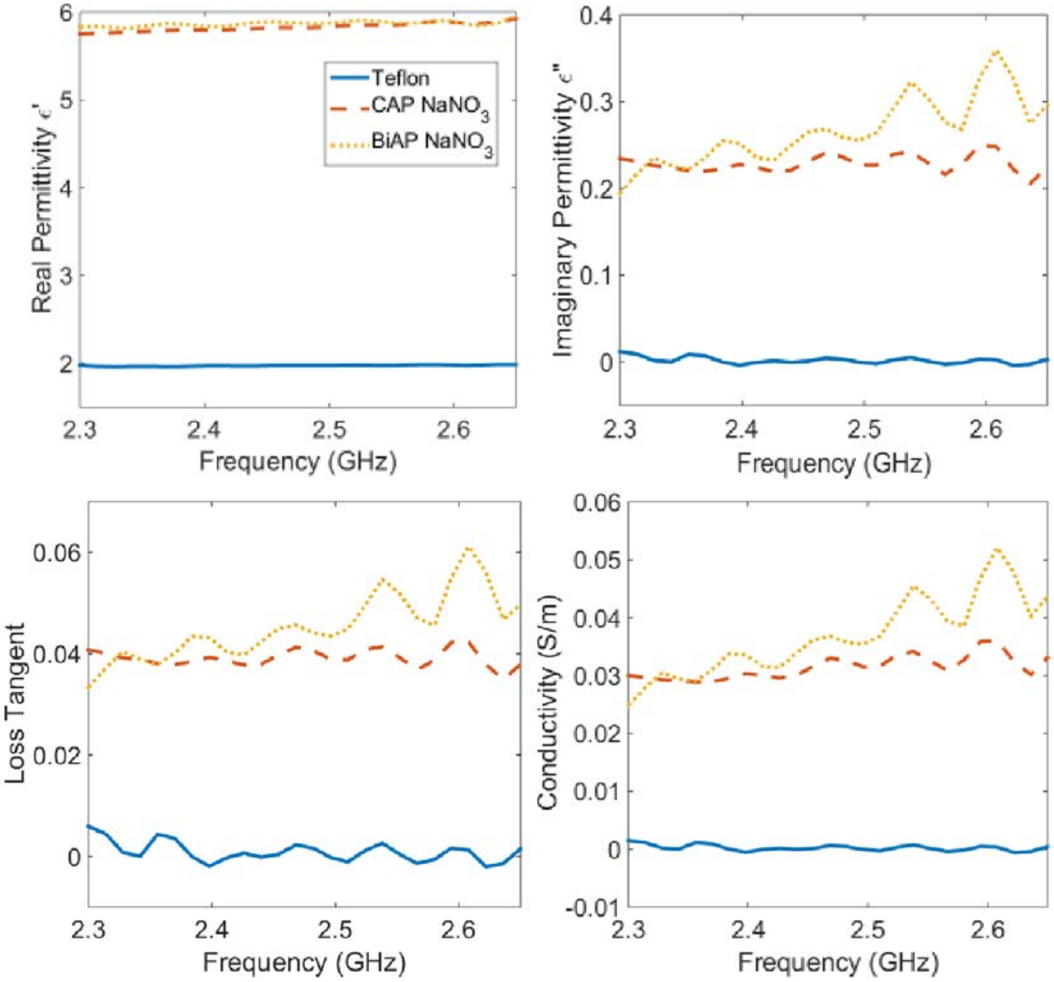

Figure 35. Graph of Teflon, CAP fNaNO3, and BiAP fNaNO3 real and imaginary permittivity, loss tangent, and conductivity as a function of frequency measured at room temperature.

5.2.3.2. COMSOL Cavity Simulation

Initial COMSOL simulations of a loaded single-mode resonant microwave cavity operating at 2.45 GHz have been developed. This model will be modified by insertion of propellant strands having as-measured or modeled microwave properties. The cavity was designed to model the continuous microwave generator setup, seen in Figure 36. In this setup, a 1 kW magnetron outputs into WR-284 waveguide to a Gerling Universal Applicator, with a quartz tube holder of OD 36 mm. In this setup, propellant will be burnt under 2.45 GHz microwave field. To understand the field strength in the condense phase of this setup (preiginiton), a model with the quartz tube and propellant strand in the cavity and a model with the propellant strand and without the quartz tube is shown in Figure 36. It is shown that field strength is ~40% lower with the quartz tube (36.3 kV/m) as compared to without the tube (59.1 kV/m). However in a propellant strand configuration, it is noted that burning propellant without a quartz tube is not feasible. COMSOL was also utilized to run RF heating of both types of propellants, in the same cavity. Results from this simulation can be seen in Table 9. As expected, bimodal AP fine $NaNO_3$ heating was greater due to its higher imaginary permittivity. Heating in a quartz tube and without in the waveguide of coarse AP fine $NaNO_3$ and bimodal AP fine $NaNO_3$ was 351.09 K and 394.16 K and, 358.73 K and 407.44 K respectively.

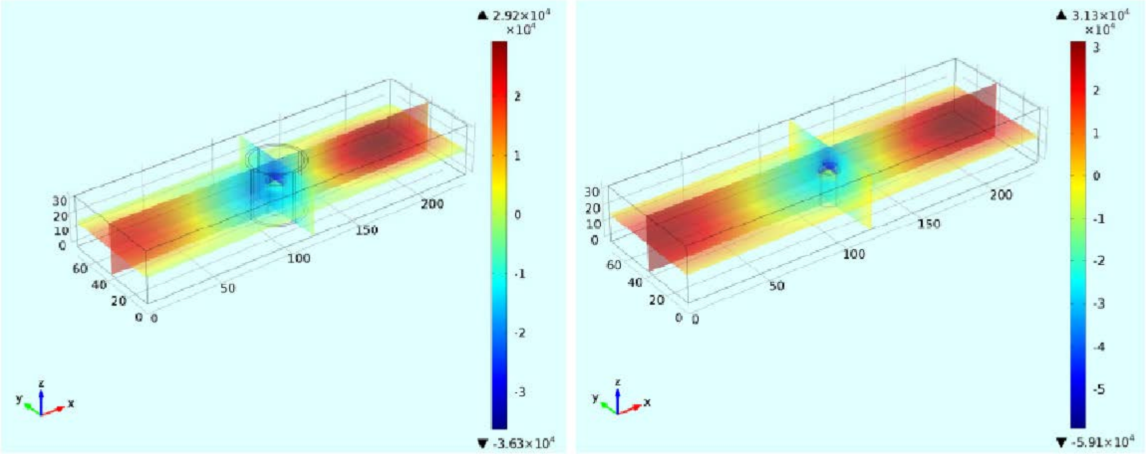

Figure 36. Comsol simulation of propellant-loaded single-mode resonant microwave cavity with 36 mm OD quartz tube (left) and without quartz tube (right). Multiple slices show the E-field strength (V/m) through the propellant center axis. Both simulations are shown for measured dielectric properties of the bimodal AP, fine NaNO3 propellant formulation.

Table 9. Simulated loaded cavity reflection loss and isotropic, temperature-invariant heating times to heat propellant articles to an average temperature of 100 °C

	VSWR		**ΔT in 20 s of MW Heating (K)**	
Propellant	**No Quartz**	**Quartz Tube**	**No Quartz**	**Quartz Tube**
BiAP, $fNaNO_3$	1.229	2.259	407.44	358.73
cAP, $fNaNO_3$	1.226	2.256	394.16	351.09

6. Summary and Conclusions

This effort demonstrates a number of methods through which the energy release rate of a solid propellant can be dynamically controlled through exploiting materials effects to localize microwave energy absorption to either the gas phase flame or the condensed phase reactants.

With respect to the gas phase, it was found that doping of an energetic material with reagents producing strongly electro-positive species (i.e. alkali metals in form of metal nitrates such as sodium nitrate) within the flame, in order to substantially increase the electron population of the flame was an effective means to enhance microwave absorption of the gas phase and to further increase the degree to which the electric field component of a microwave-frequency field can throttle the burning rate of a solid propellant. While the dielectric loss of aluminum oxide is quite low at room temperature, the exponential dependence of its loss coefficient with temperature was found to lead to observable light emission enhancement from aluminum oxide combustion product plumes during microwave modulation, suggesting that efficient microwave absorption may also occur in high temperature metal oxides within the combustion plume. These modes of energy transfer all lead to increased energy feedback to the burning surface and have been demonstrated to enable up to a 60% enhancement in propellant linear burning rate. The mechanism of microwave interaction with energetic material flames has been studied in simulation of a 1-D planar flame. It was found that electromagnetic shielding of the flame/s inner core can be significant and is exacerbated by high alkali concentrations (i.e. high electron populations). This suggests an optimum dopant level to achieve microwave field penetration to the flame core exists. The alkali doping technique was further demonstrated as a means with which to modulate the optical light emission intensity (brightness) of a pyrotechnic flame. A new two-photon laser induced fluorescence scheme with significantly greater signal to noise in comparison to single photon techniques has been demonstrated on gas phase alkali-doped and composite propellant flames. In alkali-doped composite solid propellant flames, the technique shows that plasma flame kernel formations occur near the propellant burning surface and result from localized areas of high sodium concentration.

Methods focusing on microwave interaction with condensed phase reactants have demonstrated the ability to highly localize microwave energy absorption and to accelerate burning rates by multiple orders of magnitude. The development of nanoscale thermites with thermally switchable microwave absorptivities has been demonstrated through wrapping of nanoscale thermite clusters with either graphene oxide (GO) or reduced graphene oxide (rGO). It was found that thermites wrapped in GO are highly microwave reflective and are not microwave-ignitable under the influence of steady state, high-power microwave fields for long durations of time (up to 60 seconds of microwave irradiation). Heating of these thermites was found to lead to GO reduction and as a result, drastic changes in the thermites' microwave absorptivity, which enabled microwave-ignition of the thermites in as short as 0.2 to 0.3 seconds. The development of such materials, with thermally switchable microwave absorption properties may prevent parasitic microwave energy loss within the bulk condensed phase of an energetic material and enable highly localized microwave loss to the energetic material burning surface. Application of microwave fields to wired propellants (i.e. propellants with spatially graded electrical conductivity) has been demonstrated as a technique with which to achieve multiple orders of magnitude dynamic control over propellant burning rate. A burning rate enhancement of 700%

has been demonstrated in use of graphite wires in AP composite propellant where the radius of the wire is matched to the microwave skin thickness.

Taken together, these techniques demonstrate the high degree of utility that can be enabled in design of energetic materials with electromagnetic function. However, this research program also demonstrates that the development of efficient, electromagnetically active energetic materials will require a number of considerations. Electromagnetically ‘smart’ energetic materials have several applications, including development of throttled solid rocket motors, enhanced propellant ignition and flame spread, and dynamically controlled light emission pyrotechnics, among others.

7. References

[1] Fabignon Y, Dupays J, Avalon G, Vuillot F, Lupoglazoff N, Casalis G, et al. Instabilities and pressure oscillations in solid rocket motors. Aerospace Science and Technology 2003;7:191–200. https://doi.org/10.1016/s1270-9638(02)01194-x.

[2] Chakravarthy SR, Seitzman JM, Price EW, Sigman RK. Intermittent burning of ammonium perchlorate-hydrocarbon binder monomodal matrixes, sandwiches, and propellants. Journal of Propulsion and Power 2004;20:101–9.

[3] Parr TP, Hanson-Parr DM. Optical Diagnostics of Solid-Propellant Flame Structures. In: Yang V, Brill TB, Ren W, editors. Solid Propellant Chemistry, Combustion, and Motor Interior Ballistics, Reston, VA: AIAA; 2000, p. 381–411.

[4] Culick FE, Kuentzmann P. Unsteady motions in combustion chambers for propulsion systems. NATO Research and Technology Organization; 2006.

[5] Sawka WN, Katzakian A, Grix C. Solid State Digital Propulsion Cluster Thrusters for Small Satellites Using High Performance Electrically Controlled Extinguishable Solid Propellants. The Annual AIAA/USU Conference on Small Satellites, 2005, p. 1–7.

[6] Meyerriecks W, Kosanke KL. Color values and spectra of the principal emitters in colored flames. J Pyrotech 2003;18:710–31.

[7] Sabatini JJ, Nagori AV, Chen G, Chu P, Damavarapu R, Klapötke TM. High-nitrogen-based pyrotechnics: longer- and brighter-burning, perchlorate-free, red-light illuminants for military and civilian applications. Chemistry 2012;18:628–31.

[8] Li J, Litzinger TA, Thynell ST. Plasma Ignition and Combustion of JA2 Propellant. J Propul Power 2005;21:44–53.

[9] Li J, Litzinger TA, Das M, Thynell ST. Recombination of electrothermal plasma and decomposition of plasma-exposed propellants. J Propul Power 2006;22:1353–61.

[10] Keidar M, Boyd ID. Ablation study in the capillary discharge of an electrothermal gun. J Appl Phys 2006;99:053301.

[11] Alimi R, Berdichevsky V. Mechanism of solid propellant combustion submitted to a high plasma flux. Propellants Explos Pyrotech 2008;33:118–21.

[12] Woodley CR, Fuller S. Apparent Enhanced Burn Rates of Solid Propellants due to Plasmas, n.d., p. 153.

[13] Koleczko A, Ehrhardt W, Kelzenberg S, Eisenreich N. Plasma ignition and combustion. Propellants Explos Pyrotech 2001;26:75–83.

[14] Birk A, Del Guercio M, Kinkennon A, Kooker DE, Kaste P. Interrupted-Burning Tests of Plasma-Ignited JA2 and M30 Grains in a Closed Chamber. Propellants Explos Pyrotech 2000;25:133–42.

[15] Porwitzky AJ, Keidar M, Boyd ID. On the Mechanism of Energy Transfer in the Plasma‐Propellant Interaction. Propellants Explos Pyrotech 2007;32:385–91.

[16] Li X, Li R, Jia S, Zhang Y. Interaction features of different propellants under plasma impingement. J Appl Phys 2012;112:063303.

[17] Porwitzky AJ, Scalabrin LC, Keidar M, Boyd ID. Chemically reacting plasma jet expansion simulation for application to electrothermal chemical guns. 16th Plasmadynamics and Lasers Conf., 2007.

[18] Ju Y, Sun W. Plasma assisted combustion: Dynamics and chemistry. Prog Energy Combust Sci 2015;48:21–83.

[19] Starikovskiy A. Physics and chemistry of plasma-assisted combustion. Philosophical Transactions of the Royal Society of London Series A: Physical and Engineering Sciences 2015;373:20150074.

[20] Ombrello T, Ju Y. Kinetic Ignition Enhancement of H2 Versus Fuel-Blended Air Diffusion Flames Using Nonequilibrium Plasma. IEEE Trans Plasma Sci IEEE Nucl Plasma Sci Soc 2008;36:2924–32.

[21] Ombrello T, Ju Y, Fridman A. Kinetic Ignition Enhancement of Diffusion Flames by Nonequilibrium Magnetic Gliding Arc Plasma. AIAA Journal 2008;46:2424–33.

[22] Mintoussov E, Pancheshnyi S, Starikovskii A. Propane-Air Flame Control by Non-Equilibrium Low-temperature Pulsed Nanosecond Barrier Discharge. 42nd AIAA Aerospace Sciences Meeting and Exhibit, American Institute of Aeronautics and Astronautics; 2004.
[23] Douda BE, Blunt RM, Bair EJ. Visible Radiation from illuminating-flare flames: strong emission features. Journal of the Optical Society of America 1970;60:1116–9.
[24] Tanner JE Jr. A mathematical model of flare plume combustion and radiation. Naval Weapons Support Center Crane; 1975.
[25] Dillehay DR. Resonance line broadening of alkali metals in pyrotechnic flames. Longhorn Army Ammunition Plant, Marshall TX; 1983.
[26] Webster H, Tanner JE, E DB. Theoretical Light Yields form Illuminating Flare Compositions. Naval Weapons Support Center, Crane, USA; 1973.
[27] Douda BE, Bair EJ. Radiative transfer model of a pyrotechnic flame. J Quant Spectrosc Radiat Transf 1974;14:1091–105.
[28] Gann RG, Kaufman F, Biondi MA. Interferometric study of the chemiluminescent excitation of sodium by active nitrogen. Chem Phys Lett 1972;16:380–4.
[29] Barkley SJ, Zhu K, Lynch JE, Michael JB, Sippel TR. Microwave plasma enhancement of multiphase flames: On-demand control of solid propellant burning rate. Combust Flame 2019;199:14–23.
[30] Sutton WH. Microwave processing of ceramic materials. Am Ceram Soc Bull 1989;68:376–86.
[31] Gupta M, Leong EW. Microwaves and Metals. Wiley; 2008.
[32] Rybakov KI, Olevsky EA, Krikun EV. Microwave Sintering: Fundamentals and Modeling. J Am Ceram Soc 2013;96:1003–20.
[33] Higginbotham Duque AL, Perry WL, Anderson Cook CM. Complex Microwave Permittivity of Secondary High Explosives. Propellants Explos Pyrotech 2014;39:275–83.
[34] Daily ME, Glover BB, Son SF, Groven LJ. X-Band Microwave Properties and Ignition Predictions of Neat Explosives. Propellants Explos Pyrotech 2013;38:810–7.
[35] Hasue K, Tanabe M, Watanabe N. Initiation of some energetic materials by microwave heating. Propellants Explos Pyrotech 1990;15:181–6.
[36] Vargas E, Pantoya ML, Saed MA, Weeks BL. Advanced susceptors for microwave heating of energetic materials. Mater Des 2016;90:47–53.
[37] Crane CA, Pantoya ML, Weeks BL. Investigating the trade-offs of microwave susceptors in energetic composites: microwave heating versus combustion performance. J Appl Phys 2014;115:104106.
[38] Starikovskaia SM. Plasma assisted ignition and combustion. Journal of Physics D-Applied Physics 2006;39:R265–99.
[39] Michael JB, Chng TL, Miles RB. Sustained propagation of ultra-lean methane/air flames with pulsed microwave energy deposition. Combust Flame 2013;160:796–807.
[40] Shuler KE, Weber J. A Microwave Investigation of the Ionization of Hydrogen‐Oxygen and Acetylene‐Oxygen Flames. J Chem Phys 1954;22:491–502.
[41] Raizer YP, Allen JE. Gas discharge physics. vol. 2. Springer Berlin; 1997.
[42] Stephen DT, Others. Ionisation in premixed fuel-lean flames of H 2, O 2 and N 2. Part 2.—Ions from alkali-metal additives. J Chem Soc Faraday Trans 1995;91:835–41.
[43] Lijnse PL. Electronic-excitation transfer collisions in flames—VI. Interpretation of the temperature dependence of alkali-quenching by N2 and general conclusions about the energy transfer mechanism. J Quant Spectrosc Radiat Transf 1974;14:1143–55.
[44] de Groot JJ, van Vliet JA. The High-Pressure Sodium Lamp. Macmillan International Higher Education; 1986.
[45] van der Mullen JA. Excitation equilibria in plasmas: A classification. Phys Rep 1990;191:109–220.
[46] Hagelaar GJ, Pitchford LC. Solving the Boltzmann equation to obtain electron transport coefficients and rate coefficients for fluid models. Plasma Sources Sci Technol 2005;14:722.
[47] Browner RF, Winefordner JD. Measurement of flame temperatures by a two-line atomic absorption method. Anal Chem 1972;44:247–52.

[48] van Eyk PJ, Ashman PJ, Alwahabi ZT, Nathan GJ. Quantitative measurement of atomic sodium in the plume of a single burning coal particle. Combust Flame 2008;155:529–37.
[49] Miles RB, Udd E, Zimmermann M. Quantitative flow visualization in sodium vapor seeded hypersonic helium. Appl Phys Lett 1978;32:317–9.
[50] Barker P, Bishop A, Rubinsztein-Dunlop H. Supersonic velocimetry in a shock tube using laser enhanced ionisation and planar laser induced fluorescence. Appl Phys B 1997;64:369–76.
[51] Weiland KJR, Wise ML, Smith GP. Laser-induced fluorescence detection strategies for sodium atoms and compounds in high-pressure combustors. Appl Opt 1993;32:4066–73.
[52] Bischel WK, Perry BE, Crosley DR. Two-photon laser-induced fluorescence in oxygen and nitrogen atoms. Chem Phys Lett 1981;82:85–8.
[53] Goldsmith JEM. Two-photon-excited stimulated emission from atomic hydrogen in flames. J Opt Soc Am B, JOSAB 1989;6:1979–85.
[54] Aldén M, Westblom U, Goldsmith JE. Two-photon-excited stimulated emission from atomic oxygen in flames and cold gases. Opt Lett 1989;14:305–7.
[55] Aldén M, Edner H, Grafström P, Svanberg S. Two-photon excitation of atomic oxygen in a flame. Opt Commun 1982;42:244–6.
[56] Tjossem PJH, Cool TA. Detection of atomic hydrogen in flames by resonance four-photon ionization at 365 nm. Chem Phys Lett 1983;100:479–83.
[57] Zhang Z, Shneider MN, Miles RB. Coherent microwave rayleigh scattering from resonance-enhanced multiphoton ionization in argon. Phys Rev Lett 2007;98:265005.
[58] Kulatilaka WD, Gord JR, Katta VR, Roy S. Photolytic-interference-free, femtosecond two-photon fluorescence imaging of atomic hydrogen. Opt Lett 2012;37:3051–3.
[59] Richardson DR, Roy S, Gord JR. Femtosecond, two-photon, planar laser-induced fluorescence of carbon monoxide in flames. Opt Lett 2017;42:875–8.
[60] Berrocal E, Conrad C, Püls J, Arnold CL, Wensing M, Linne M, et al. Two-photon fluorescence laser sheet imaging for high contrast visualization of atomizing sprays. OSA Continuum, OSAC 2019;2:983–93.
[61] Allen JE, Anderson WR, Crosley DR, Fansler TD. Energy transfer and quenching rates of laser-pumped electronically excited alkalis in flames. Symp Combust 1979;17:797–809.
[62] Higginbotham Duque AL, Perry WL, Anderson-Cook CM. Complex microwave permittivity of secondary high explosives. Propellants Explos Pyrotech 2014;39:275–83.
[63] Perry WL, Sewell TD, Glover BB, Dattelbaum DM. Electromagnetically induced localized ignition in secondary high explosives. J Appl Phys 2008;104:094906.
[64] Biswas P, Mulholland GW, Rehwoldt MC, Kline DJ, Zachariah MR. Microwave absorption by small dielectric and semi-conductor coated metal particles. J Quant Spectrosc Radiat Transf 2020;247:106938.
[65] Meir Y, Jerby E. Thermite powder ignition by localized microwaves. Combust Flame 2012;159:2474–9.
[66] Alibay Z, Kline DJ, Rehwoldt MC, Biswas P, Herrera S, Wang H, et al. Mechanism of microwave-initiated ignition of sensitized energetic nanocomposites. Chem Eng J 2021;415:128657.
[67] Baker-Jarvis J, Janezic MD, Degroot DC. High-frequency dielectric measurements. IEEE Instrum Meas Mag 2010;13:24–31.
[68] Perry WL, Cooke DW, Katz JD, Datye AK. On the possibility of a significant temperature gradient in supported metal catalysts subjected to microwave heating. Catal Letters 1997;47:1–4.
[69] Ho YS, Kramer JJ. Microwave Dielectric Properties of Metal Filled Particulate Composites. Materials Research Society Symposia Proceedings, vol. 124, 1988, p. 161–6.
[70] Dreyer DR, Park S, Bielawski CW, Ruoff RS. The chemistry of graphene oxide. Chem Soc Rev 2010;39:228–40.
[71] Menéndez JA, Arenillas A, Fidalgo B, Fernández Y, Zubizarreta L, Calvo EG, et al. Microwave heating processes involving carbon materials. Fuel Process Technol 2010;91:1–8.
[72] Hu H, Zhao Z, Zhou Q, Gogotsi Y, Qiu J. The role of microwave absorption on formation of

graphene from graphite oxide. Carbon N Y 2012;50:3267–73.
[73] Wang C, Han X, Xu P, Zhang X, Du Y, Hu S, et al. The electromagnetic property of chemically reduced graphene oxide and its application as microwave absorbing material. Appl Phys Lett 2011;98:072906.
[74] Stankovich S, Dikin DA, Piner RD, Kohlhaas KA, Kleinhammes A, Jia Y, et al. Synthesis of graphene-based nanosheets via chemical reduction of exfoliated graphite oxide. Carbon 2007;45:1558–65.
[75] Wang L, Jia X, Li Y, Yang F, Zhang L, Liu L, et al. Synthesis and microwave absorption property of flexible magnetic film based on graphene oxide/carbon nanotubes and Fe 3 O 4 nanoparticles. J Mater Chem A Mater Energy Sustain 2014;2:14940–6.
[76] Hu C, Mou Z, Lu G, Chen N, Dong Z, Hu M, et al. 3D graphene--Fe3O4 nanocomposites with high-performance microwave absorption. Phys Chem Chem Phys 2013;15:13038–43.
[77] Han M, Yin X, Kong L, Li M, Duan W, Zhang L, et al. Graphene-wrapped ZnO hollow spheres with enhanced electromagnetic wave absorption properties. J Mater Chem A Mater Energy Sustain 2014;2:16403–9.
[78] Xu H-L, Bi H, Yang R-B. Enhanced microwave absorption property of bowl-like Fe3O4 hollow spheres/reduced graphene oxide composites. J Appl Phys 2012;111:07A522.
[79] Xu S, Zhong G, Chen C, Zhou M, Kline DJ, Jacob RJ, et al. Uniform, Scalable, High-Temperature Microwave Shock for Nanoparticle Synthesis through Defect Engineering. Matter 2019;1:759–69.
[80] Ma X, Zachariah MR, Zangmeister CD. Crumpled Nanopaper from Graphene Oxide. Nano Lett 2012;12:486–9.
[81] King MK. Analytical modeling of effects of wires on solid motor ballistics. J Propul Power 1991;7:312–21.
[82] Caveny LH, Glick RL, Caveny LH, Glick RL, Caveny LH, Glick RL. Influence of embedded metal fibers on solid- propellant burning rate. J Spacecr Rockets 1967;4:79–85.
[83] Bakhman NN, Lobanov IN. Effect of heat-conducting elements on burning rate. Combustion, Explosion and Shock Waves 1975;11:424–8.
[84] Lawrence R. Method of increasing propellant burning rate by the use of high conductive wires. Patent 3793097, 1974.
[85] Winer R. Use of graphite fibers to augment propellant burning rate. Patent 4072546, 1978.
[86] Shuling C, Fengsheng L. Influence of long metal wires on combustion of double-base propellants. Combust Flame 1982;45:213–8.
[87] Brewster MQ, Hardt BE. Influence of metal agglomeration and heat feedback on composite propellant burning rate. J Propul Power 1991;7:1076–8.
[88] Bakhman NN, Lobanov IN. Influence of the diameter of the heat-conducting elements on their efficiency during the combustion of condensed systems. Combustion, Explosion and Shock Waves 1983;19:42–6.
[89] Isert S, Lane CD, Gunduz IE, Son SF. Tailoring burning rates using reactive wires in composite solid rocket propellants. Proc Combust Inst 2016;36:2283–90.
[90] Gordon S, McBride BJ. Computer Program for Calculation of Complex Chemical Equilibrium. NASA; 1994.
[91] Drawin HW, Emard F. Optical Escape Factors for Bound-bound and Free-bound Radiation from Plasmas. I. Constant Source Function. Beiträge Aus Der Plasmaphysik 1973;13:143–68.
[92] Pancheshnyi S, Biagi S, Bordage MC, Hagelaar GJM, Morgan WL, Phelps AV, et al. The LXCat project: Electron scattering cross sections and swarm parameters for low temperature plasma modeling. Chem Phys 2012;398:148–53.
[93] Alves LL. The IST-LISBON database on LXCat. J Phys Conf Ser 2014;565:012007.
[94] Igenbergs K, Schweinzer J, Bray I, Bridi D, Aumayr F. Database for inelastic collisions of sodium atoms with electrons, protons, and multiply charged ions. At Data Nucl Data Tables 2008;94:981–1014.
[95] Ratnavelu K, Ong WE. Electron and positron scattering from atomic potassium. Eur Phys J D

2011;64:269–85.

[96] Zatsarinny O, Bartschat K, Babaeva NY, Kushner MJ. Electron collisions with cesium atoms—benchmark calculations and application to modeling an excimer-pumped alkali laser. Plasma Sources Sci Technol 2014;23:035011.

[97] Laroussi M. Interaction of microwaves with atmospheric pressure plasmas. Int J Infrared Millimeter Waves 1995;16:2069–83.

[98] Sengupta I, Chakraborty S, Talukdar M, Pal SK, Chakraborty S. Thermal reduction of graphene oxide: How temperature influences purity. J Mater Res 2018;33:4113–22.

[99] Balanis CA. Advanced Engineering Electromagnetics. John Wiley & Sons; 2012.

[100] Laug OB. Evaluation of the A test method for measuring microwave oven cooking efficiency. Institute for Applied Technology, National Bureau of Standards; 1977.

[101] Hartung G, Hult J, Kaminski CF. A flat flame burner for the calibration of laser thermometry techniques. Meas Sci Technol 2006;17:2485.

[102] Cool TA. Quantitative measurement of NO density by resonance three-photon ionization. Appl Opt 1984;23:1559.

[103] Green KM, Borras MC, Woskov PP, Flores GJ, Hadidi K, Thomas P. Electronic excitation temperature profiles in an air microwave plasma torch. IEEE Trans Plasma Sci IEEE Nucl Plasma Sci Soc 2001;29:399–406.

[104] Griem HR. Principles of Plasma Spectroscopy. Cambridge University Press; 2005.

[105] Kramida A, Ralchenko Y, Reader J, Others. NIST atomic spectra database lines form. NIST Atomic Spectra Database (ver 5 2)[Online] 2014.

[106] Wiese WL, Smith MW, Miles BM. Atomic transition probabilities. Vol. 2: Sodium through Calcium. A critical data compilation. 1969.

[107] Malacara D. Color vision and colorimetry: Theory and applications. Color Res Appl 2003;28:77–8.

[108] Paula AL de, Rezende MC, Barroso JJ. Experimental measurements and numerical simulation of permittivity and permeability of Teflon in X band. J Aerosp Technol Manag 2011;3:59–64.

[109] American Society of Testing Materials. ASTM D5568-1: Standard test method for measuring relative complex permittivity and relative magnetic permeability of solid materials at microwave frequencies. 2001.

[110] Baker-Jarvis J, Vanzura EJ, Kissick WA. Improved technique for determining complex permittivity with the transmission/reflection method. IEEE Trans Microw Theory Tech 1990;38:1096–103.

[111] Edwards Jt, Air Force Astronautics Lab Edwards AFB CA. Solid propellant flame spectroscopy. Air Force Astronautics Lab Edwards AFB CA; 1988.

[112] Hammack S, Rao X, Lee T, Carter C. Direct-coupled plasma-assisted combustion using a microwave waveguide torch. IEEE Trans Plasma Sci IEEE Nucl Plasma Sci Soc 2011;39:3300–6.

[113] Sutton WH. Microwave Processing of Ceramics - An Overview. MRS Online Proceedings Library Archive 1992;269. https://doi.org/10.1557/PROC-269-3.

[114] Kitchen HJ, Vallance SR, Kennedy JL, Tapia-Ruiz N, Carassiti L, Harrison A, et al. Modern microwave methods in solid-state inorganic materials chemistry: from fundamentals to manufacturing. Chem Rev 2014;114:1170–206.

[115] Wang X, Hossain K, Jackson TL. The three-dimensional numerical simulation of aluminized composite solid propellant combustion. Combust Theory Model 2007;12:45–71.

[116] Metaxas AC, Meredith RJ. Industrial Microwave Heating. IET; 1983.

[117] Jos J, Mathew S. Ammonium Nitrate as an Eco–Friendly Oxidizer for Composite Solid Propellants: Promises and Challenges. Crit Rev Solid State Mater Sci 2017;42:470–98.

[118] Kramida A, Ralchenko Y, Reader J, Others. NIST atomic spectra database (ver. 5.3) 2015.

[119] Singh H, Somayajulu MR, Bhaskara Rao R. A study on combustion behavior of magnesium-sodium nitrate binary mixtures. Combust Flame 1989;76:57–61.

[120] Walkiewicz JW, Kazonich G, McGill SL. Microwave heating characteristics of selected minerals

and compounds. Miner Metall Process 1988;5:39–42.
[121] Bykov YV, Rybakov KI, Semenov VE. High-temperature microwave processing of materials. J Phys D Appl Phys 2001;34:R55.
[122] Fay H. The Electrical Conductivity of Liquid Al2O3 (Molten Corundum and Ruby). J Phys Chem 1966;70:890–3.
[123] Amorim J, Baravian G, Jolly J. Laser-induced resonance fluorescence as a diagnostic technique in non-thermal equilibrium plasmas. J Phys D Appl Phys 2000;33:R51.
[124] Amorim J, Baravian G, Touzeau M, Jolly J. Two‐photon laser induced fluorescence and amplified spontaneous emission atom concentration measurements in O2 and H2 discharges. J Appl Phys 1994;76:1487–93.
[125] Zhao Y, Li X, Ma L. Multidimensional Monte Carlo model for two-photon laser-induced fluorescence and amplified spontaneous emission. Comput Phys Commun 2012;183:1588–95.
[126] Fourkas JT, Brewer TR, Kim H, Fayer MD. Picosecond polarization‐selective transient grating experiments in sodium‐seeded flames. J Chem Phys 1991;95:5775–84.
[127] Partridge WP Jr, Laurendeau NM. Formulation of a dimensionless overlap fraction to account for spectrally distributed interactions in fluorescence studies. Appl Opt 1995;34:2645–7.
[128] Zhang Z, Shneider MN. Measurement of plasma decay processes in mixture of sodium and argon by coherent microwave scattering. Phys Plasmas 2010;17:033108.
[129] Khambatta NM, Radziemski LJ, Dixit SN. Upper bound for a three-photon excitation cross section in atomic argon in the ultraviolet regime. Phys Rev A Gen Phys 1989;39:3842–5.
[130] Lambropoulos P. Theory of multiphoton ionization: Near-resonance effects in two-photon ionization. Phys Rev A 1974;9:1992–2013.
[131] Cowan RD. The Theory of Atomic Structure and Spectra. University of California Press; 1981.
[132] Wiese WL, Smith MW, Glennon BM, National Standard Reference Data System. Atomic Transition Probabilities. Volume I. Hydrogen Through Neon. National Standard Reference Data System; 1966.
[133] Shampine LF. Solving hyperbolic PDEs in MATLAB. J Comput Math 2005;2:346–58.
[134] Jiang Y, Deng S, Hong S, Zhao J, Huang S, Wu C-C, et al. Energetic Performance of Optically Activated Aluminum/Graphene Oxide Composites. ACS Nano 2018;12:11366–75.
[135] Alam SN, Sharma N, Kumar L. Synthesis of graphene oxide (GO) by modified hummers method and its thermal reduction to obtain reduced graphene oxide (rGO). Graphene 2017;6:1–18.
[136] Shokrollahi H. A review of the magnetic properties, synthesis methods and applications of maghemite. J Magn Magn Mater 2017;426:74–81.
[137] Wang Y, Song XL, Jiang W, Deng GD, Guo XD, Liu HY, et al. Mechanism for thermite reactions of aluminum/iron-oxide nanocomposites based on residue analysis. Trans Nonferrous Met Soc China 2014;24:263.
[138] Sui H, Atashin S, Wen JZ. Thermo-chemical and energetic properties of layered nano-thermite composites. Thermochim Acta 2016;642:17–24.
[139] Trunov MA, Schoenitz M, Zhu X, Dreizin EL. Effect of polymorphic phase transformations in Al2O3 film on oxidation kinetics of aluminum powders. Combust Flame 2005;140:310–8.
[140] Sundaram DS, Yang V, Zarko VE. Combustion of nano aluminum particles (Review). Combustion, Explosion, and Shock Waves 2015;51:173–96.
[141] Thakur P, Sharma V, Thakur N. Role of graphene as an additional fuel in Al/Fe2O3 nanothermite. AIP Conf Proc 2020;2265:030443.
[142] Jiang Y, Deng S, Hong S, Tiwari S, Chen H, Nomura K-I, et al. Synergistically chemical and thermal coupling between graphene oxide and graphene fluoride for enhancing aluminum combustion. ACS Appl Mater Interfaces 2020;12:7451–8.
[143] Shen J, Qiao Z, Wang J, Yang G, Chen J, Li Z, et al. Reaction mechanism of Al-CuO nanothermites with addition of multilayer graphene. Thermochim Acta 2018;666:60–5.
[144] Su Y, Kravets VG, Wong SL, Waters J, Geim AK, Nair RR. Impermeable barrier films and protective coatings based on reduced graphene oxide. Nat Commun 2014;5:4843.

[145] Smith AT, LaChance AM, Zeng S, Liu B, Sun L. Synthesis, properties, and applications of graphene oxide/reduced graphene oxide and their nanocomposites. Nano Materials Science 2019;1:31–47.

[146] Barkley SJ, Lynch JE, Miklaszewski EJ, Dilger JM, Crespo WF, Michael JB, et al. Microwave-assisted modulation of light emission intensity in alkali-pyrotechnic plumes. Combust Flame 2021;225:406–16.

[147] Cheng J, Roy R, Agrawal D. Radically different effects on materials by separated microwave electric and magnetic fields. Mater Res Innovations 2002;5:170–7.

[148] Crane CA, Pantoya ML, Weeks BL, Saed M. The effects of particle size on microwave heating of metal and metal oxide powders. Powder Technol 2014;256:113–7.

[149] Barkley SJ, Zhu K, Ballestero M, Michael J, Sippel TR. Measurements of Dielectric Properties of Condensed Phase Aluminized Composite Propellants. 52nd AIAA/SAE/ASEE Joint Propulsion Conference, American Institute of Aeronautics and Astronautics; 2016. https://doi.org/10.2514/6.2016-4593.

[150] Fiorillo F. Measurement and Characterization of Magnetic Materials. Elsevier Academic Press; 2004.